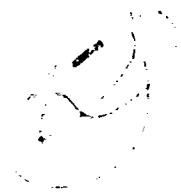


AD-A249 949

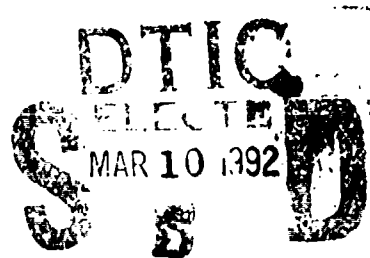
PL-TR-91-2278



Time Domain Regional Discriminants

L. J. Burdick, E. J. Garnero, C. K. Saikia and D. V. Helmberger

Woodward-Clyde Consultants
566 El Dorado Street,
Suite 100
Pasadena, CA 91101



1 November 1991

Scientific Report No. 1

APPROVED FOR PUBLIC RELEASE; DISTRIBUTION UNLIMITED



PHILLIPS LABORATORY
AIR FORCE SYSTEMS COMMAND
HANSCOM AIR FORCE BASE, MASSACHUSETTS 01731-5000

84 3 07 079

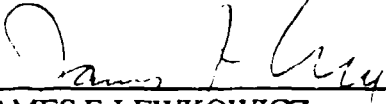
92-06120



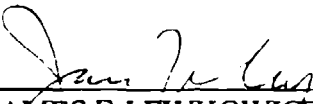
**Best
Available
Copy**

The views and conclusions contained in this document are those of the authors and should not be interpreted as representing the official policies, either expressed or implied, of the Air Force or the U.S. Government.

This technical report has been reviewed and is approved for publication.



JAMES F. LEWKOWICZ
Contract Manager
Solid Earth Geophysics Branch
Earth Sciences Division



JAMES F. LEWKOWICZ
Branch Chief
Solid Earth Geophysics Branch
Earth Sciences Division



DONALD H. ECKHARDT, Director
Earth Sciences Division

This document has been reviewed by the ESD Public Affairs Office (PA) and is releasable to the National Technical Information Service (NTIS).

Qualified requestors may obtain additional copies from the Defense Technical Information Center. All others should apply to the National Technical Information Service.

If your address has changed, or if you wish to be removed from the mailing list, or if the addressee is no longer employed by your organization, please notify PL/IMA, Hanscom AFB MA 01731-5000. This will assist us in maintaining a current mailing list.

Do not return copies of this report unless contractual obligations or notices on a specific document requires that it be returned.

REPORT DOCUMENTATION PAGE			Form Approved OMB No. 0704-0188	
Public reporting burden for this collection of information is estimated to average 1 hour per response, including the time for reviewing instructions, searching existing data sources, gathering and maintaining the data needed, and completing and reviewing the collection of information. Send comments regarding this burden estimate or any other aspect of this collection of information, including suggestions for reducing this burden, to Washington Headquarters Services, Directorate for Information Operations and Reports, 1215 Jefferson Davis Highway, Suite 1204, Arlington, VA 22202-4302, and to the Office of Management and Budget, Paperwork Reduction Project (0704-0188), Washington, DC 20503				
1. AGENCY USE ONLY (Leave blank)	2. REPORT DATE 11/1/91	3. REPORT TYPE AND DATES COVERED Scientific Report #1 11/1/90-11/1/91		
4. TITLE AND SUBTITLE Time Domain Regional Discriminants		5. FUNDING NUMBERS PE 62101F PR 7600 TA 09 WU AZ Contract F19628-90-C-0194		
6. AUTHOR(S) L.J. Burdick E.J. Garnero		C.K. Saikia D.V. Helmberger		
7. PERFORMING ORGANIZATION NAME(S) AND ADDRESS(ES) Woodward-Clyde Consultants 566 El Dorado Street Pasadena CA 91101		8. PERFORMING ORGANIZATION REPORT NUMBER		
9. SPONSORING / MONITORING AGENCY NAME(S) AND ADDRESS(ES) Phillips Laboratory Hanscom AFB, MA 01731-5000 Contract Manager: James Lewkowicz/GEH		10. SPONSORING / MONITORING AGENCY REPORT NUMBER PL-TR-91-2278		
11. SUPPLEMENTARY NOTES				
12a. DISTRIBUTION / AVAILABILITY STATEMENT Approved for public release; Distribution unlimited.		12b. DISTRIBUTION CODE		
13. ABSTRACT (Maximum 200 words) Most regional discriminants developed to date have been based purely on empirics, and many rely on the characteristics of spectra. At Woodward Clyde, a unique type of time domain discriminant has been developed based on a theoretical understanding of wave propagation and the direct identification of depth phases in P_n and P_g . This work has involved original basic research into the nature of the short period P_n waveform and the effect of pP_n on it; development of an understanding of the nature of P_n propagation; and inquiries into the relation of pP_n and $spall$. The studies of P_g have involved identification of a frequency band in which the waveform is stable; a forward modeling study of NTS regional data; and a careful breakdown of the wavenumber integration synthetics into the generalized rays that compose them. This work has led to direct identification of depth phase effects in P_g and a preliminary indication of how to detect and discriminate with them. This is the first report on a multi-year effort to complete development of the P discriminants, to extend the technology to S_n and S_g and to test the power of the discriminants on the new data bases from the Soviet Union. Strong efforts to analyze the new data from the Soviet Union have been undertaken including studies of both the older hand digitized analog records and of the digital data from the new IRIS stations.				
14. SUBJECT TERMS Regional Discriminants, P_n , P_g , S_n , S_g , Upper Mantle, Soviet Union.		15. NUMBER OF PAGES 86		16. PRICE CODE
17. SECURITY CLASSIFICATION OF REPORT Unclassified	18. SECURITY CLASSIFICATION OF THIS PAGE Unclassified	19. SECURITY CLASSIFICATION OF ABSTRACT Unclassified	20. LIMITATION OF ABSTRACT SAR	

TABLE OF CONTENTS

Introduction	1
Recently Developed Waveform Discriminants	3
Upper Mantle Triplications Beneath Asia	26
Composition of Regional Pn and Sn Waveforms Recorded in the U.S. and U.S.S.R.	51
References	72



Accession For	
NTIS GRA&I	<input checked="" type="checkbox"/>
DTIC TAB	<input checked="" type="checkbox"/>
Unannounced	<input type="checkbox"/>
Justification	
By _____	
Distribution/ _____	
Availability Codes	
Dist	Avail and/or Special
A-1	10

INTRODUCTION

The time and frequency domains are equivalent displays of seismic trace information, though some qualities of the signal are more easily observed in one domain than the other. The relative frequency excitation of Lg, for instance, is most easily viewed in the frequency domain, but such waveform qualities as the sequence in which pulses arrive in the wave train or the sharpness of pulse onset are most easily studied in the time domain (Murphy and Bennett, 1982; Blandford, 1981). Because of the tremendous complexity of high frequency regional data, most attempts at using it for discrimination purposes have involved analysis of the frequency content of the various arrivals either through transforming selected windows or through multiple bandpass filtering. We report here on our initial attempts to explore the alternative and to discriminate events using those waveform characteristics most easily observed in the time domain.

A second advantage of time domain analysis approaches is that they permit a deeper insight into the physical processes creating a seismic signal's character. For this reason, they can be more easily used to evaluate the transportability of a discriminant to varying geophysical and tectonic regimes. This is an especially important feature in the development of regional discriminants. The most prominent and successful spectral regional discriminants have been empirically developed. This means that they must be redeveloped and reverified in each new area. As we shall show in the following, through rigorous time domain analysis such features as regional depth phases can be identified and used to discriminate. Discriminants based on such simple physical features as source depth should be transportable anywhere.

In work recently completed under the treaty verification program, we have proved that such time domain discriminants do exist. In analyzing a test discrimination data set from the western U. S., we have discovered that the onset of P_n is always very similar for explosions and that few earthquakes have this unique waveform character. This information can be constructed into a simple discrimination scheme by testing the correlation of observed P_n waveform onsets with average waveforms observed from explosions. High correlations indicate explosions and low correlations earthquakes. We have also discovered that the regional phase P_g is actually composed

of a sequence of sub-arrivals which correspond to successively higher orders of reverberation in the crust. In realistic crust models, the depth phases play an important role in the waveshapes of these sub-arrivals. By selecting an appropriate frequency band to analyze, we have been able to accurately model this type of data from explosions in the western United States. Over the very relevant regional distance ranges of 200 to 600 km, it appears that a discrimination procedure very similar to the one which is known to work for P_n will also be effective for P_g . We are investigating whether similar discriminants can be constructed based on the phases S_n and S_g in areas where those phases are prominent arrivals.

RECENTLY DEVELOPED WAVEFORM DISCRIMINANTS

Though the technology for recording broad band seismic data digitally has existed for some time, a good regional net of stations surrounding NTS has only been put into place recently (Figure 1). Several different types of stations and seismometers are in the net including DWWSSN (JAS, AIQ or ANMO), LLNL broad bands (ELK, MNV, LAC, KNB) and the new Streckeisens installed by Caltech (PAS) and UCSD (PFO). Much recent effort at Woodward Clyde has been directed at developing short period regional discriminants that work on data from this net. The situation of having data available from many sources very close to each other which are similar in character such as NTS explosions is a unique one. The timing and locations of the events are known exactly. This turns any single regional station in the western U. S. into the equivalent of a regional seismic array. Any of the standard array processing techniques can be used with the role of sources and stations being reversed. There is some variability in source time history and near source structure, but on the other hand the receiver structure is constant. We began our previous work by simply obtaining suites of records from each of the stations in the net and summing to form stable averages. In so doing, we observed important features in the average P_n and the average P_g waveforms which could each be used to develop time domain discriminants. Our success to date is summarized below.

The P_n Waveform Discriminant Our initial success in developing a P_n waveform discriminant was rooted in past experience with modeling waveforms of teleseismic P waves from nuclear explosions. Figure 2 is taken from Burdick et al. (1984). It shows observed and synthetic, long and short period records from the nuclear test, CANNIKIN. Arrows on the left of the figure draw attention to a subtle feature in the short period records which is associated with the arrival of the phase pP . The records where the feature appears are assumed to be along high Q paths ($t^* = 0.8$ s). Along lower Q paths the feature washes out. The long periods are not affected by pP in a clearly visible way.

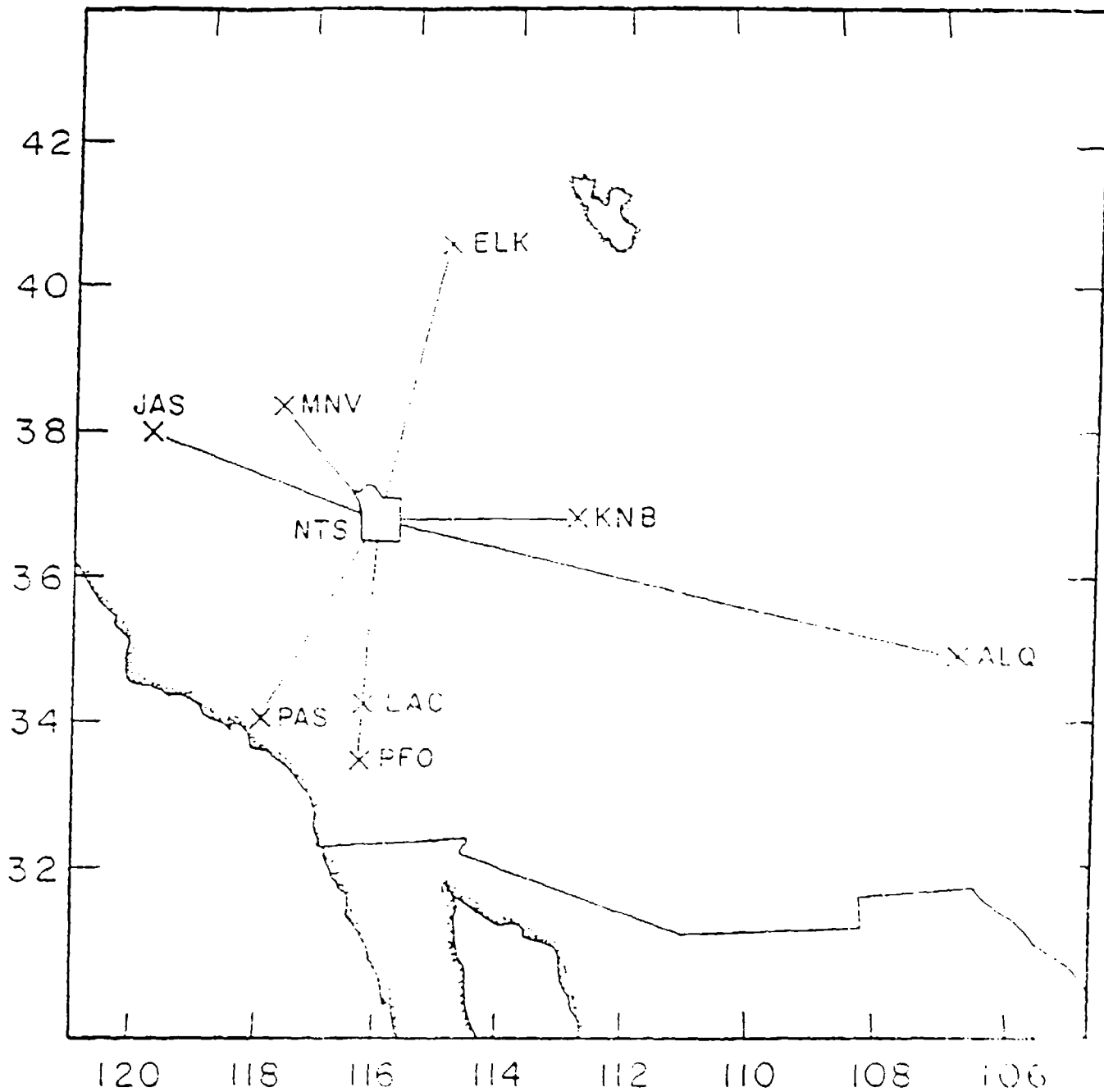


Figure 1. Map showing the distribution of stations from NTS. Of these ELK, KNB, LAC and MNV are broad band stations operated by LLNL, the station ALQ and JAS are operated by DIWSSN and the stations PAS and PFO by universities.

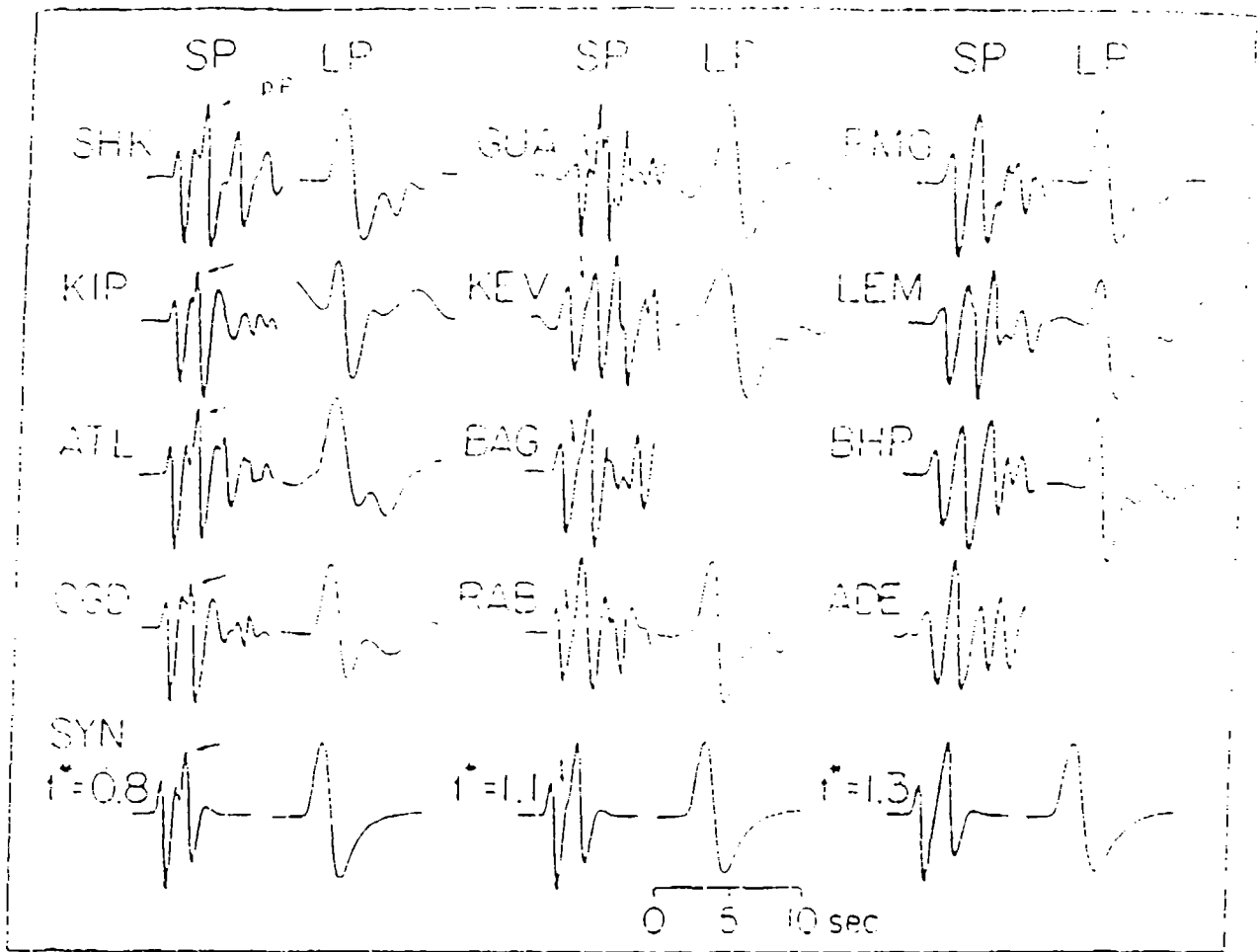


Figure 2. Comparison of observed short and long period P waves with synthetic seismograms for a range of t^* values at teleseismic distances. As t^* increases, the interference in the second upswing produced by pP becomes less apparent. pP can be observed as a distinctive double peak and is produced in the synthetics with an artificial delay.

This previous experience with the effects of pP on teleseismic short period P waves proved valuable in interpreting regional P_n waveforms. As it happens, some of the stations in the western U.S. digital net have a band-limited response equivalent to the WWSSN stations in Figure 2. To make a uniform comparison, all of the records in the data base were transformed to short period WWSSN instrument response. When the digital signals from NTS explosions were averaged, it was observed that the average P_n waveform was very similar to those on the left of Figure 2 although much shorter in period. Average waveforms at 5 stations in the digital net are shown in Figure 3. The consistent splitting of the second upswing is indicated by the arrows. The clear implication is that the physics of the wave propagation of short period teleseismic P and short period P_n is very comparable. More precisely, the interaction of pP with P must be similar in the two instances. This is not unreasonable in that the apparent velocity of P_n is about 8 km/s and that of teleseismic P only increases to about 12 km/s at 30°. The associated change in pP timing and amplitude is small. The implications for regional discrimination are clear. Only very shallow sources like explosions will have depth phases at very short times. Earthquake depth phases will be much later. To test the performance of this discriminant, we assembled a set of P_n waveforms from small earthquakes near NTS, windowed out the first three seconds of P_n and measured the correlation with the average P_n waveforms of explosions like those shown in Figure 3. A similar procedure was carried out on the explosion data base. The results from one typical station, JAS are shown in Figure 4. The explosions are displayed as stars and the earthquakes as crosses. The separation of the populations is good enough to warrant more study of this discriminant.

The discrimination capability illustrated in Figure 4 only demonstrates that the P_n waveform of explosions is stable at JAS and consistently different from earthquake waveforms. However, the similarity of the waveforms in Figure 3 suggests that the shape of the explosion waveform is consistent from station to station. That this is indeed the case is shown in Figure 5 where the average JAS explosion waveform has been correlated with the explosion data base at MNV.

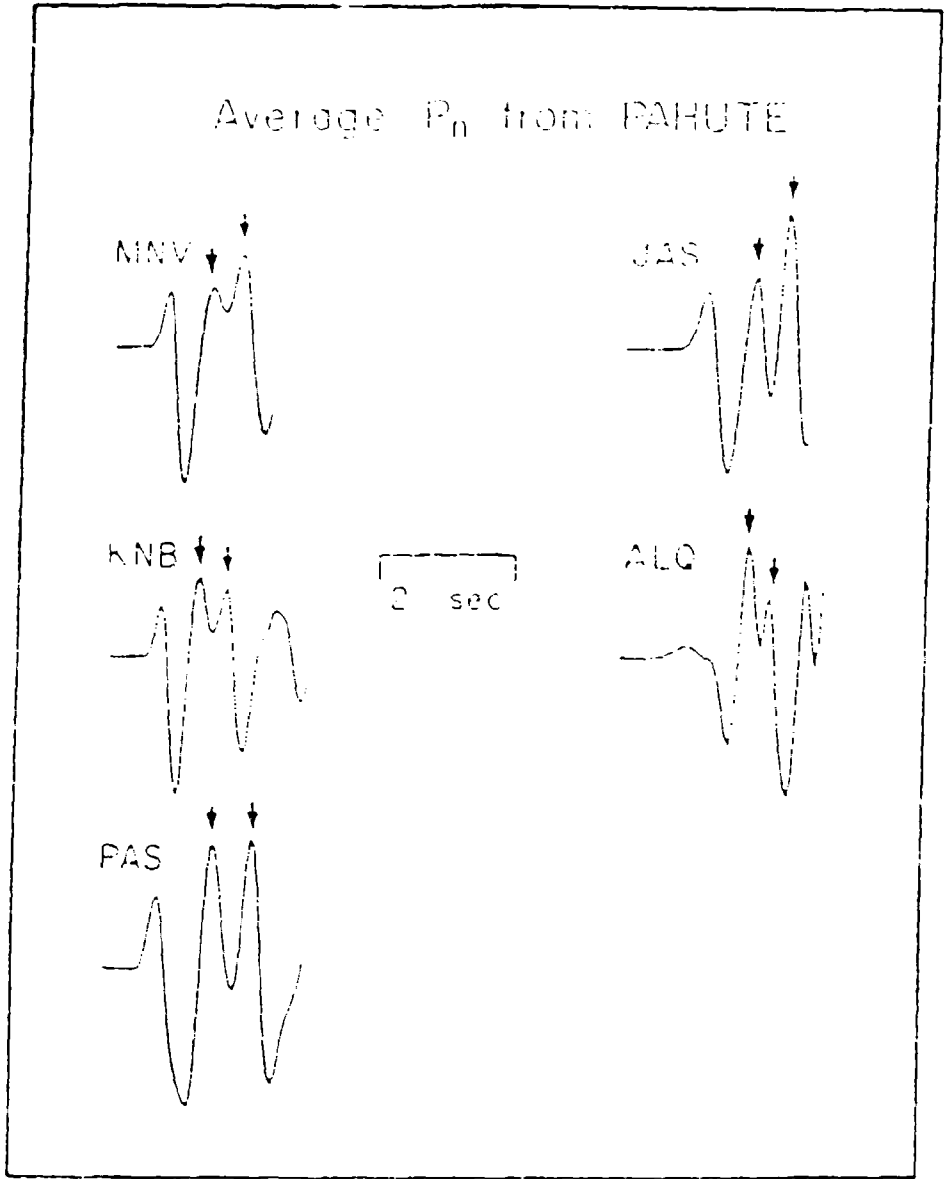


Figure 3. The average P_n waveform for Pahute explosions observed at stations in the western U.S. digital net. The split third swing is indicated by arrows.

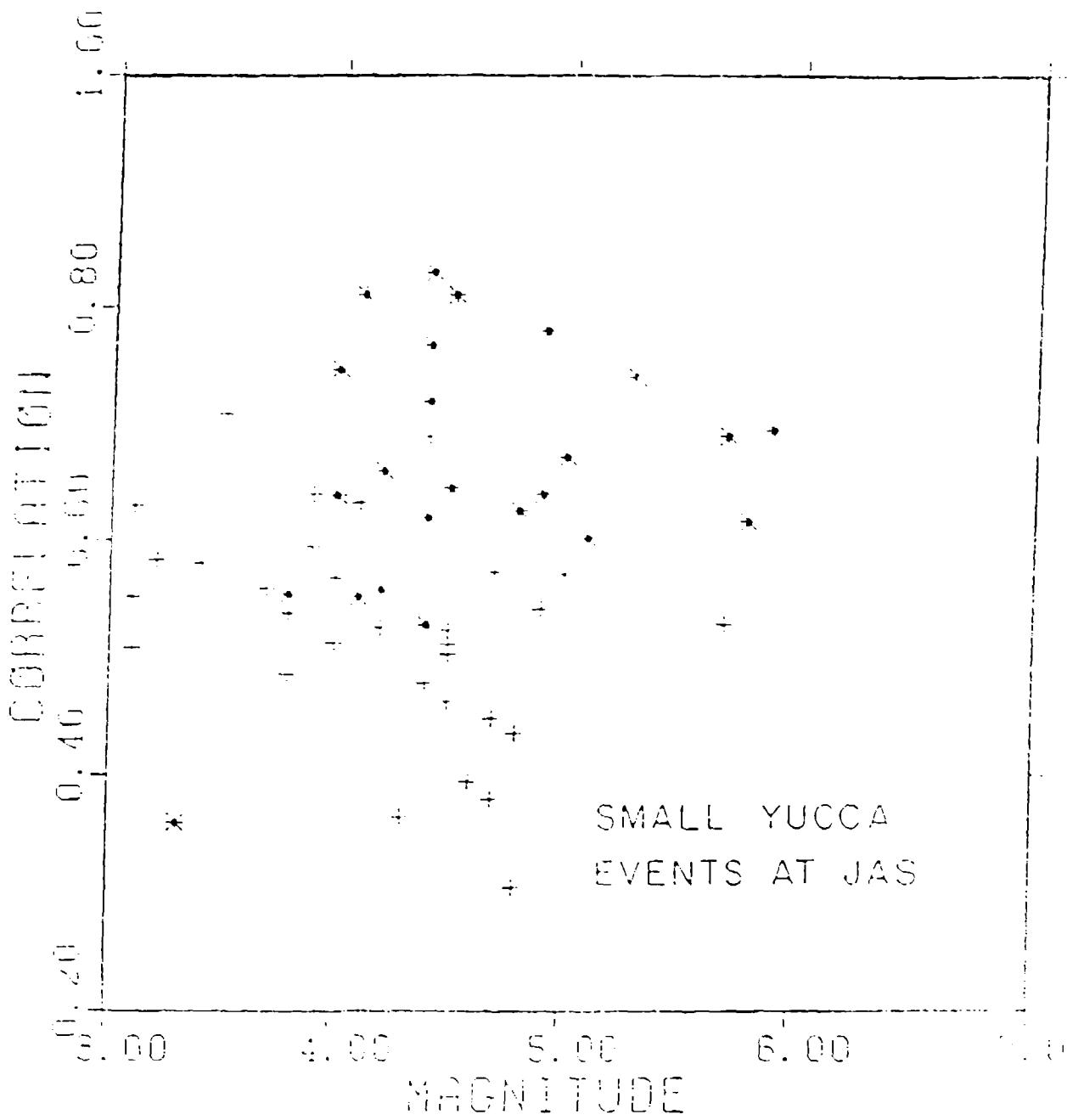


Figure 4. Discrimination of Yucca explosions from earthquakes using correlation with the average P_0 waveform at JAS. The explosions are stars and the earthquakes are crosses.

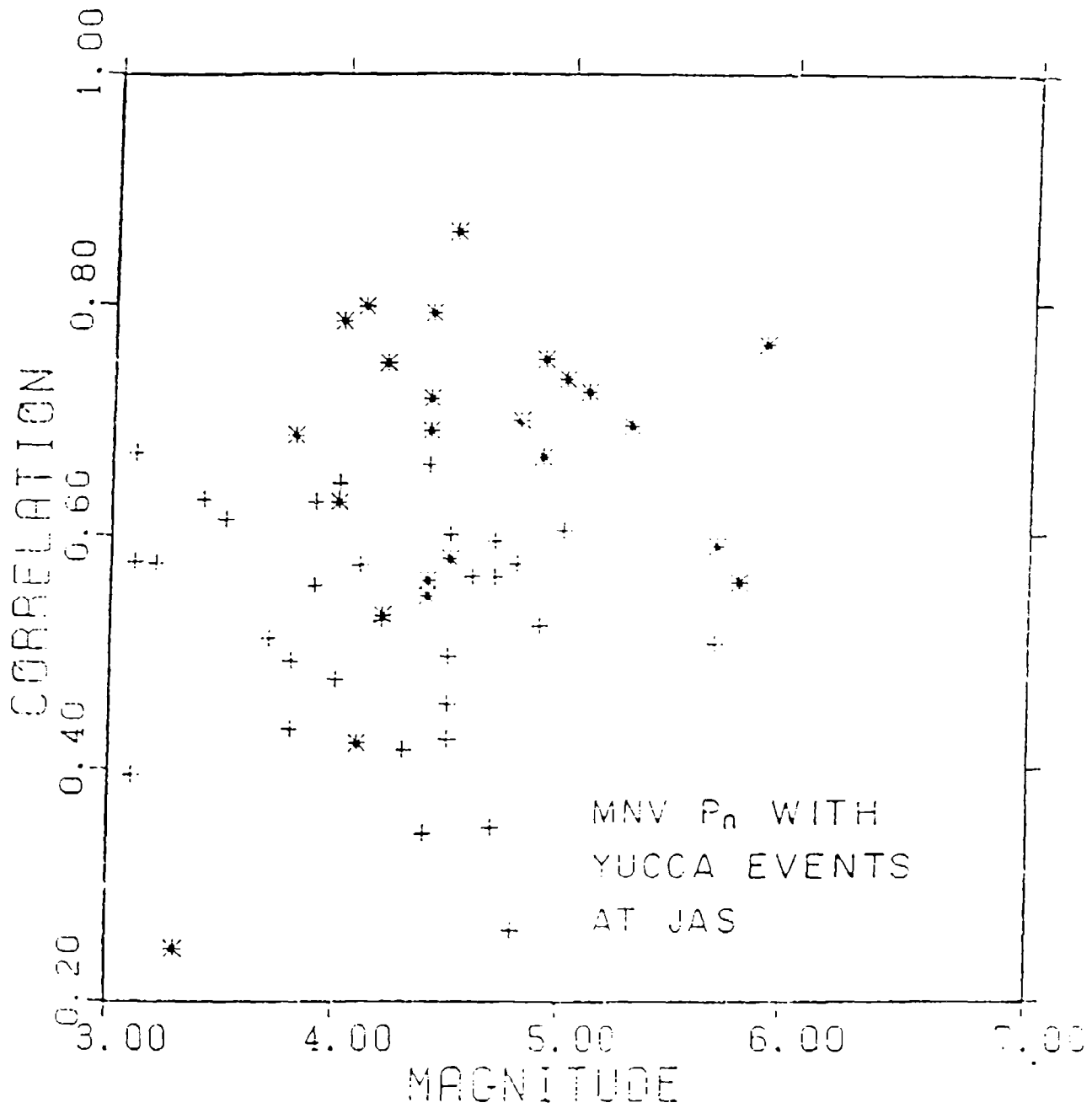


Figure 5. Discrimination of Yucca explosions from earthquakes using the average P_n waveform from MNV and the data base from JAS. Explosions are stars and earthquake are crosses. The separation of the populations is comparable to that in Figure 4 illustrating the transportability of the discriminant.

Moderately good event discrimination is still possible. These studies suggest that one method to achieve discrimination with a regional net will be to continuously monitor the waveform of P_n onset at all of the stations and to test in an objective fashion for the presence of depth phases.

The small shoulder on the second upswing of the waveforms in Figure 3 seems to be a relatively subtle feature on which to base a discriminant. However, its apparently subtle nature is due to the particular response of the WSSN instrument. To demonstrate this, we carried out a forward modeling study of the broad band P_n waveforms from the LLNL stations designed to determine the true size of the pP arrival. A typical result is shown in Figure 6 where the waveforms of four Pahute events as recorded at MNV are displayed. The data are shown as solid lines and synthetics for an appropriate crustal model and explosion source are shown as dashed lines. Because the instruments are broad band, deconvolving the response out is a stable operation which has been carried out. The traces shown are true ground velocity. The arrows indicate the arrival of pP_n in the data and synthetics. The observed pP_n is consistently much later than the elastic predictions. This discrepancy was observed for all events at all stations where the waveforms could be modeled. In many instances, it was observed that pP was as much as two times larger than the elastic predictions. Similar results (pP late and amplified) have been reported in most studies where pP times from nuclear tests have been measured. In our final report for our previous work (Burdick et al., 1988), we showed that this phenomenon could be explained in terms of spall. These studies are relevant here in two ways. First, effective pP (that is pP plus spall) is a large arrival, and it is sensible to attempt to continuously examine signal onsets for its presence in order to discriminate. Second, synthetic modeling of the P_n - pP_n interaction is very feasible, and it is reasonable to attempt its use in automated discrimination schemes.

The P_g Discriminant The second new short period regional discriminant we are developing and testing in the western U.S. is based on the observation that the P_g phase turns out to contain a sequence of sub-arrivals. They correspond to successive reverberations of energy in the crustal wave guide, and we have named them crustal resonance phases. Our initial evidence as to their existence and character emerged when we averaged observations of suites of events at a single

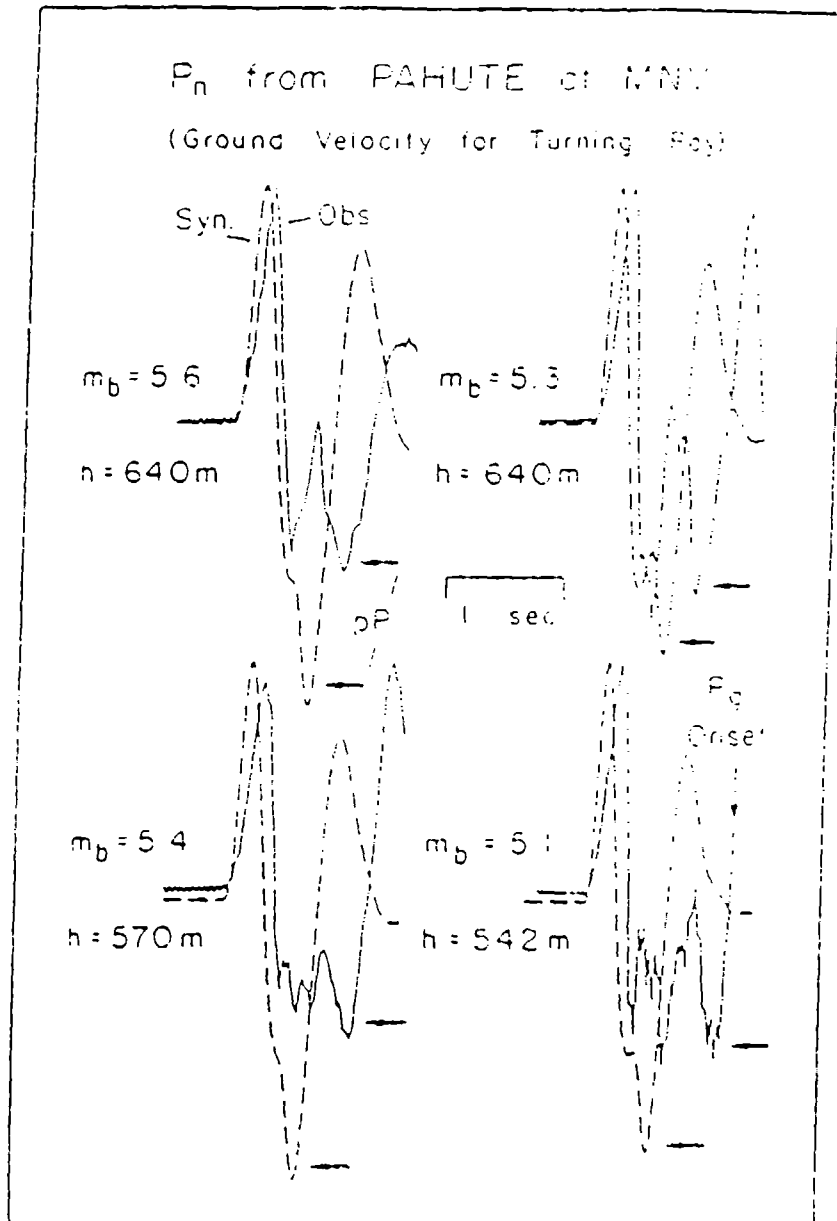


Figure 6. Observed versus synthetic P_n waveforms at MNV for Pahute events. The turning ray model for propagation is assumed. The Mueller-Murphy source scaling relations and a t^* value of 0.1 s are also assumed. As indicated by arrows, the observed pP arrival is late but approximately the same in size as the elastic prediction.

station just as did the evidence for pP_n . Though there were some indications of a series of arrivals pumping energy into the P_g coda in some of the raw data, the effects of scattering and other variations between events seems to dominate. This has long been known to be the greatest difficulty in interpreting regional data. To suppress the scattering effects, we aligned the signals very carefully at P_n time and summed. The Yucca and Pahute data were treated separately. This procedure neglects the difference in slowness, but our results indicate that this is a reasonable approach. Some of the clearest evidence for the phases came from ALQ. The result for Yucca events is shown in Figure 7 where we display a progressive sum of records. Each subsequent line shows the effect of adding in an additional record. The final sum clearly indicates that there are coherent resonance phases at frequencies of several Hz. The first two crustal resonance phases develop almost immediately indicating that they are very coherent. A third appears by the time 4 traces are added in and the sum has stabilized by the time 8 are added in. Actually, this is a relatively rapid rate of stabilization indicating that the resonance phases are very coherent for this path. At the bottom, we show a synthetic for a simple layer over a half space model to indicate that the resonance phases have approximately the character we expect.

Since it is clear that these reverberation phases exist, it is natural to explore the possibility that they could be useful in discrimination. There have been many studies of the relative properties of the long-duration, composite phases such as P_g or S_g . Now that we know that the complete phases are built up of sub pulses, we can attempt to base discriminants on their properties. A large number of possibilities exist. Any discriminant which has been tried on the composite pulses can be tested on the sub pulses. These could include particle motion, relative amplitude, frequency content or sharpness. To illustrate that important variations in the character of the resonance phases exist, we show the three component record of the Pahute event TIERRA at ANMO in Figure 8. The instrument response is short period DWSSN. The resonance phases are clear on the vertical, but vary markedly in their character on the horizontals. The second resonance phase appears to be carrying much more S energy. As we will show in the following, the first crustal resonance appears to be an efficient energy channel for P and later resonances for S. One possible

PROGRESSIVE SUM OF RECORDS
YUCCA TO ALQ OF ANMO

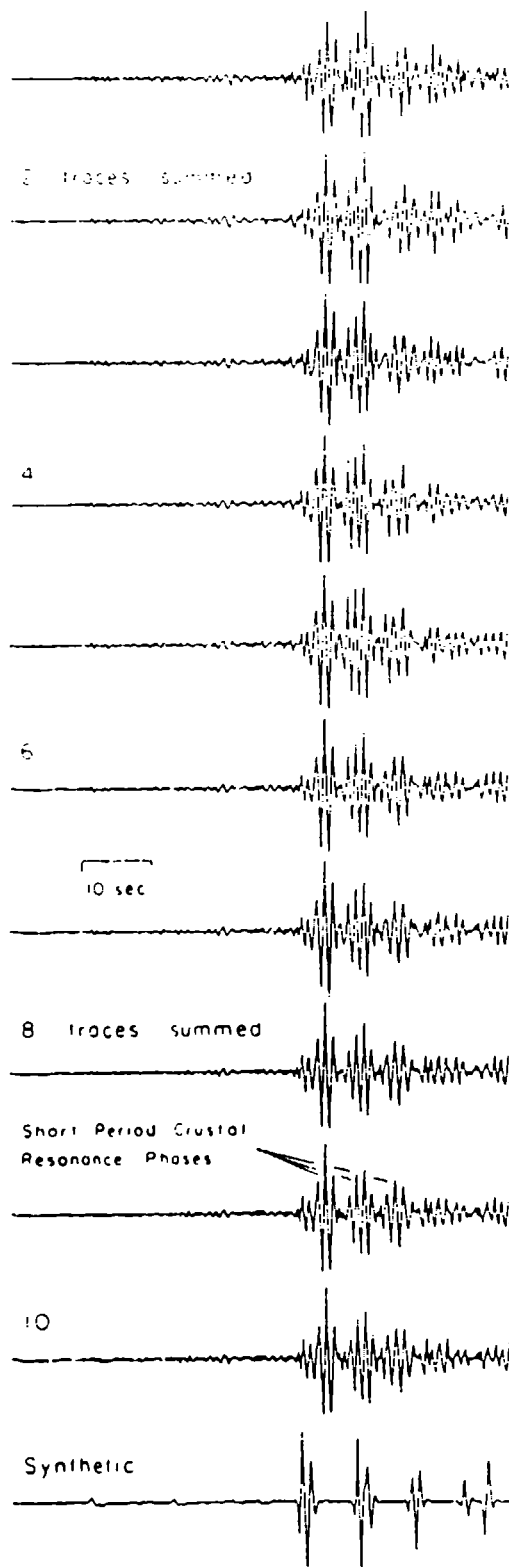


Figure 7. The crustal resonance phases for Yucca events are separated from the noise by stacking. The synthetic at the bottom merely indicates that the phases have approximately the right timing and amplitude.

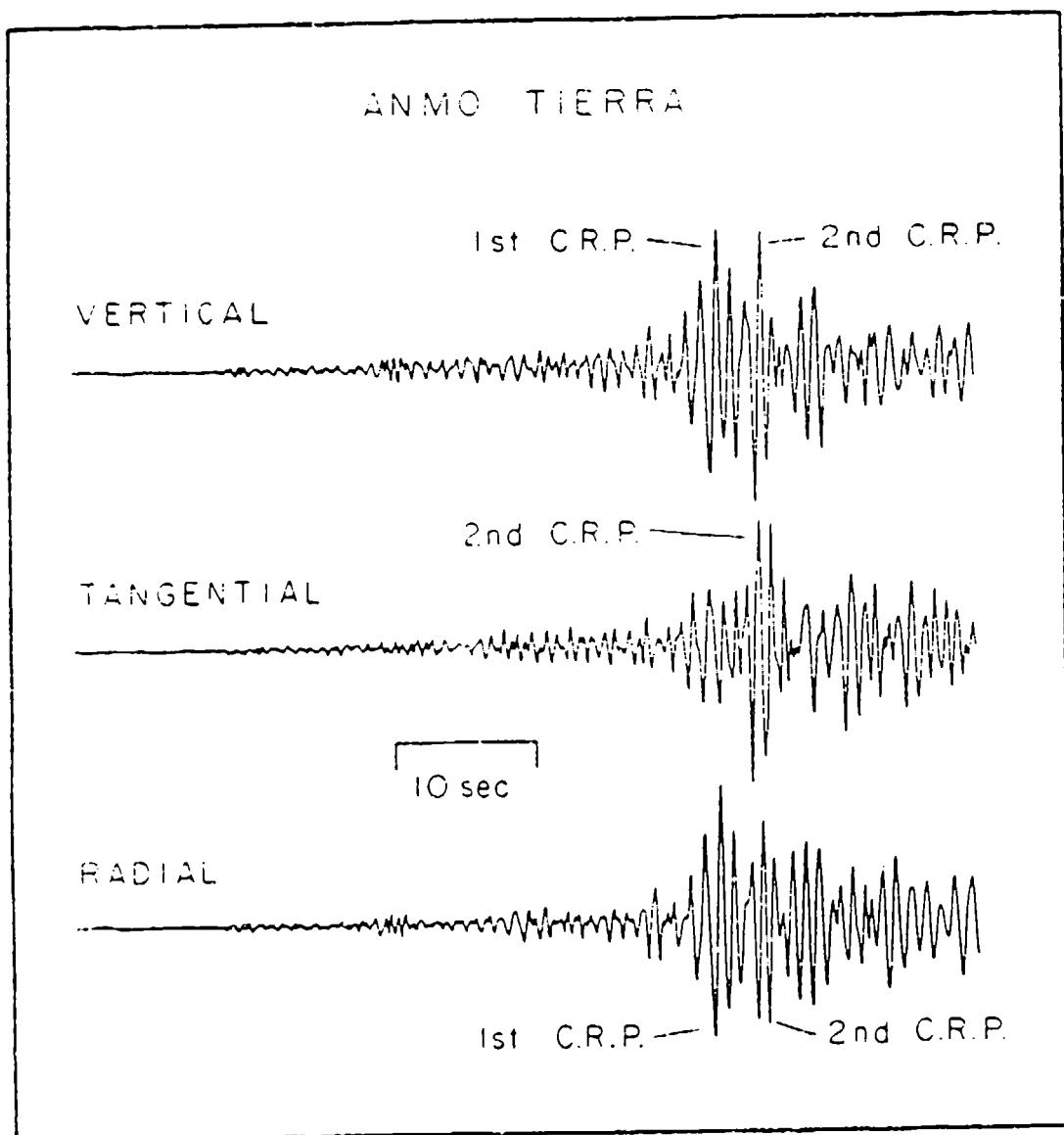


Figure 3. Three component observation at ANMO of a small Pahute event. Note the increase in the amount of S energy at the time of arrival of the second crustal resonance phase. This is presumed to be scattered SV.

method for discriminating using P_g may be to measure the relative amount of scattered SV energy between the first and third resonance phases. There should be more scattered S in earthquakes. In the following, we shall discuss the development of a time domain discriminant based on time domain correlations of longer period (2 sec. and greater) energy, but the point here is that there are a number of alternate discriminants possible.

We began our work in the western US by attempting to identify a frequency band in which the stable resonance phases (resolved in Figure 7 by stacking) could be observed consistently in individual records. This would naturally occur in a somewhat longer period band. We obtained suites of explosion records from each of the stations in the digital net and experimented with a number of bandpass filters. We achieved the desired stability using the WWSSN long period response modified by a high pass and a low pass third order butterworth filter. The long period butterworth cutoff was positioned at 10 sec and the low pass at .6 sec. This resulted in signals with a dominant period of about 2 sec. A suite of records from about 15 events was released to us by LLNL and some of the records with the best signal to noise are displayed in Figure 9. The strong correlation of the waveforms is apparent as is the move out of P_n in front of P_g with range. There are differences between the Yucca Flat and Pahute Mesa signals at the same station, but this is not surprising given the variation in distance to the test sites.

We developed and tested appropriate generalized ray and wavenumber integration codes for computing synthetics of P_g which in this period range is sometimes called P_n . We examined a number of plausible crustal models attempting to keep them as simple and realistic as possible. Our preferred structure model for the western U.S. was a crustal layer 32 km thick over a standard lid model with a realistic free surface velocity decrease grading smoothly over the top 6 km. Green's functions for the model computed using wavenumber integration and generalized ray theory are compared on the left and right of Figure 10 respectively for a suite of ranges. The wavenumber results are exact except for the limits of numerical integration while the generalized ray results

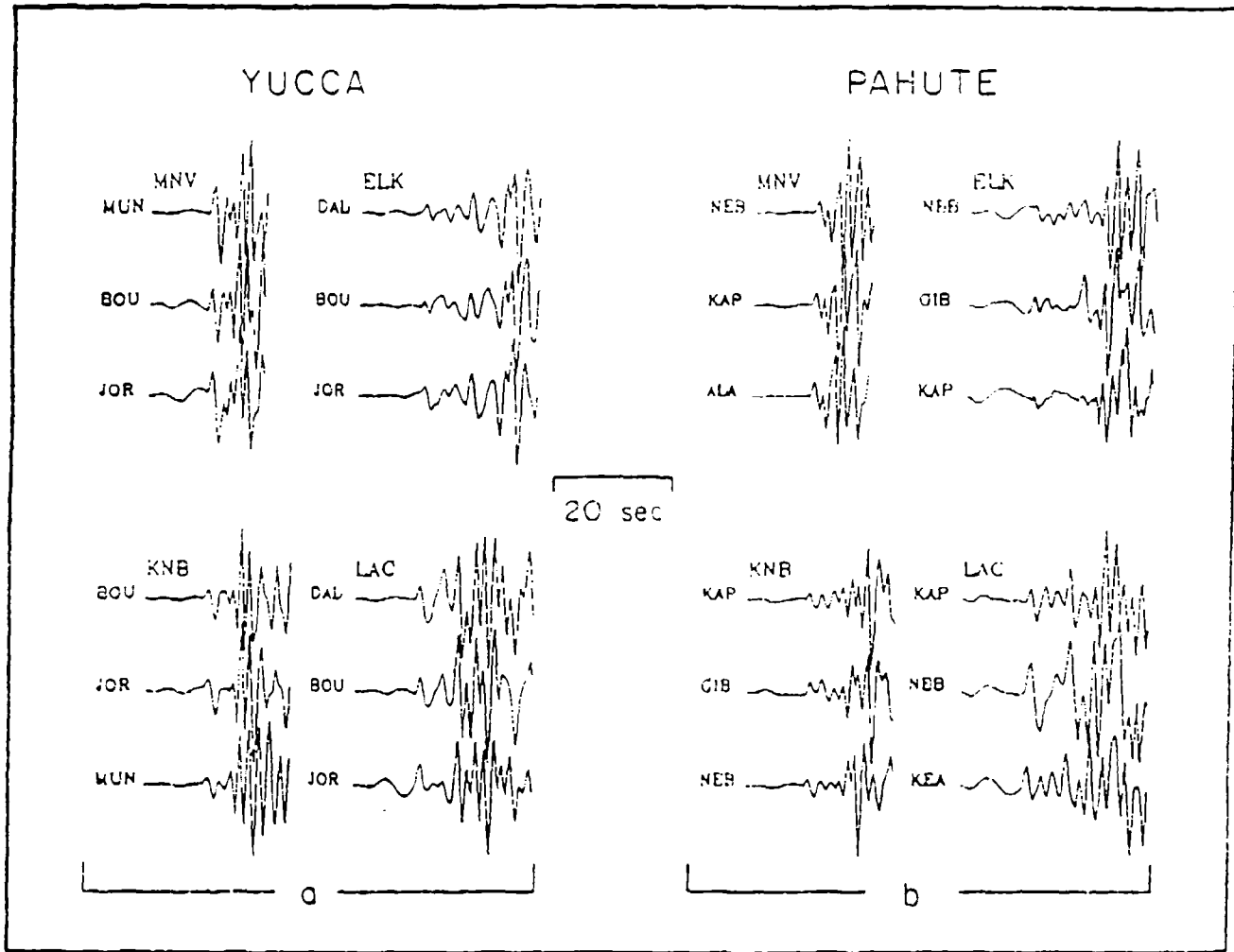


Figure 9. Recorded P_{n1} seismograms from both Yucca flat and Pahute Mesa on the LLNL network after convolving with a WWSSN LP instrument and a recursive bandpass filter (low-cut = 0.1 Hz, high cut = 0.6 Hz and third-order Butterworth causal). (a) For Yucca flat explosions and (b) for Pahute Mesa explosions. Data show remarkable stability. Original instrument response was deconvolved.

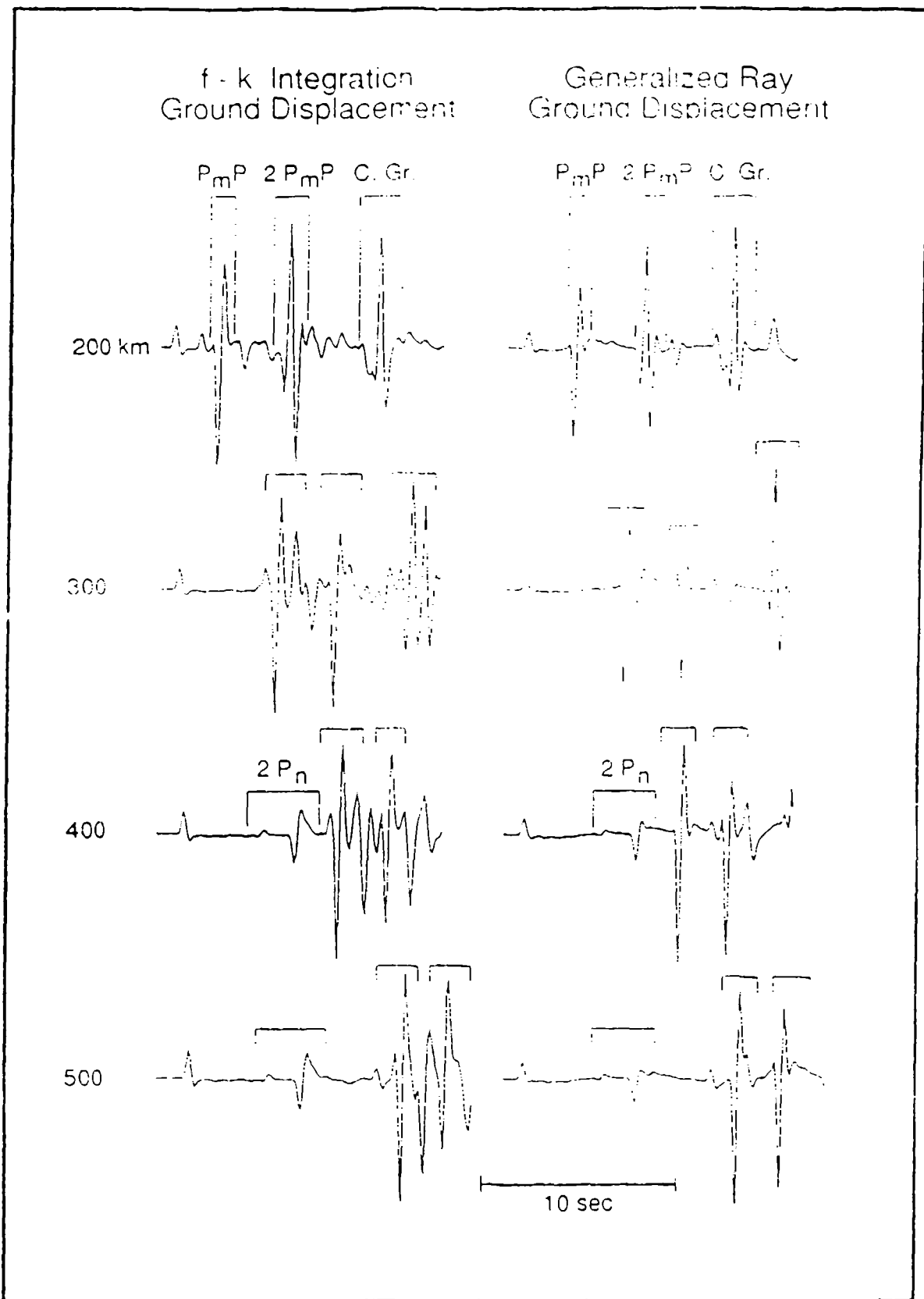


Figure 10. A comparison of Green's functions computed using wavenumber integration vs. generalized rays. Traces shown are displacement with a Mueller-Murphy source. Four dominant ray groups are identified.

are somewhat affected by truncation of the ray sum. The generalized rays include only those which reflect from the free surface or the Moho thus neglecting internal reflections within the surface gradient.

The utility of having reasonably accurate generalized ray synthetics is that they can be decomposed into ray subsets to determine the paths carrying the dominant energy. Four subgroups of rays are identified in the figure, and they are clearly related to the resonance phases discussed above. The first energy is of course P_n , but the first large arrival or P_g onset is composed of PmP and $pPmP$. The contribution of the free surface reflection is significant. The second group of rays forming the second resonance is dominated by $2PmP$ and $2pPmP$. The third group labeled C. Gr refers to some unusual rays in a Converted Group. They are dominated by $PmSPmP$, $PmPSmP$ and their free surface reflections. Note that this converted group moves rapidly out of the synthetic window and that it evolves a great deal of complexity in the wavenumber integration synthetics. These mean that it will not strongly affect a discriminant focused on the onset of P_g and that it is undesirably sensitive to the details of the free surface gradient. However, it may constitute the desirable channel for scattered S energy discussed earlier. At any rate, the fourth group noted in Figure 10 is a second head wave dominated by $2P_n$. This arrival is part of the same generalized ray as $2PmP$, so it is not surprising that if the reflection is strong so is the head wave. The free surface reflection plays an important role in shaping $2P_n$ just as it does for $2PmP$. We computed similar synthetics for a crust model without the free surface gradient and found that the effect of the gradient is to dramatically increase the significance of $2PmP$ and all of the free surface reflections. Without the gradient, much more upgoing energy converts to SV as should be expected.

The next two figures present those records which we believe make a particularly strong case for interpretation of the P_g observations in terms of the four basic generalized ray groups discussed in the previous section (PmP , $2PmP$, Converted Group and $2P_n$). Figure 11 shows four records at distances of about 200 or 300 km. Note in Figure 10 that this is where the generalized ray interpretation is most valid. For each station, we show the observation on top, a complete

RAY INTERPRETATION

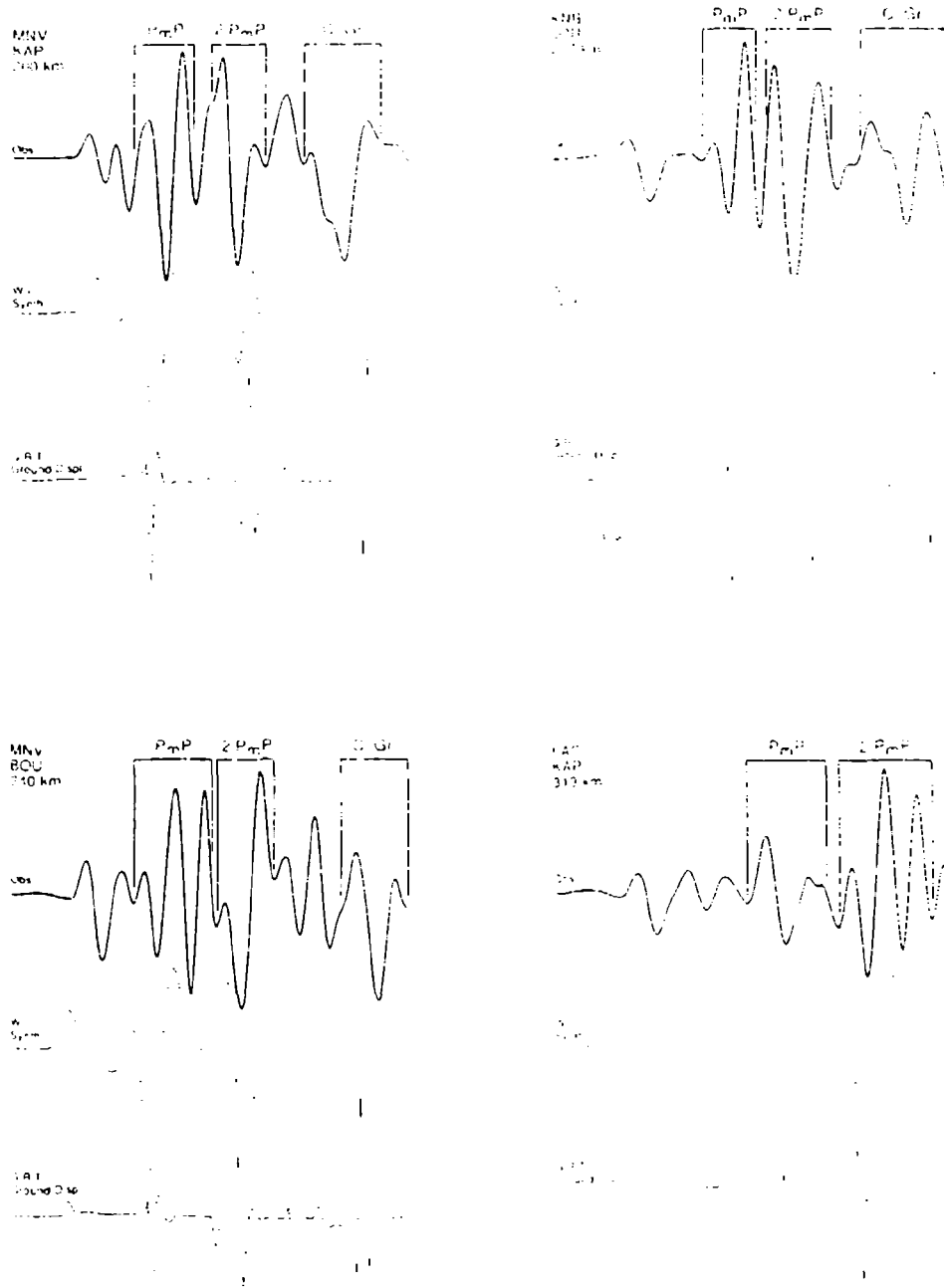


Figure 11. Interpretation of regional P_{ni} from explosions in terms of major ray groups.

wavenumber integration synthetic and finally a generalized ray Green's function beneath to aid in interpretation. The two records from MNV comprise a strong case that most of the P_g arrival is comprised of an interference of the PmP and $2PmP$ group. The relative amplitudes and exact details differ between observation and prediction, but these are two second waves and this level of fit is typical of that generally obtained in this period range. There is definite support for the converted ray group, but its role in determining the waveshape is not as strong as for the other two groups. The records at KNB and LAC provide further support that P_g in this distance range is predominantly an interference of two main pulses. The synthetics again do not predict the exact ratio of $PmP/2PmP$ amplitudes, but they are reasonably close.

Figure 12 presents a similar interpretation of four records at close to 400 km range. There is continuing evidence of the importance of PmP and $2PmP$ in determining the P_g wave shape. The converted group is outside the synthetic window. The primary difference is that the $2P_n$ group has emerged in front of PmP and caused a clear pulse. It is important to note the inclusion of the PmS , $pPmS$ and $pSmP$ head waves within the $2P_n$ group. The reason is that the $2P_n$ wave itself is a negative pulse as shown in the generalized ray Green's function. In all cases except for the ELK record the first motion of the $2P_n$ group is clearly positive. The wavenumber synthetics predict a weak positive arrival. We interpret the strong positive arrivals in the data as being associated with the PmS group, though the observed arrivals are definitely sharper and higher amplitude than predicted. Our model generally fails to predict head wave behavior in this regard. The fit of the observations to the synthetics after the onset of $2P_n$ is, on the other hand, most acceptable and substantiates our model for the fine structure of Pnl .

The adequacy of the very simple crustal structure, Model 3, for modeling the completely trapped (past critical angle) response though not the head waves in our data base is simple to explain. The model has no structure; no velocity increase at all beneath the crust-mantle transition. The completely trapped energy has no penetration beneath the Moho so it is insensitive to this detail. The head waves do penetrate, and in particular, would be sensitive to a positive gradient below the transition. The Moho is a world-wide feature, so that in any region the development

RAY INTERPRETATION

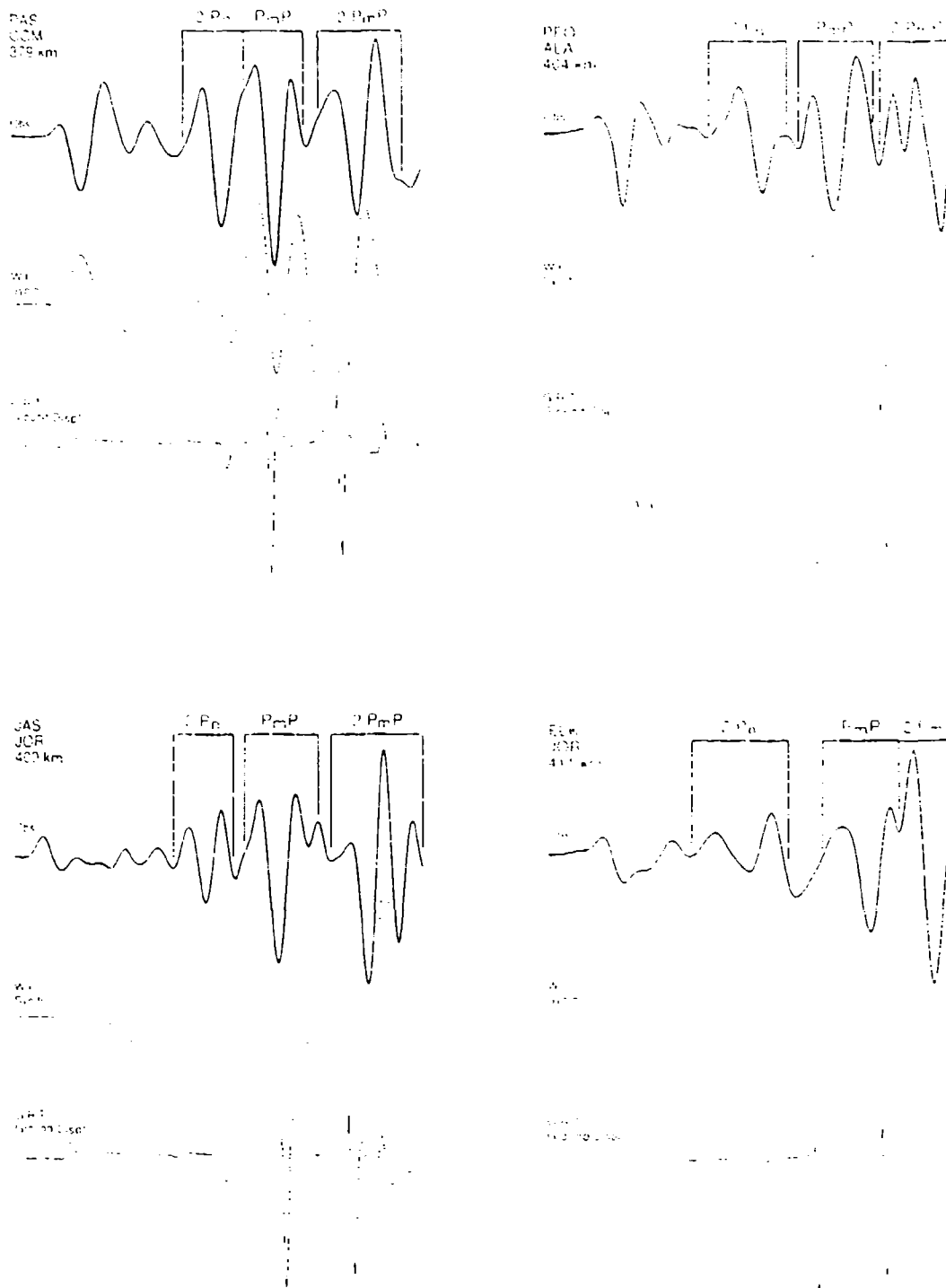


Figure 12. Interpretation of regional P_n in terms of the major ray groups.

of the P_g through the PmP - $2PmP$ interference could be anticipated, and because the energy is completely trapped, the waveform would be insensitive to lateral variations in lid structure. This has important implications in solving the event discrimination problem.

Two of the most general physical bases with which to develop a discriminant between explosions and earthquakes are the event depth and the level of shear radiation. We have found that the beginning of the P_g arrival is relatively deterministic and, because of the free surface gradient, relatively sensitive to the free surface phases. Because of the increased number of significant ray paths, the number of free surface contributions increases along with the complexity of the free surface contribution. Clearly the free surface interaction is very dependent on source depth, but it is also sensitive to the level of shear radiation and associated S to P conversion. A clear path to follow in attempting to develop a discriminant would be to focus analysis on the P_g onset in the period range we have been studying here. To establish the level of differences to be expected between explosions and earthquakes, we computed Green's functions for a point double couple buried at 7 km depth in our Model 3. The predicted waveforms for a range of 300 km are compared to the synthetic for a shallow explosion in Figure 13. The source for the earthquake was assumed to be a triangle with 1.4 sec rise and fall time. This is appropriate for a magnitude 5.6 earthquake which is consistent with the event size used in computing the explosion source. The explosion synthetic is shown on the top followed by synthetics for a vertical strike slip, a vertical dip slip and a 45° dip slip fault. The differences in both the P_g and P_n waveforms are apparent.

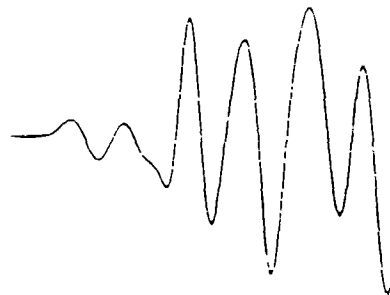
There are a variety of approaches possible in the development of a discriminant from the type of waveform information shown in the figure. In the case of P_n we used a simple correlation norm as discussed in the previous section. We developed a discriminant by simply determining the average waveform expected for an explosion and correlating that waveform with P_n waveforms from a mixed data base. The explosion-explosion norms were on average about 30% higher than the explosion-earthquake. The correlation norms for the earthquake waveforms with the explosion waveform are shown next to the traces in Figure 13. The correlation of the explosion with itself

REGIONAL SEISMOGRAMS

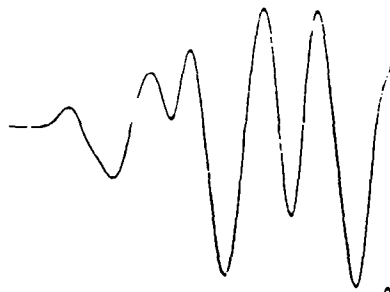
Explosion 0.64 km
Earthquake 7.00 km



EXPLOSION
ccor = 1.000

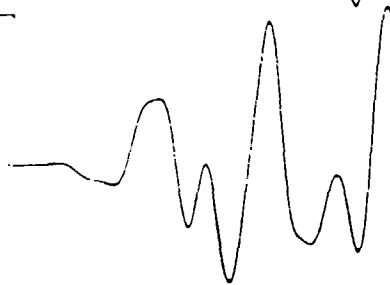


VERTICAL STRIKE SLIP
ccor = .532



VERTICAL DIP SLIP
ccor = .604

10 sec



45° DIP SLIP
ccor = .446

Figure 13. Synthetic regional seismograms for Model 3 at a range of 300 km. Source depths of explosion vs. earthquake are indicated. Ccor is the value of the normalized correlation coefficient between earthquake and explosion.

is of course 1.0, but it is reduced by at least 40% for each of the other Green's functions. From a theoretical standpoint, discriminant performance comparable to the P_n discriminant might be anticipated. Waveform norms were computed for all possible source mechanisms by stepping through fault orientation angles on a 10° grid. The average correlation decrease of the explosion-earthquake was 45% with a minimum 28%. For noisy signals in a laterally varying earth, the performance of a correlation discriminant would undoubtedly be worse than these calculations indicate, but additional investigation seems warranted.

To complete this preliminary inquiry into the potential of the Pg waveform time domain discriminant, we have computed on a theoretical basis the expected trajectory of the average norm in a standard discrimination plot (see Figure 14). To compute the variation of a typical earthquake source with size we combined relationships of seismic moment to M_L and m_b (Taylor et al., 1988) with those for source duration with seismic moment for western North America (Somerville et al., 1987) to obtain

$$\text{Log}(\text{duration}) = 5.77m_b - 2.778$$

This relation has the same information requirements as the Mueller-Murphy source which we are using for our explosion calculations. It only requires an m_b value in combination with a depth scaling relation and a magnitude yield curve. Figure 14 shows the trajectory of the expected correlation of an explosion Pg waveform with an earthquake Pg waveform. The observed P_n correlations are shown for reference. The separation of the observed explosion population from the theoretical earthquake population is far from complete. However, there is clearly sufficient impetus to continue the investigations of the Pg discriminant further and every reason to believe the Pg waveform discriminant will be as good as any developed to date. We again emphasize the physically based nature (depth phases) of the P_n and Pg discriminants and the hope this offers for them to be widely transportable.

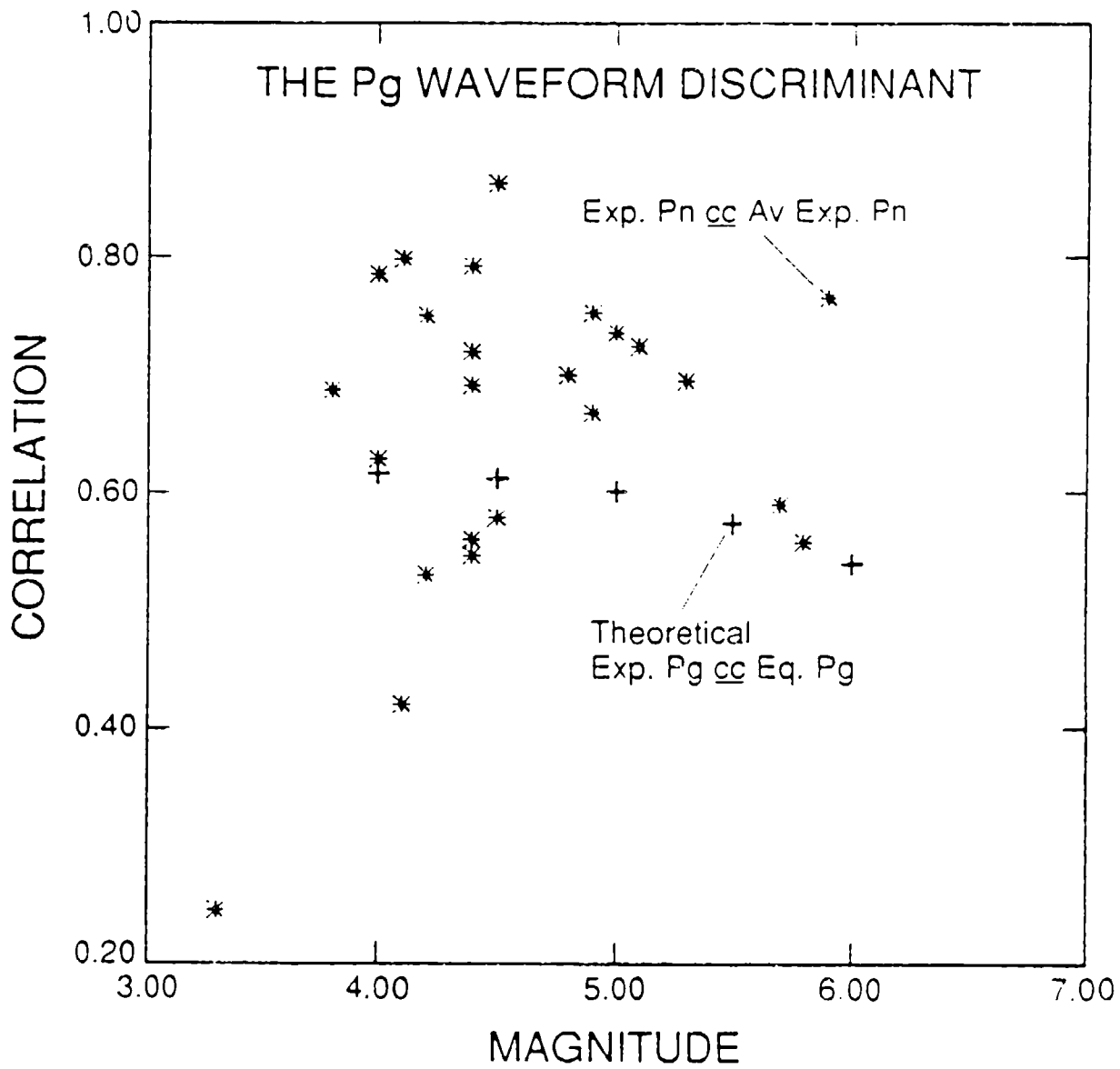


Figure 14. The discrimination performance of the theoretical cross correlation of Pg expl. to earthquake (crosses) is compared to the observed performance of the Pn discriminant.

UPPER MANTLE TRIPLICATIONS BENEATH ASIA

Introduction: Understanding the detailed structure of the seismic discontinuities of the Earth's upper mantle is of fundamental importance in the geosciences. This structure and its regional and lateral variations play an important role in geodynamics as well as providing constraints for compositional models of the Earth. The upper mantle P-wave velocity discontinuities have been studied in detail for many different regions (e.g., U.S., Canada, Europe, and west Asia). However, until recently, data recorded in central Asia have not been readily available, preventing the Asian plateau from being an area of prolific study.

In establishing the USA-USSR Joint Seismic Program, whereby an agreement between IRIS and the Soviet Academy of Sciences has been set forth, previously unavailable data can now be obtained. Decades of analog records from the Soviet national network are now available, and are similar in many respects to the World Wide Seismographic Station Network (Given, Helmberger and Zhao, 1991.) Many records from this database are already digitized and easily obtained from the Center for Seismic Studies (CSS). These data greatly increase the number of event-to-station paths in central Asia, as well as span a distance range bracketing the upper mantle triplications, enabling a detailed regional study of the upper mantle beneath central Asia.

In an effort to study the upper mantle P-wave velocity profile we analyze P-wave motions at distances where arrivals from the upper mantle triplications are clearly evident. The data used are digitized analog vertical component short period records of USSR underground nuclear explosions. A comparative approach is taken wherein USSR data are correlated with predictions made from upper mantle models presented in previous studies. These models were derived for distinctly different regions elsewhere on the globe, and are used here in an effort to gain a qualitative understanding of the lateral variations in the upper mantle of the different locales of central Asia.

Region of Study: A map of the study area is presented in Figure 15. The eleven stations from which we have short period analog data are presented as triangles. This array spans distances from around 5 to 40 degrees, sampling many different regions, as well as different tectonic settings. While the lithosphere in central Asia is comprised of the Russian Platform to the northwest, and

USSR Study Area

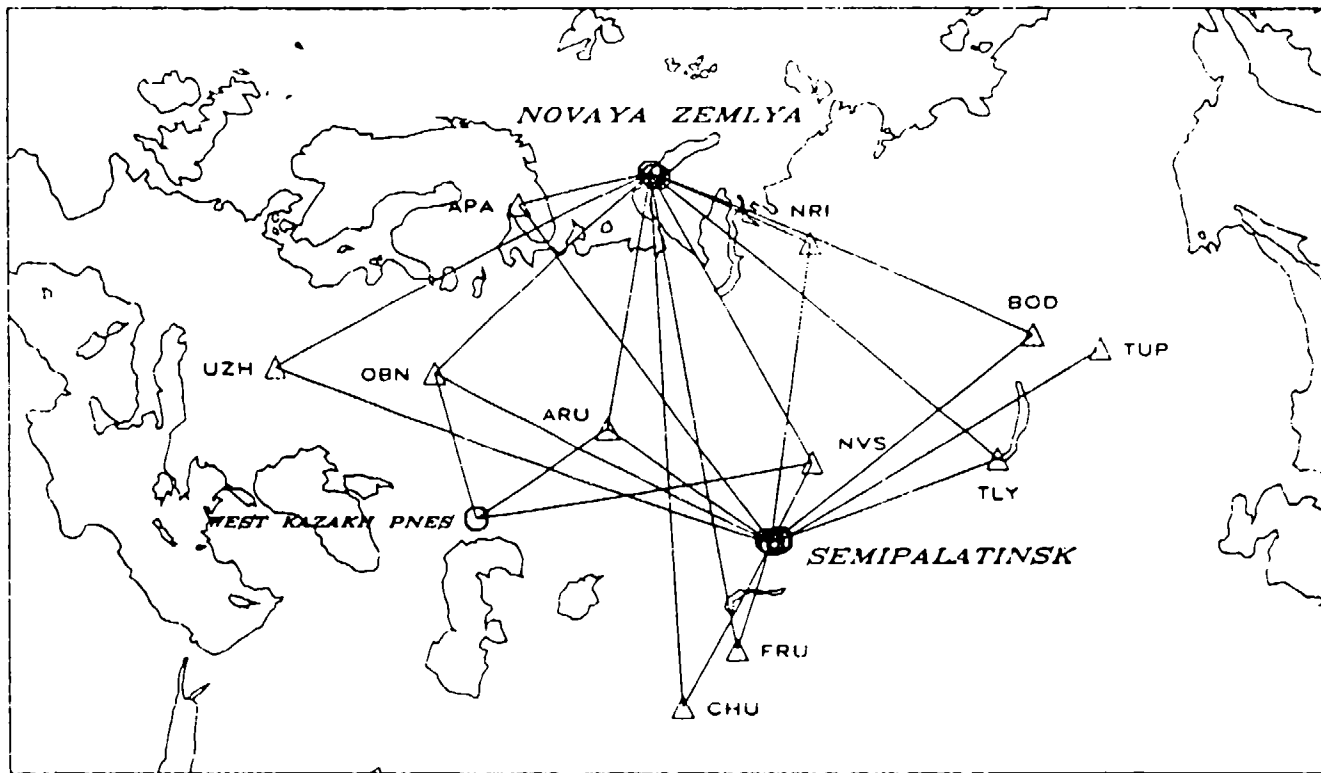


Figure 15. Map of Asia. 11 stations and 3 source regions used. Raypath coverage is good, adequately covering central Asia.

the West Siberian Platform to the north, the regions to the south and southeast are comprised of complex fold systems. The question of whether or not these fold systems are accompanied by tectonic rather than shield seismic velocities in the lithosphere is important, and will be investigated in this study. Also, lying between the West Siberian Platform (plains) to the north and the Northeast Siberian fold system (mountain ranges) to the east, is the Central Siberian Platform (plateau) to the northeast, where the possibility of some degree of a tectonic lithosphere, or transition zone between tectonic and shield regions, has not yet been addressed. Three stations are located in the southeast (BOD, TLY and TUP) which permits us to investigate such a possible transition zone. With two distinctly different and densely populated source regions, Novaya Zemlya and Semipalatinsk, there are many path geometries across Asia to investigate such lateral variations.

Comparative Modeling Technique: A comparative modeling approach was used in this study, whereby data were correlated with predictions made from models previously presented in the literature. The synthetics were generated by the generalized ray method (HelMBERGER, 1973a). The generalized ray technique was used because of its speed and cost-effectiveness. The procedure was to first generate Green's functions for the specific models and distances and then convolve them with empirical sources to obtain the predictions. Empirical sources were estimated by taking several P-wave waveforms at teleseismic distances where the triplication arrivals are well separated in time, taking care to choose records with good signal to noise ratio as well as minimal P-wave coda, keeping only the first arrival for convolving with synthetics (see Figure 16). Records chosen were typically beyond 26 degrees or so, a distance sufficiently past the 670 km discontinuity triplication crossover. P-waves with different source time functions were chosen so that comparing synthetics with the data could be easily accomplished by choosing the empirical sources having source time function characteristics matching those of the data to be modeled.

The Data Set: Our data set is a collection of 479 digitized short period vertical component records from 11 stations of the Soviet national network, recording 110 underground nuclear explosions. The number of events recorded at each station is presented in Figure 17a. Some stations are very densely populated, while others are sparse. The distance distribution of the events recorded for

SYNTHETIC SEISMOGRAM TECHNIQUE

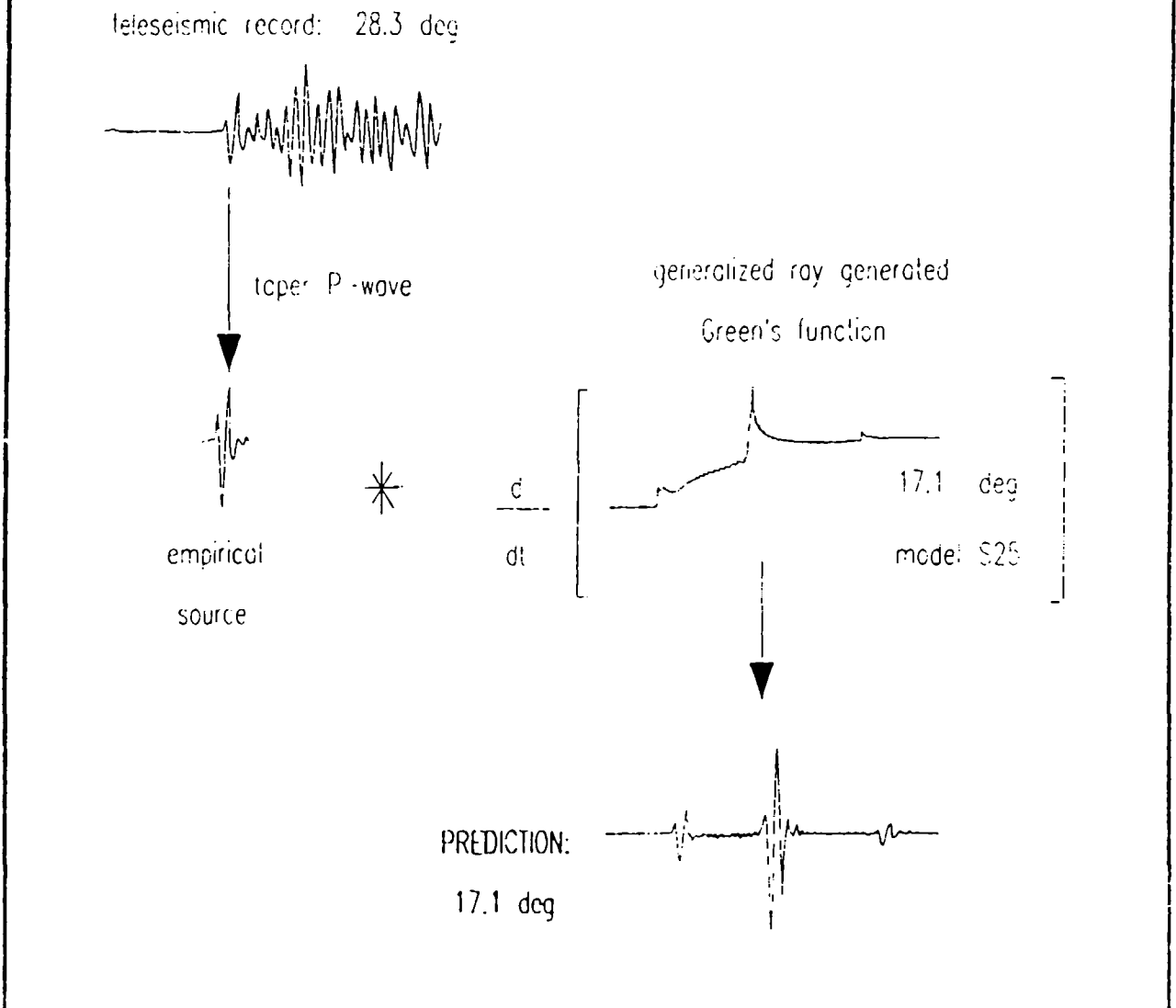
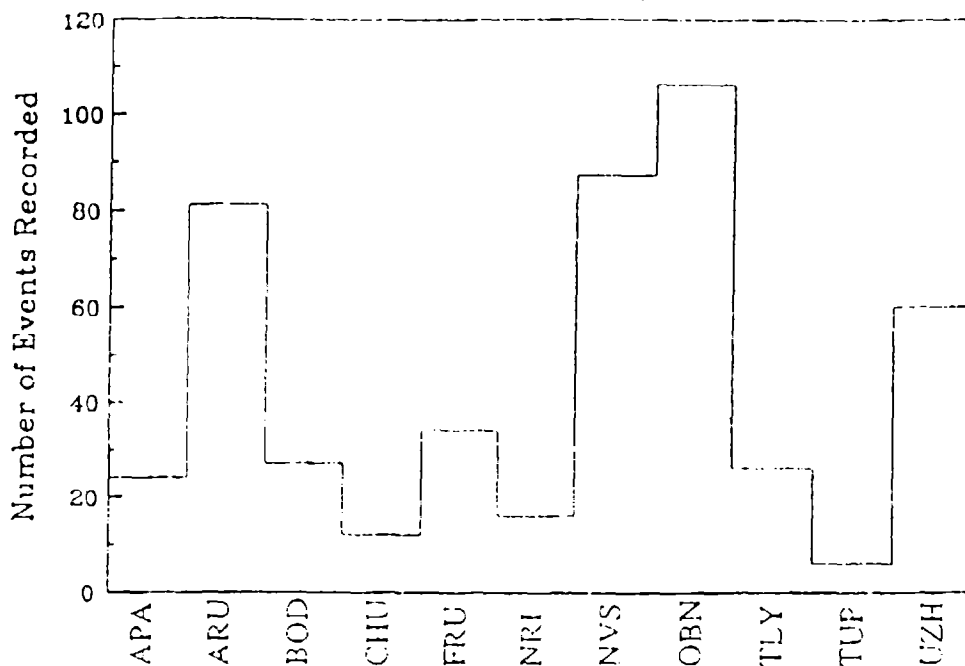


Figure 16. Synthetic Seismogram Technique. An empirical source time function is derived by tapering the P wave of a record where no triplications arrivals exist in the time window of interest. This is then convolved with the time derivative of a generalized ray generated Green's function to obtain the model prediction.

Short Period Analog Records

A)



Distance distribution

B)

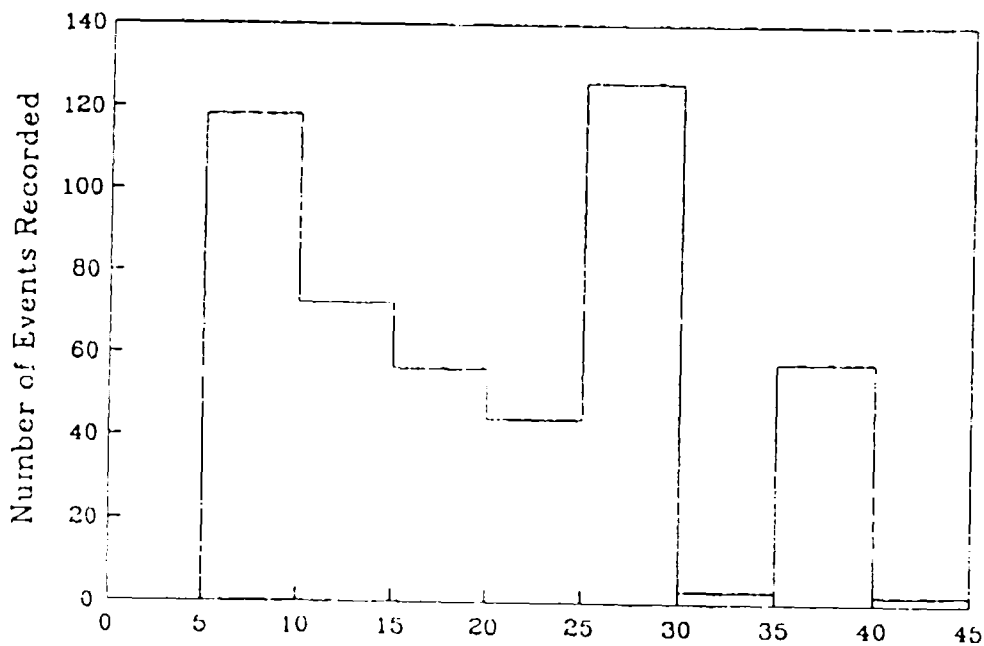


Figure 17(a) Population of events recorded at each station. The average is about 43 recordings per station. (b) The number of recordings plotted with respect to distance. Triplification distances are well populated for this data set.

this network is shown in Figure 17b. As this figure illustrates, the distances where the different triplication arrivals are routinely recorded from around 15 to 27 degrees are well populated. Nearly all of the 110 events are from the two main Soviet test sites, Semipalatinsk and Novaya Zemlya, with the exception of several off site Peaceful Nuclear Explosions (PNE's.) The Novaya Zemlya events are from the northern Matochkin site. The Semipalatinsk events are from 3 specific sites: Degelen Mountain, Koynstan and Shagan River. The Semipalatinsk events are plotted in Figure 18 using the USGS PDE locations. The data from each of the three Semipalatinsk sites were analyzed separately. The CKM-3 instruments recording these events are similar in nature to the World Wide Seismographic Station Network (WWSSN) short period instruments, peaking at around 1 second. This data set is easily obtained in digital form from CSS.

The controlled nature of the source-receiver geometries along with the abundance of the short period data makes it ideal to stack the data. Records were binned with respect to source regions and stations, and a separate stack was made for each station at each source site, provided sufficient data existed for any given path. Separate stacks were made for the three specific Semipalatinsk sites shown in Figure 18. Thus, for any given station, up to four stacks may have been made: one for each of the Semipalatinsk sites, and one for the northern Novaya Zemlya site. The data for specific paths contain similar waveforms, and after stacking, the triplication signals become enhanced while coda signals decrease in amplitude. The distance window for any site-receiver path usually varies no more than about 30 km, so the stacks were made by lining up the first arrivals of the waveforms. All amplitudes were normalized to unity before stacking. An example for the well populated station OBN is given in Figure 19. The distance window, using the USGS PDE locations, spans only about 7 km. The resulting stacked traces of the short period data set are used to model upper mantle structure. Records were stacked only for distances where triplication arrivals are clearly seen above the noise level. Records were not included in a stack if they had portions that were zero in amplitude presumably due to undigitizable sections of the original

SEMIPALATINSK SITES

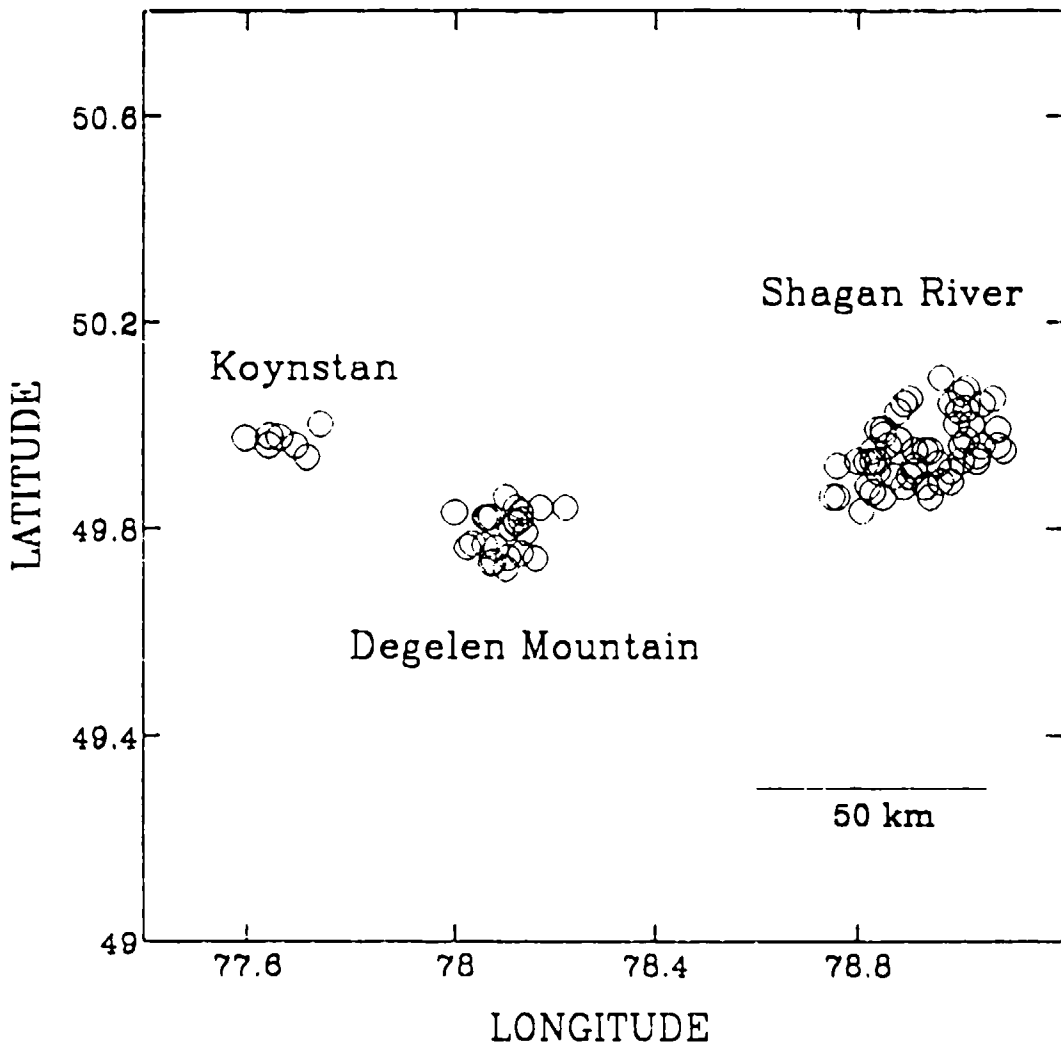


Figure 18. Location of events from three Semipalatinsk sites. The locations are from the USGS PDE. The data from each site were stacked separately.

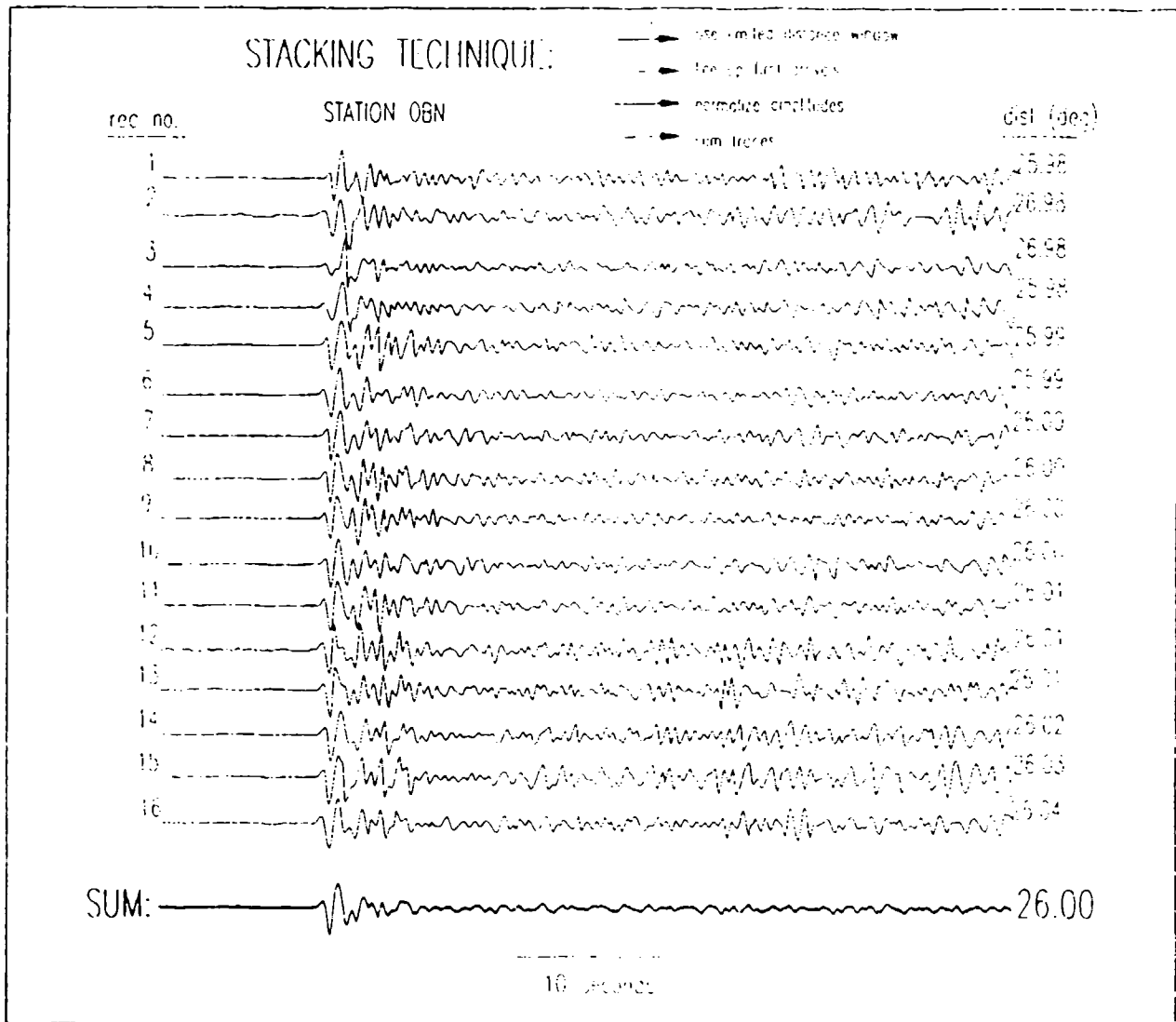


Figure 19. Stacking Technique. For a specific source region and station, the first arrivals are lined up, all amplitudes are normalized to the peak amplitude, then the traces are summed. The example given, for station OBN recording Shagan River events, the variation in distance spans about 10 km. The resulting sum exhibits enhanced triplication arrivals and suppressed coda arrivals.

seismograms. The total number of records fitting the above criteria is 183. For the binning of records chosen above, 20 stacks have been made, with the average number of records per stack being about 9 (Table 1).

Models for Comparative Study: Synthetic seismograms were generated for the distances in Table 1 for four different models. These synthetics were then compared to the data stacks in an effort to obtain a first order idea of the type of model necessary to explain the data for each path. The models chosen represent different types of lithospheric structure (Figure 20), such as a thick shield model (S25, LeFevre and Helmberger, 1990, Canadian shield), a model with no low velocity zone (KCA, King and Calcagnile, 1976, west Russia), and two models with a low velocity zone in the lithosphere, K8 (Given and Helmberger, 1980, northwestern Eurasia) and T7 (Burdick and Helmberger, 1978, western U.S.), where T7 is a tectonic model. Although these four models were derived for different regions of the globe, the comparison of their predictions to the Soviet data is important to assess the possible nature of the underlying upper mantle. The most important differences in these models are in the top 200 km. Second order differences are the depths of the "400" and "670" km discontinuities, gradients above and below the discontinuities, as well as the percent velocity increase of the discontinuities. For the rest of this paper we loosely use the numbers "400" and "670" to represent the two major upper mantle discontinuities, keeping in mind that their exact depth varies from model to model, as well as in the Earth.

Absolute Travel Times: The arrival times of the first arrivals of the large short period data set were usually very easy to measure due to the first arrival's impulsive nature. Records having low signal to noise ratio were not used in our travel time analysis. One of the uncertainties in the travel times is the use of the USGS PDE origin times (unfortunately, the origin times are not available from the USSR.) Also, the records came from CSS with a file of instrument time corrections that range from 0 seconds up to around 60 seconds. Up to three time corrections per day are listed for each station for the days that events occurred. In many cases, the clock error was not constant over the period of a day, and changed by as much as a second and a half. This

Table 1: Stacked Traces List

STACK NO.	STA NAME	DELTA (deg)	# RECS	SOURCE REGION	SITE NAME
1	ARU	13.43	3	Semipalatinsk	Degelen Mountain
2	ARU	13.75	4	Semipalatinsk	Shagan River
3	TLY	15.72	14	Semipalatinsk	Shagan River
4	ARU	17.09	9	Novaya Zemlya	Matochkin Shar
5	OBN	19.76	7	Novaya Zemlya	Matochkin Shar
6	NRI	20.14	4	Semipalatinsk	Koynstan
7	NVS	21.86	8	Novaya Zemlya	Matochkin Shar
8	BOD	22.01	4	Semipalatinsk	Shagan River
9	BOD	22.49	3	Semipalatinsk	Degelen Mountain
10	NVS	22.87	4	W. Kazakh	PNE
11	APA	24.36	2	Semipalatinsk	Degelen Mountain
12	APA	24.60	2	Semipalatinsk	Shagan River
13	OBN	25.22	5	Semipalatinsk	Koynstan
14	TUP	25.28	5	Semipalatinsk	Shagan River
15	OBN	25.56	17	Semipalatinsk	Degelen Mountain
16	OBN	25.96	39	Semipalatinsk	Shagan River
17	BOD	27.44	9	Novaya Zemlya	Matochkin Shar
18	UZH	28.31	5	Novaya Zemlya	Matochkin Shar
19	TLY	29.88	5	Novaya Zemlya	Matochkin Shar
20	UZH	36.20	31	Semipalatinsk	Shagan River

Model	Region	Reference	Data
S25	Canada	Lefevre & Helmberger, 1990	LP Body waves
KCA	W Russia	King & Calcagnile, 1976	SP Body waves
K8	NW Eurasia	Given & Helmberger, 1980	SP & LP Body waves
T7	Western US	Burdick & Helmberger, 1978	LP Body waves

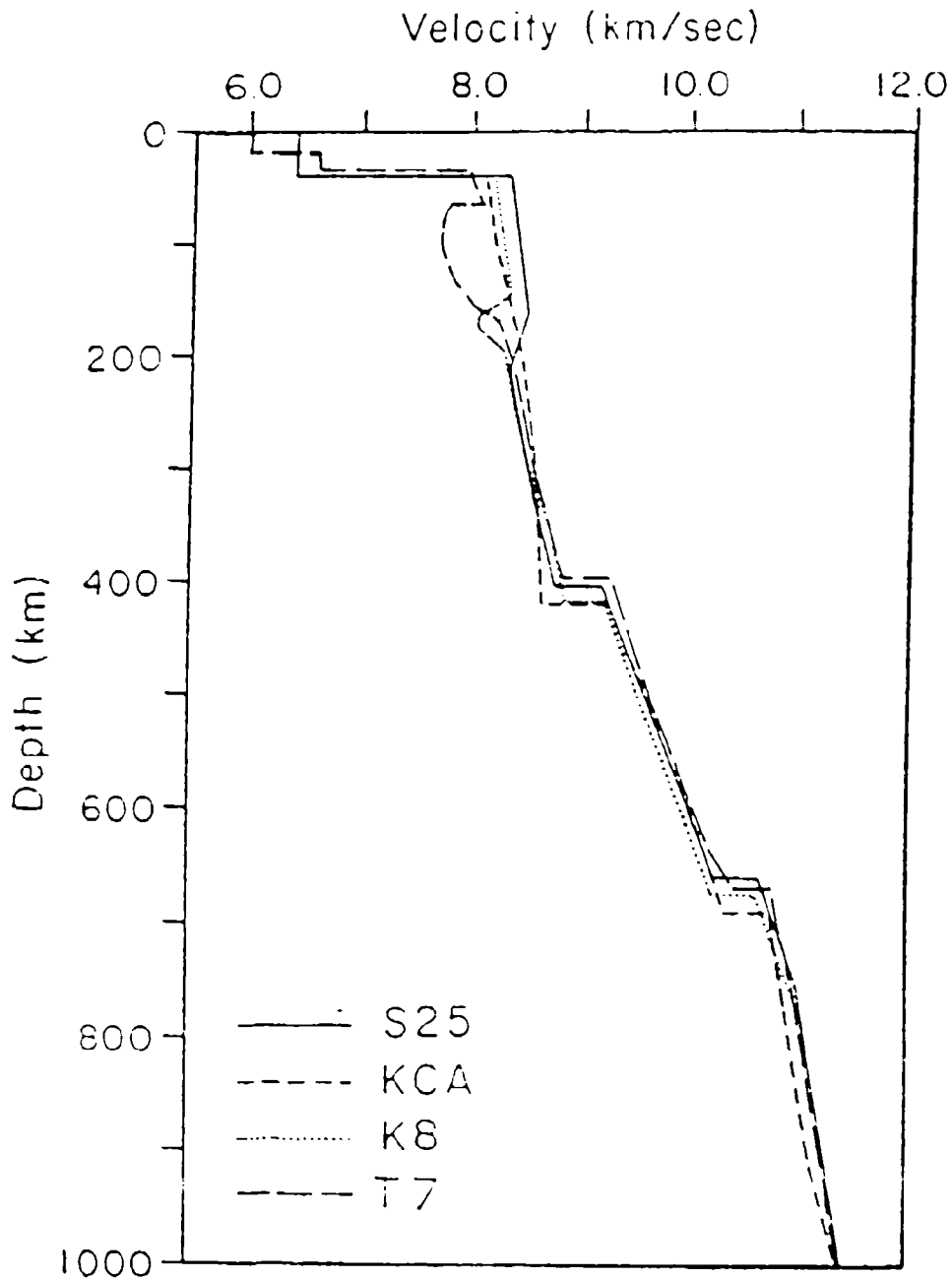


Figure 20. Velocity Models. Four models were used in this study for comparison with the data stacks. The most outstanding differences in the models are in the uppermost 200 km of the mantle. S25 has a fast thick lid and a gradual low velocity zone, T7 and K8 have pronounced low velocity zones, and KCA has no low velocity zone.

may be another source of travel time error. For cases where the clock error changed within a day, we interpolated the given time corrections for that day to the P-wave arrival time for that day's event, assuming the clock error changed in a linear fashion

First arrival travel times are shown in Figure 21 with the predictions of model KCA. Anomalies are clearly visible on this figure, especially at 15.7 degrees (station TLY) where the first arrival is as delayed as the discontinuity reflection. This may be a slow tectonic path from the Semipalatinsk region.

With the uncertainty in travel times due to origin time, along with the data being grouped at very discrete distances as seen in Figure 21, a $\frac{dt}{dx}$ investigation is not possible. Furthermore, because of these uncertainties, we choose not to use absolute travel times from this data set as a discriminant for choosing between the different models.

Waveform Comparisons: As Figure 15 indicates, our study area has good coverage of the central Asia area. However, the source-receiver geometry is such that no given path from a source region has more than one station on it. Without a profile of stations for a specific path, obtaining a unique solution model is not possible. While deriving a definitive model is not practical in this situation, comparisons with model predictions can still be made to assess agreement with different classes of models and assess lateral variation from path to path.

Predictions for the four models K8, KCA, S25 and T7 are compared to the data stacks in Figure 22. Nine panels are presented, in each of which the top trace is the data stack, and the four underlying traces are model predictions. The time window shown is 30 sec, and the prominent arrivals are a function of distance. An example of the relative timing order of the triplication arrivals is seen in the travel time curve for KCA in Figure 21. Up to around 21° the first arrival is the direct P from above the 400 (P_{AB}), and the second arrival is the combination of the reflection off the top of the 400 km discontinuity (P_{BC}) and the P wave from below the 400 (P_{CD}). In some cases, the reflection off of the top of the 670 (P_{DE}) along with the direct arrival from below the 670 (P_{EF}) are evident as a third arrival. For these distances, the goodness of fit criteria are how well waveforms, amplitude ratios and differential travel times in the synthetics agree with the

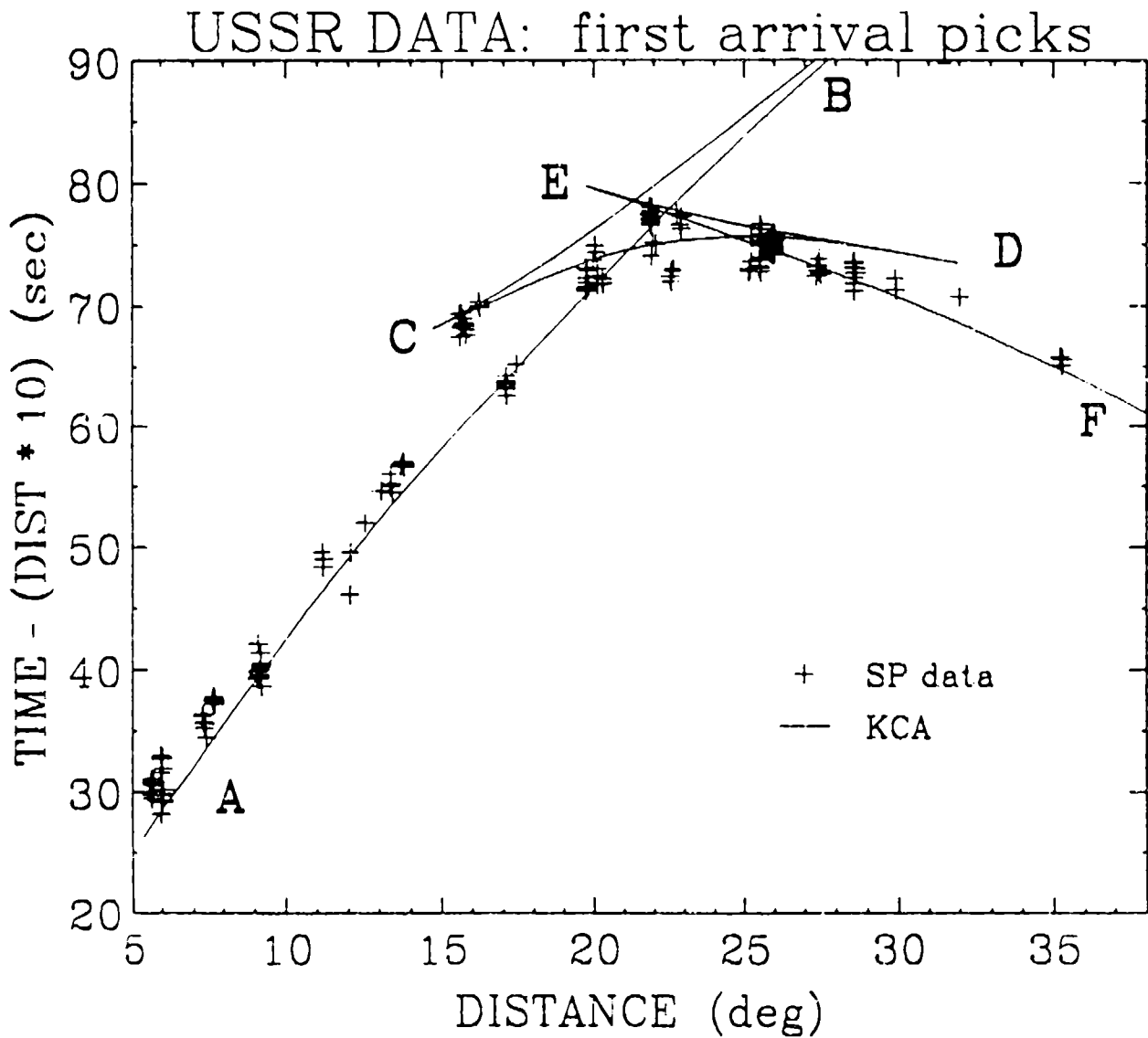


Figure 21. First Arrival Travel Times. First arrival picks of the short period data made from impulsive waveforms only are shown here with the prediction of model KCA. The letters A through F represent the names of the different triplication branches.

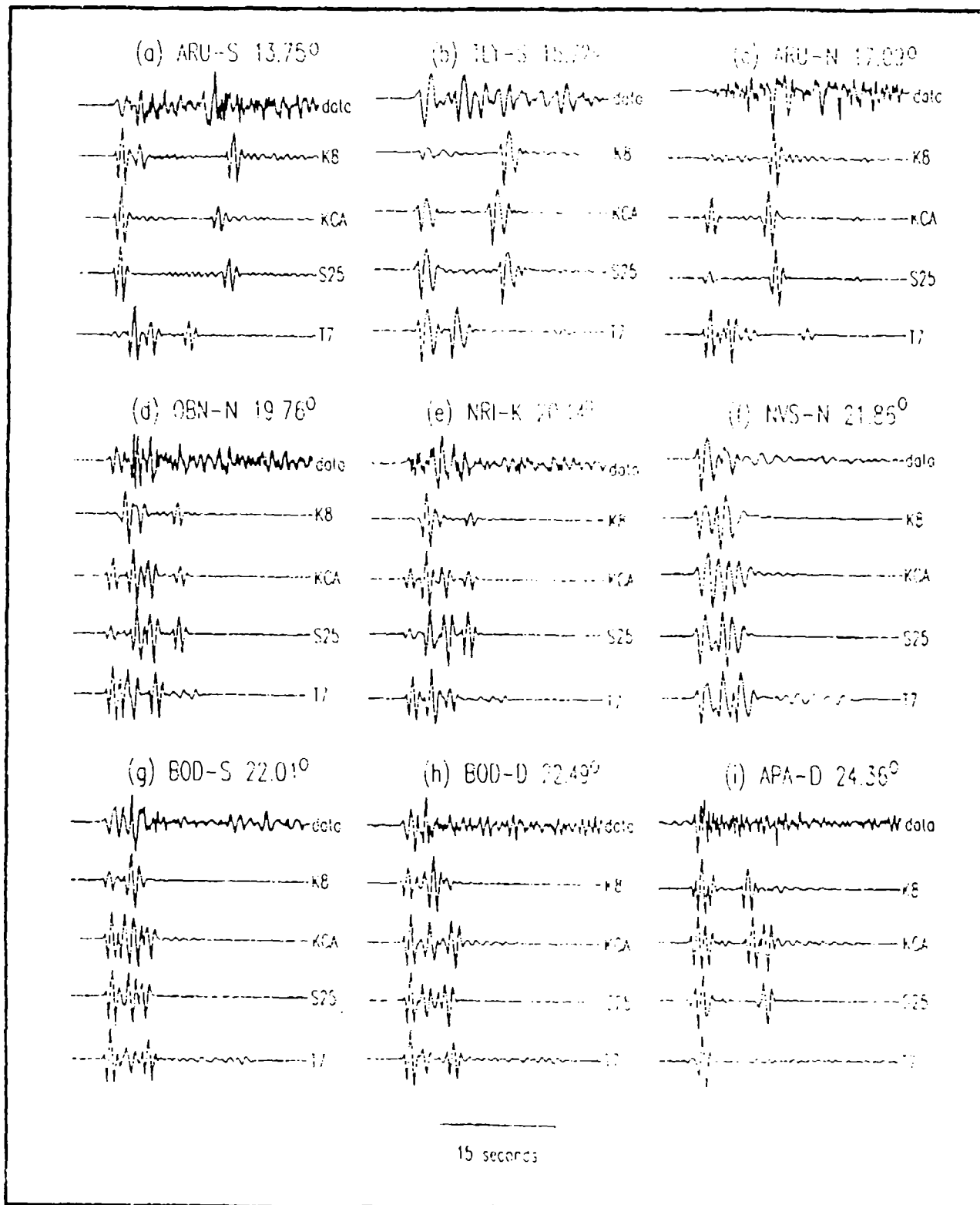


Figure 22 (a) through (i) present data stacks (top trace) and the predictions of the four models (bottom four traces.) Comparisons are described in the text

data. This distance window corresponds to Figure 22 (a) through (d). From right before the crossover distance of the P_{AB} and P_{CD} , to a little after the crossover of the P_{CD} and the arrival from below the 670 (P_{EF}), the differential time between the triplication arrivals is often too small to measure. This corresponds to Figure 22 (e) through (h), where at least two arrivals appear as more of a wave packet than distinct arrivals. The shape of these wave packets (data and synthetics) are very sensitive to the amplitude ratios of the different arrivals, and thus can be a good diagnostic tool to distinguish between different possible models. Beyond the crossover distance of P_{CD} and P_{EF} the arrivals separate in time so that differential travel time information again supplements the amplitude ratios.

The degree of fit of the model predictions to the data stacks varies from good to poor. In some cases differential travel time information is well predicted, but amplitude behavior is not. Also, the short period data is undoubtedly affected by site structure reverberation, which we make no effort to account for here other than attempting to suppress this affect in the stacking process. Nonetheless, the triplication arrivals are usually strong and clear in this data set. Data from many of the paths to the west of the test sites in Figure 15 are better modeled in the first order sense by a shield or shield-type model. Data to TLY to the east from Semipalatinsk, however, is better modeled by the tectonic western US model T7. Figure 22 (b) shows the data stack and predictions for station TLY at 15.7° . Only model T7 predicts the anomalously small differential travel time between P_{AB} and P_{CD} due to its slow lid. To a slightly more northerly azimuth is station BOD. Figure 22 has two central Asian stacks for BOD. With about a 0.5 degree difference in distance, Figure 22 (g) is for the Shagan River site, while Figure 22 (h) is for the Degelen Mountain site. For Figure 22 (g), the prediction from K8 is the best. Increasing in distance 0.5° (Figure 22 (h)) yields a record that is poorly modeled by all four models. It is possible that the path to BOD from Semipalatinsk may coincide with a transition region or boundary between the tectonic region to the south and a more shield-like lithosphere to the north, producing complex records.

Station OBN recorded many events from the three Semipalatinsk sites. The three resulting OBN data stacks and model predictions are presented in Figure 23. For this distance, the first arrival is P_{EF} and the second arrival is a combination of P_{CD} and P_{DE} . Around 8 or 10 sec after the first arrival, the back branch of the 400 triplication consisting of P_{AB} and P_{BC} can be seen in the synthetics. A remarkable feature in the data in Figure 23 is the rapid diminishing with distance of the second arrival (P_{CD} and P_{DE} .) This feature is not predicted in the synthetics. Given and HelMBERGER (1980) presented data in this same distance window from Semipalatinsk to an azimuth to the southwest recorded at TAB (Tabriz, Iran.) For that azimuth, the changing amplitude ratio of the first two arrivals is well predicted by K8 (Figure 24). The OBN data appears anomalous in that the second arrival decays so rapidly in such a small distance window of around 0.8° . This feature of diminishing P_{CD} and P_{DE} relative to P_{EF} in a small distance window (i.e., move the tip of the triplication to a smaller distance) may be more accurately modeled by increasing the velocity gradient between the 400 and 670 discontinuities. Increasing the gradient causes down-going rays in this depth range to turn up more sharply. Thus the deepest possible ray propagating above the 670 discontinuity, i.e., the arrival at the tip of the D branch, is bent up to a smaller distance.

Station TUP has an azimuth from Semipalatinsk intermediate to that of stations TLY and BOD for that same source region. For this path, the distance to TUP is 25.28° . This distance is in the window of that presented in Figure 23 to station OBN, though the waveforms are quite different. The source time function of the TUP record is longer period, which may partly obscure any differentiation between the two triplication phases that are arriving just a few seconds apart. Also, if these waves propagate along a transition zone from a tectonic lithosphere to that of a shield, complexities should be expected. Figure 25 (a) displays the stack for TUP and the synthetics. The prediction from model K8 gives the closest fit, though it is still poor. The prediction from the tectonic model T7 is not as good as that of K8. It is possible that the transition from tectonic to shield is abrupt because the T7 model is the only model that adequately predicts the record from the neighboring path to the south at station TLY (Figure 22 (b)). For paths to TLY, TUP and BOD from Semipalatinsk, the models K8 and T7 produce motions closest to our observations. This

STATION OBN Central Asia

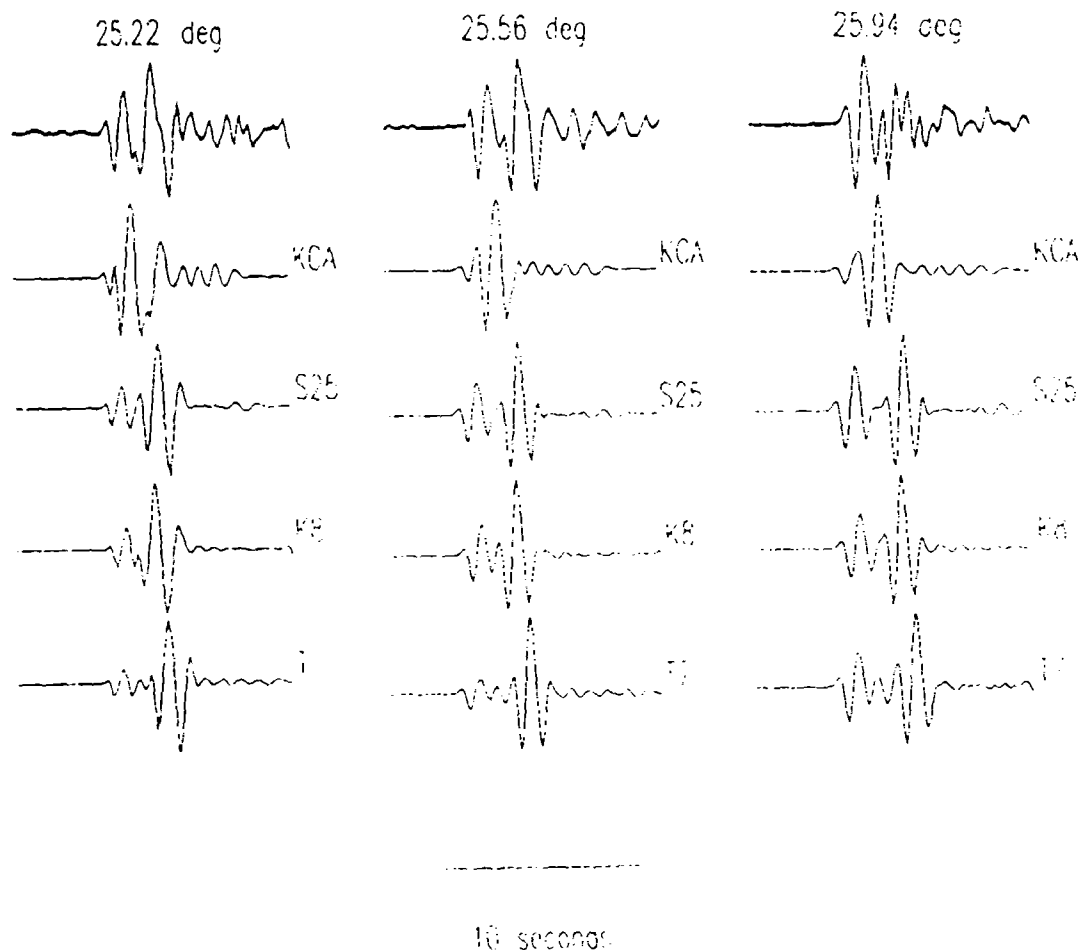


Figure 23. OBN from Semipalatinsk. The three columns are separate stacks for the 3 sites in Figure 4 and model predictions for that specific distance. For these distances, the reflection off the 670 arrives around 2 or 3 seconds after the first arrival, and the arrival of the 400 arrives around 7 or so seconds after the first arrival. (For this distance range, only S25 predicts a visible 400 arrival, and it is very small. This source-receiver pair shows no strong sign of an arrival from the 400.) At 25.22, S25 and K8 produce reasonable fits to the data stack. But as the distance increases, the 670 arrival in the data diminishes rapidly, and this behavior is not predicted by any of the synthetics.

Semipalatinsk to Tabriz, Iran

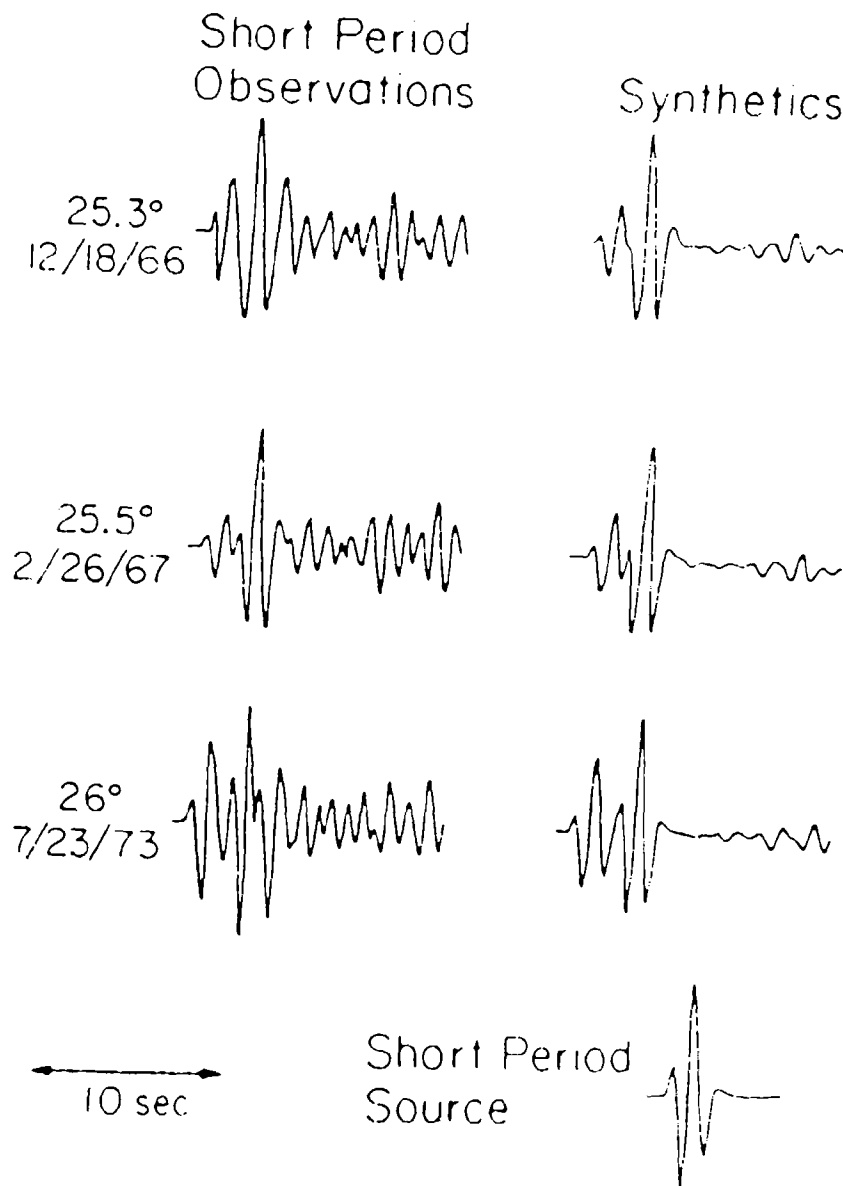


Figure 24. Three Semipalatinsk events recorded at TAB (Tabriz, Iran) are shown here with K8 synthetics (from Given and HelMBERGER, 1980.) The amplitude ratio of the first two arrivals is well predicted by K8 for this southwest azimuth from Semipalatinsk.

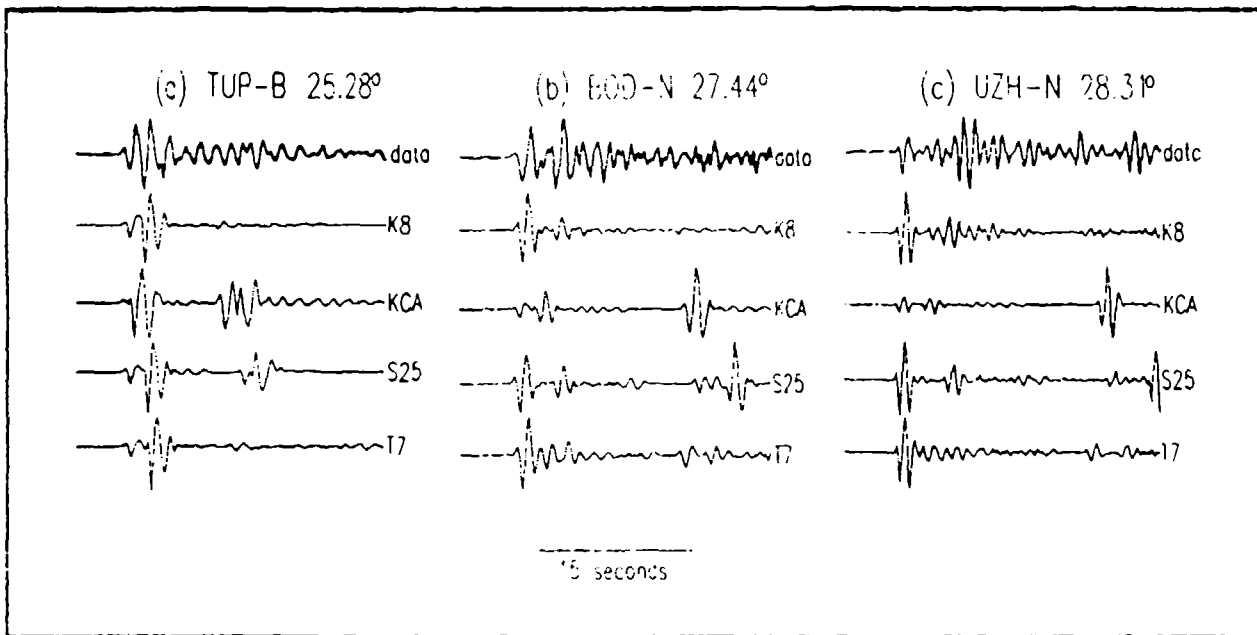


Figure 25. (a) through (c) present data stacks (top trace) and the predictions of the four models (bottom four traces.) Comparisons are described in the text.

implies that over a lateral distance of around 500 km or so, the low velocity zone might drastically change from one like that in T7 to one like that in K8. Finer modeling with broadband data is necessary to resolve such issues.

For larger distances (Figure 25 (b) and (c)) the predictions widely vary for the four models presented here. The observed amplitude ratio of the first two arrivals in each of (b) and (c) is not predicted by the synthetics. Also, models KCA and S25 predict a large late arrival that has reflected off of the 400 km discontinuity. This is not seen in the data. If the large second arrival in the data is P_{CD} with P_{DE} , then S25 does better than the other models in predicting the differential travel time, though the amplitude ratio prediction is very poor. Modifications in the fine details of the gradients above and below the discontinuities are necessary to model these two paths.

Discussion: The four models chosen for this comparative study represent widely varying upper mantle rheologies. All four models were derived from body wave studies. KCA is a logical choice as a comparison model because it was derived from short period data in the western Russia region. K8 was chosen because it has a shield-like lithosphere as well as being derived for parts of central Asia that coincide with our study area. K8 was constructed using KCA as a starting model, utilizing both short and long period data from Soviet explosions. A classic shield model is S25, derived for the Canadian shield region using long period earthquake data. A first order justification in choosing S25, a model that was derived for a completely different locale, is that central Asia is thought to be shield-like, with the East European Craton to the west and the Siberian Craton to the east. This choice has proven useful, as S25 is a best-fitting model for several of the paths in our study area. To assess regions where tectonics are thought to play an important role, model T7 was utilized. T7 was derived for the tectonic western US from long period body waves of earthquakes and explosions. Other models in the literature may have done equally well for our criteria of choosing four models with fundamentally differing lithospheres. We note again that our choice of models is to emphasize regional and lateral variations in the upper mantle beneath Asia, and not to make an argument for specific models for the specific locales.

We have not used absolute travel time information in our modeling procedure. Due to uncertainties in hypocenter information, we are unable to analyze travel times at well populated stations with array data techniques. However, we can still make qualitative comparisons between the different stations. For example, data recorded at TLY from Semipalatinsk are anomalously slow by up to 8 seconds when compared to KCA predictions (Figure 21, 15.7°). Absolute travel times for the direct P waves at this range for the various models show considerable differences. The largest difference is between S25 (pure shield) and GCA (pure tectonic, Waick (1984)) is roughly 13 seconds. The travel time for GCA at 15.7° is over 10 seconds slower than that of KCA, which brackets the TLY times in Figure 7. T7 predicts an arrival time near 3 seconds earlier than the TLY data, though modifications in the direction of a more tectonic model makes matching these observations possible.

The 13 source-receiver paths that are most relevant to upper mantle triplication distances are presented in Figure 26 along with the best-fitting model for that path. For some paths, two models are listed because predictions from either model may be considered as a better fit than the others. The model name is in parentheses if the best-fitting model for that path poorly predicts observed motions. If no model came close to predicting observations, a question mark is shown. A comparative study has been presented in this report, so that the four models in Figure 26 are primarily meant to give a first order view of the upper mantle regimes beneath Asia, as well as possible lateral variations from locale to locale. All of the models used in this study have a LVZ, with the exception of KCA. Only one path favored KCA (station OBN from Novaya Zemlya), with predictions from S25 being equally satisfactory. A first order qualitative conclusion from this comparative approach is that from the four models chosen for comparison in this study, the north and the west regions of our study area favor shield (S25) or shield-type (K8) models, while the area to the southeast is probably a transition zone from a shield-type mantle to a more tectonic upper mantle (T7). A more detailed modeling approach is necessary for each path to make more quantitative inferences about the structure of the underlying mantle.

Paths and best fitting models

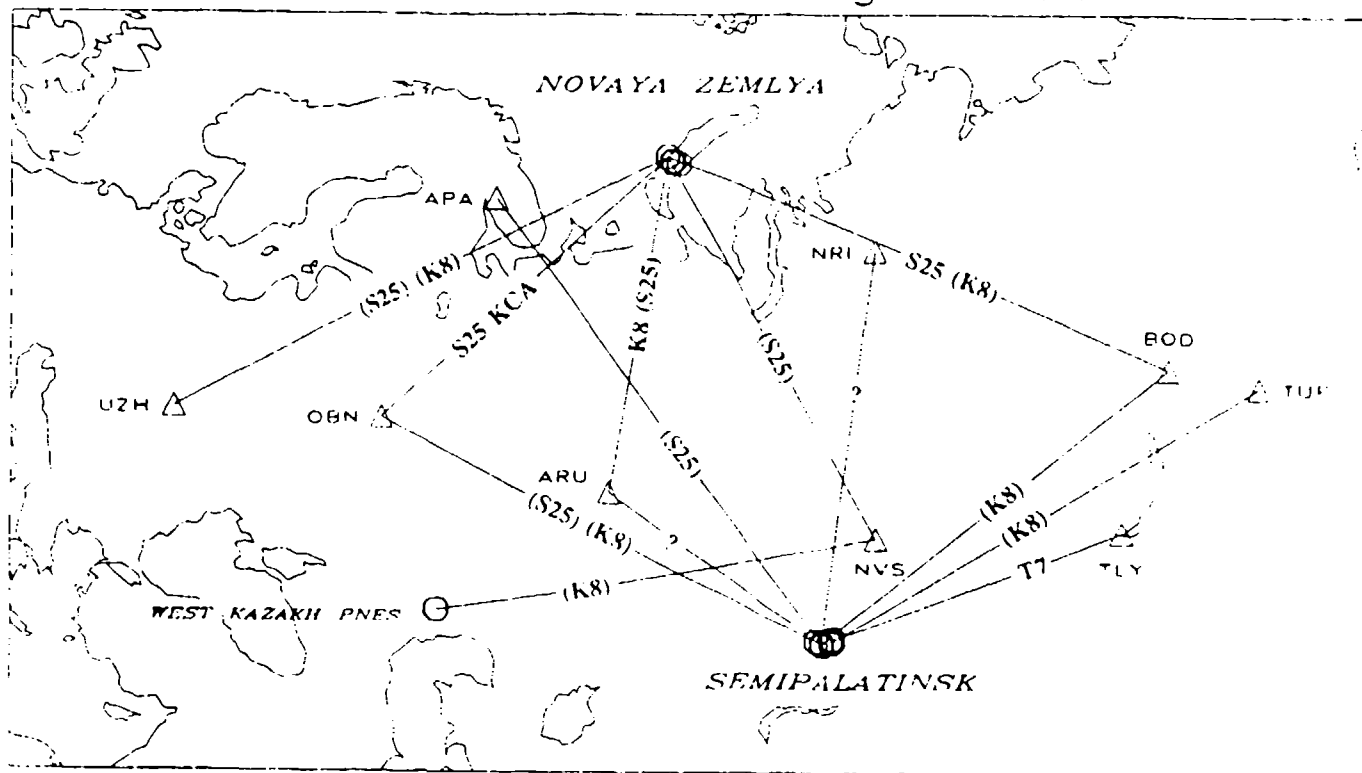


Figure 26. Best fitting models for this data set are written on the wave-paths. If the best fitting model or models do a poor job at best in predicting observations, the model name is put in parentheses.

Several paths in this data set produce motions that are poorly predicted by the above models. For example, the paths from Semipalatinsk westward to stations ARU and OBN are close in azimuth and are poorly modeled. For ARU, the differential travel time and amplitude ratio of P_{AB} and P_{CD} in the data are not predicted in any of the synthetics (Figure 22a). For OBN, rapid decay of the second arrival in a very short distance window is seen in the data and not the synthetics (Figure 23).

In the case of station OBN, the diminishing second arrival at 25.96° can be attributed to an early ending of the "D" tip of the 670 km triplication. To produce such a feature in the synthetics, changes must be made to the model in the transition zone. Model changes made far above the 400 km discontinuity tend not to diminish the amplitude of the second arrival enough to match the data. Support for this statement is seen in Figure 23 in that four very different lithospheric structures fail to produce a diminished second arrival. One way to end the 670 km triplication at a smaller distance would be to include a small zone of an increased velocity gradient on the top side of the 670 discontinuity. This turns rays up more sharply, thus decreasing the distance where the "D" tip occurs. An example of such a scenario is presented in Figure 27. The left column of synthetics is from K8, whereas the middle column is from K8.1, where K8 has been modified by a small zone of increased gradient right above the 670 discontinuity. The prediction of K8.1 at 26.0° adequately suppresses the second arrival. It has been recently proposed that the depth of the 670 km discontinuity may vary by as much as 20 km. Note also that the depth of this discontinuity for different regions of the globe has been placed anywhere from around 640 km to 690 km in the literature. A 670 km discontinuity occurring at a more shallow depth would also give rise to the "D" tip of the triplication ending sooner. An example of the discontinuity raised by 17 km along with a slightly increased overlying gradient is presented in the third column of Figure 27. This model K8.2 also predicts the correct amplitude behavior at 26.0° . These types of forward modeling calculations can be carried out at each station. Although we note here that the non-uniqueness due to the source-receiver geometry prevents the validation of such results.

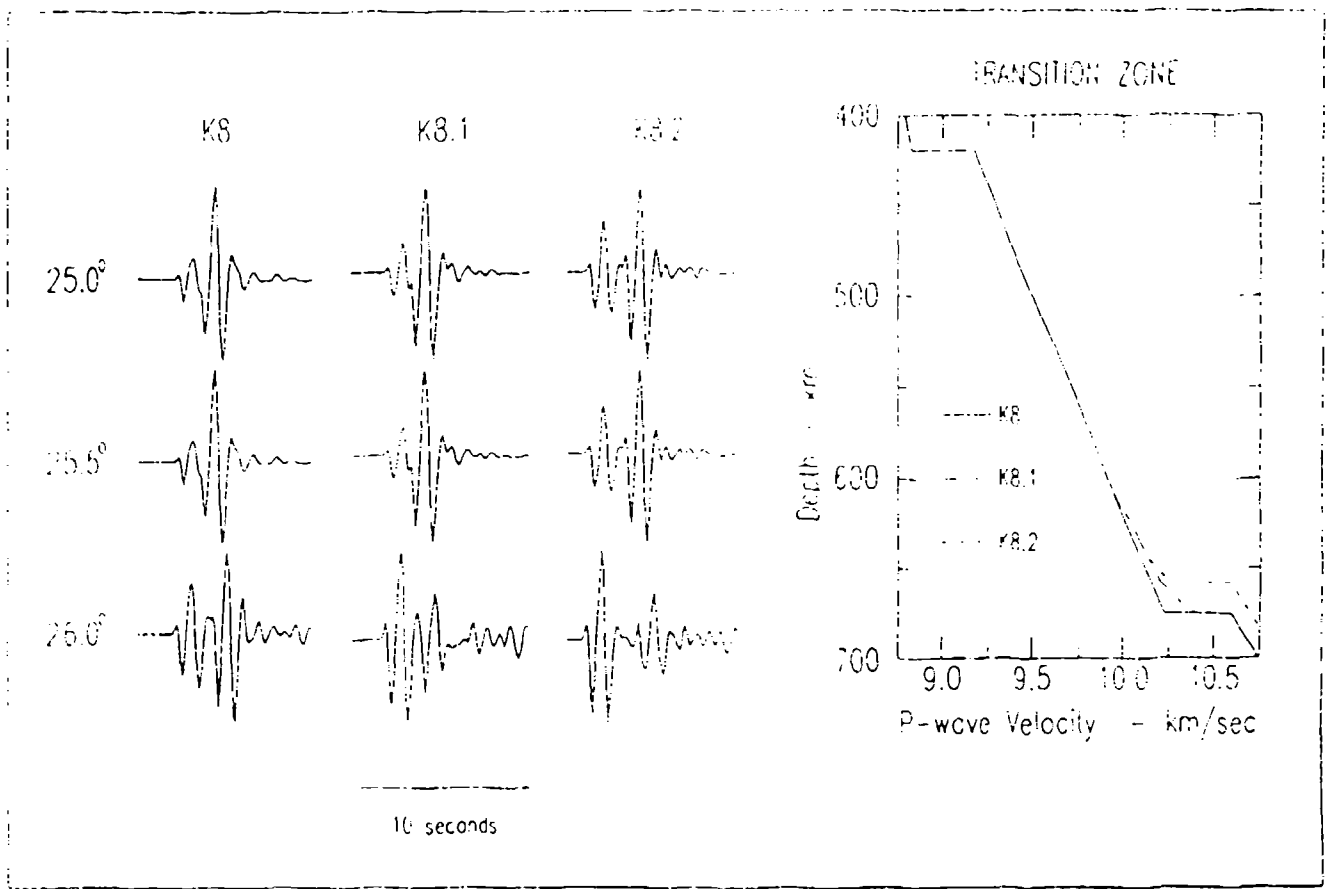


Figure 27. Predictions are plotted from K8 and two models with increased transition zone gradients, where one has a more shallow 670 discontinuity by 17 km. The amplitude ratio of the first two arrivals for K8.1 and K8.2 is opposite of that for K8. This amplitude behavior is seen in the data at OBN.

Recently, there has been renewed debate over the existence of a 520 km discontinuity. Synthetics were made for a model D25 (Jones and Helmberger, 1991), a model where S25 was modified by adding a 1 percent velocity increase at 500 km depth, and to preserve travel time the increase in velocity at 670 km was decreased. In comparing D25 synthetics with the data, a discontinuity of this nature is not supported by the short period data stacks in this study.

With broadband data from the Soviet Union becoming more available, future work for this region will include a detailed forward modeling effort. By using other stations in the Soviet national network that were not included in the CSS data set, along with selected earthquakes, a better view of the Asian upper mantle may be constructed. For the source-receiver geometry inherent in this data set, wave paths are typically isolated such that no multi-station profiles exist for any path. For this reason we have not explored solution models for any of the data due to non-uniqueness.

COMPOSITION OF REGIONAL P_n and S_n WAVEFORMS RECORDED
IN THE U.S. and U.S.S.R

Introduction: With the methodologies available to compute high-frequency full-wave responses both for vertically and laterally inhomogeneous crustal media, the broadband modeling of regional displacement seismograms has become a topic in many recent studies for retrieving the source and propagation path characteristics (Barker, 1991; Burdick *et al.*, 1991; Helmberger *et al.*, 1991; Zhao and Helmberger, 1991). The method of Cagniard de-Hoop is generally used to understand the composition of various seismic phases that the source process and the propagation effect together make up at a receiving station. This method requires many generalized rays to be tracked between the source and the receiver. As the crustal medium becomes complicated, the method can quickly become quite cumbersome with the process of just tracking the rays. For this reason alone, the method developed based on the frequency-wavenumber integration/reflectivity approaches is highly useful. This later method is computation intensive, but with the advent of fast computers and vectorized machines this is no longer a constraint on the methodology.

At high frequencies the effects of scattering in the crust become so intense that only statistical properties of wave forms are meaningful. However, one exception to this generality involves the long-period P_n and shear-coupled P waves at regional (1° - 15°) ranges (Helmberger, 1972, 1973). In a recent study, Saikia and Burdick (1990) showed that the short-period P_{nl} waves (period as short as 2 s) are also stable. They studied many observations from the Nevada Test Site (NTS) explosions recorded at regional distances of 200 to 420 km and modeled the P_{nl} waveforms using a deterministic crustal waveguide. The sources of these waveforms were shallow. Also, the sources were predominantly isotropic, and the portion of P_{nl} waves which was included in the P_n and P_g waves had a duration of about 30 s and was dominated by compressional waves. To understand the observed data, Saikia and Burdick (1990) employed the following strategy. They used the frequency-wavenumber algorithm (CODE: FILON_AS, written by Chandan K. Saikia, Woodward-Clyde Consultants) to compute the explosion generated P_{nl} waves for several canonical crustal models and selected a crustal model based on the agreement between the data and the

synthetic seismograms. The crustal model was then utilized to understand the composition of the P_g wave group which was constituted of phases like PmP, pPmP, 2PmP, PmS, pPmS, PmPSmP, PmSPmP etc. P_g is a constituent wave group whose frequency content is widely used to discriminate events. In this study, we have taken a similar strategy to investigate the broadband composition of P_{nl} and S_{nl} seismograms recorded in the North American continent at regional distance from double-couple sources and of the P and S waveforms that are recorded within the Soviet Union. We shall mainly focus on identifying the rays important to model the regional waves within the S wave window.

Data: For the U.S. study, we used a set of three-component broadband seismograms recorded at Harvard (HRV) station at a distance of 640 km from the Saguenay earthquake of November 25, 1988 (Figure 28a). These seismograms were recorded on a Streckeisen seismometer. We selected these seismograms because many features recorded on the seismograms were successfully modeled by Zhao and Helmberger (1991). Beginning with their crustal model, we have directed our study towards the modeling the high-frequency details observed in the P_{nl} waves and the composition of waves identified as S_n and sS_n by Zhao and Helmberger (1991) using a multiple source model. A similar study was directed towards the modeling of the broadband seismograms recorded within the Soviet Union. We selected a set of three-component seismograms recorded at GARM from an earthquake which originated at a distance of 200 km at an azimuth of 290° on May 4, 1989 (38.73°N and 78.5°W , Figure 28b). Unlike for North American earthquakes, the waveforms of very few Soviet Union earthquakes have been modeled. Thus, it is necessary to develop a starting crustal model even to obtain a first-order agreement between data and synthetic.

Modeling of HRV Seismograms from the Saguenay Earthquake: Figure 29 shows the broadband displacements recorded at Harvard station. To investigate the influence of crustal structure on the various significant phases of the P_{nl} window, we have started with the crustal model shown in Figure 30 by dotted lines. This model extends from the surface to a half space at a depth of 55 km. The major velocity discontinuity is at a depth of 55 km where the P velocity jumps from 6.71 km/s to 8.1 km/s and the S velocity jumps from 3.82 km/s to 4.7 km/s. Zhao and Helmberger

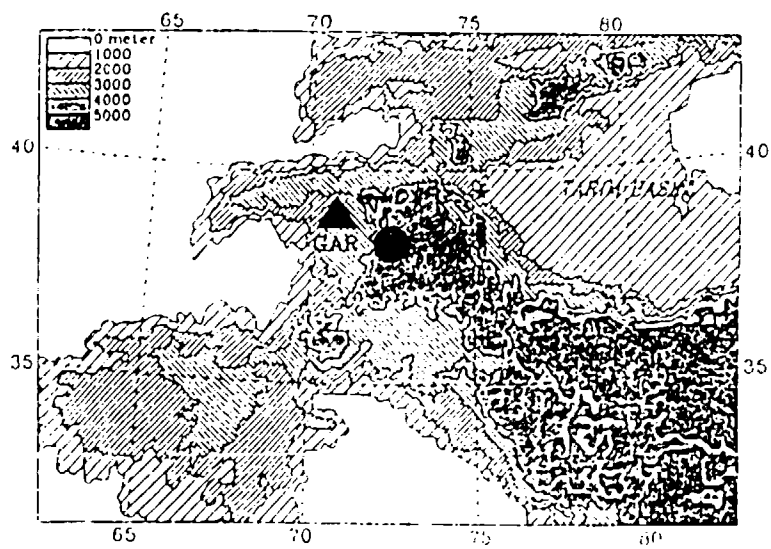
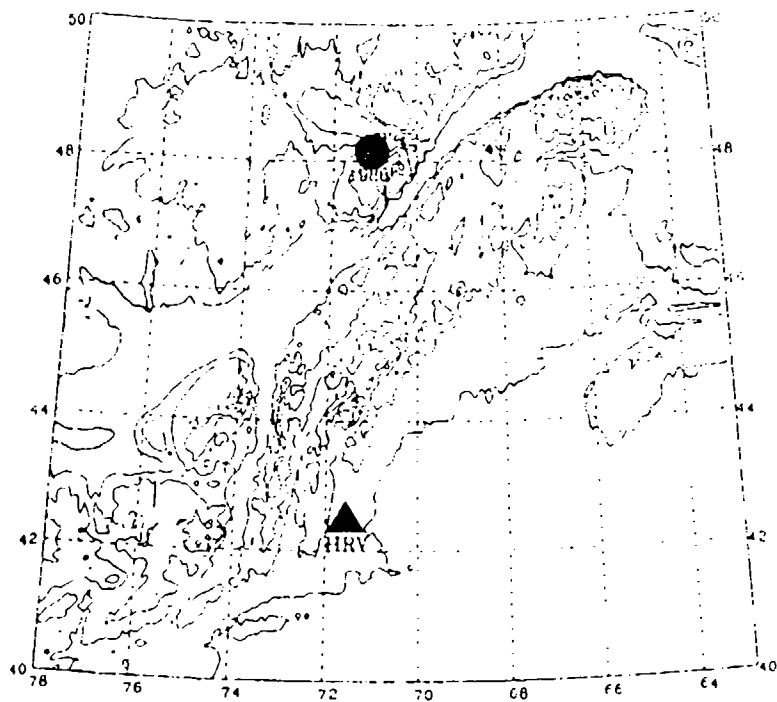


Figure 28. Geographical location of (a) HRV (Harvard) station (solid triangle) and November 25, 1988 Saguenay earthquake (solid star) and (b) GAR (Garm) station (solid triangle) and May 4, 1989 USSR earthquake (solid star).

Broadband Displacement recorded at Harvard
Station from 1988-11-25, Saguenay Earthquake

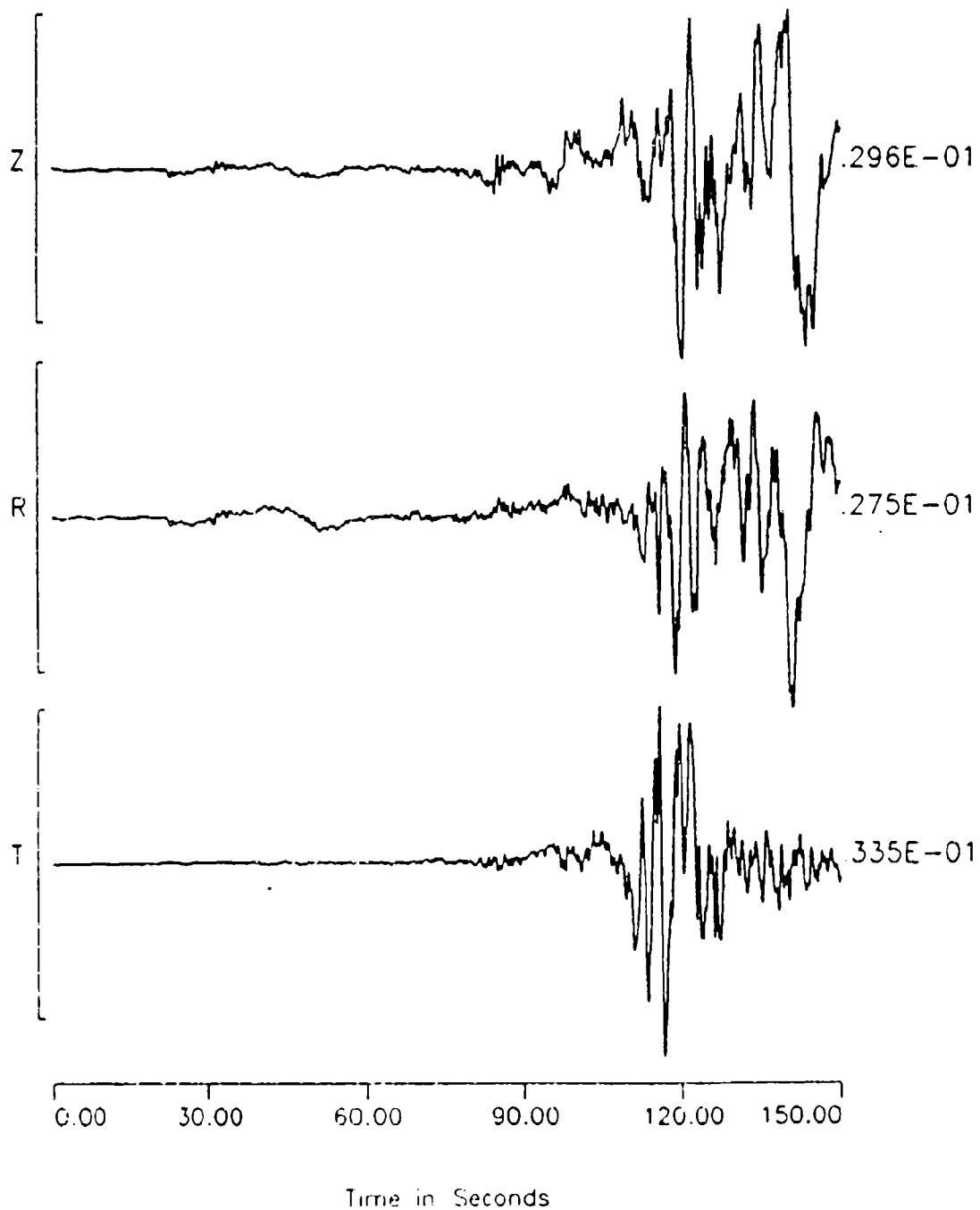


Figure 29. Broadband three-component displacement seismograms as recorded by Harvard station from the 1988, November 25 Saguenay earthquake. The original seismograms were integrated

ENA Regional Velocity Models

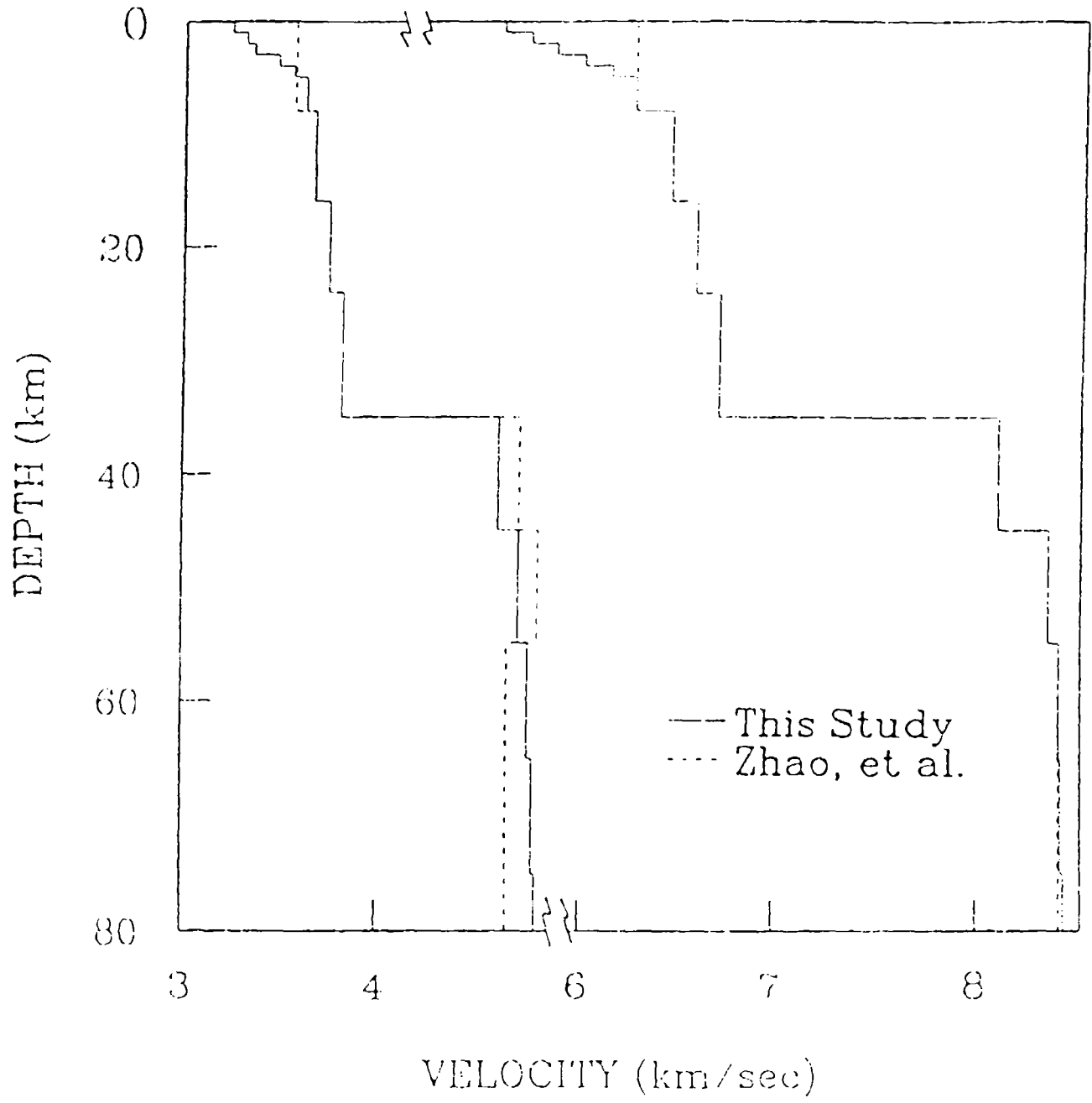


Figure 30. Preliminary regional crustal model developed for the region between the Garm station and the source of the 1989 May 4, USSR earthquake.

(1991) used a reflectivity code (Mallick and Frazer, 1988) to compute the medium response and used an elastic crustal structure to model the data. They used a Q_{β} (shear-wave quality factor) of 6200 and stated that a lower value of Q_{β} is not required to match the recorded wave form, although the conventional wisdom is that for eastern North America Q_{β} is of the order of 300 (Hwang and Mitchell, 1987). Based on this published information, we started to look for certain phases within the P_{nl} regime for which the agreement between the data and synthetic can be improved and in the process to learn more about the regional waveguide.

The phases marked as S_n and sS_n show the greatest misfit between the data and the synthetics computed by Zhao and Helmberger (1991) (see their Figure 16). The synthetic seismograms are definitely of lower frequency. So our initial attempt was to understand what part of the crustal waveguide would be most critical in development of these waveforms. In the present calculation, we used the frequency-wavenumber integration method and set the nyquist frequency at 10 Hz. We computed theoretical seismograms for eight fundamental faults and used a focal mechanism with a dip 65° , a rake of 78° and a strike of 323° to predict the vertical, radial and tangential component seismograms. These synthetics were used to compute both the point and multiple source seismograms and the corresponding vertical component seismograms are shown in Figure 31. The source model contained three sub-sources, with seismic moments of 1.55×10^{24} , 1.45×10^{24} and 1.95×10^{24} dyne-cm respectively. The second source was delayed by 0.65 s and the third source by 1.45 s from the first source to account for the propagation of the rupture front. The first source was represented with a source time function defined by a trapezoid of 0.4s rise time, 0.05s of follow-on time and 0.25s of healing time. Similarly, the second and third sources were convolved with the trapezoids of (0.2s, 0.15s, 0.15s) and (0.1s, 0.3s, 0.2s), respectively. We also show the synthetic seismograms generated by Zhao and Helmberger (1991) in Figure 32 using a nyquist frequency of 4 Hz so that a direct comparison can be made with those shown in Figure 31. The frequency content in the P_{nl} waves of these seismograms is not as rich as those P_{nl} waves shown in Figure 31. In these seismograms (Figure 31), the high frequencies are the result of derived source complexity.

Point-Source Vs Multiple-Source Synthesis of the Harvard Record for Various Crustal Models

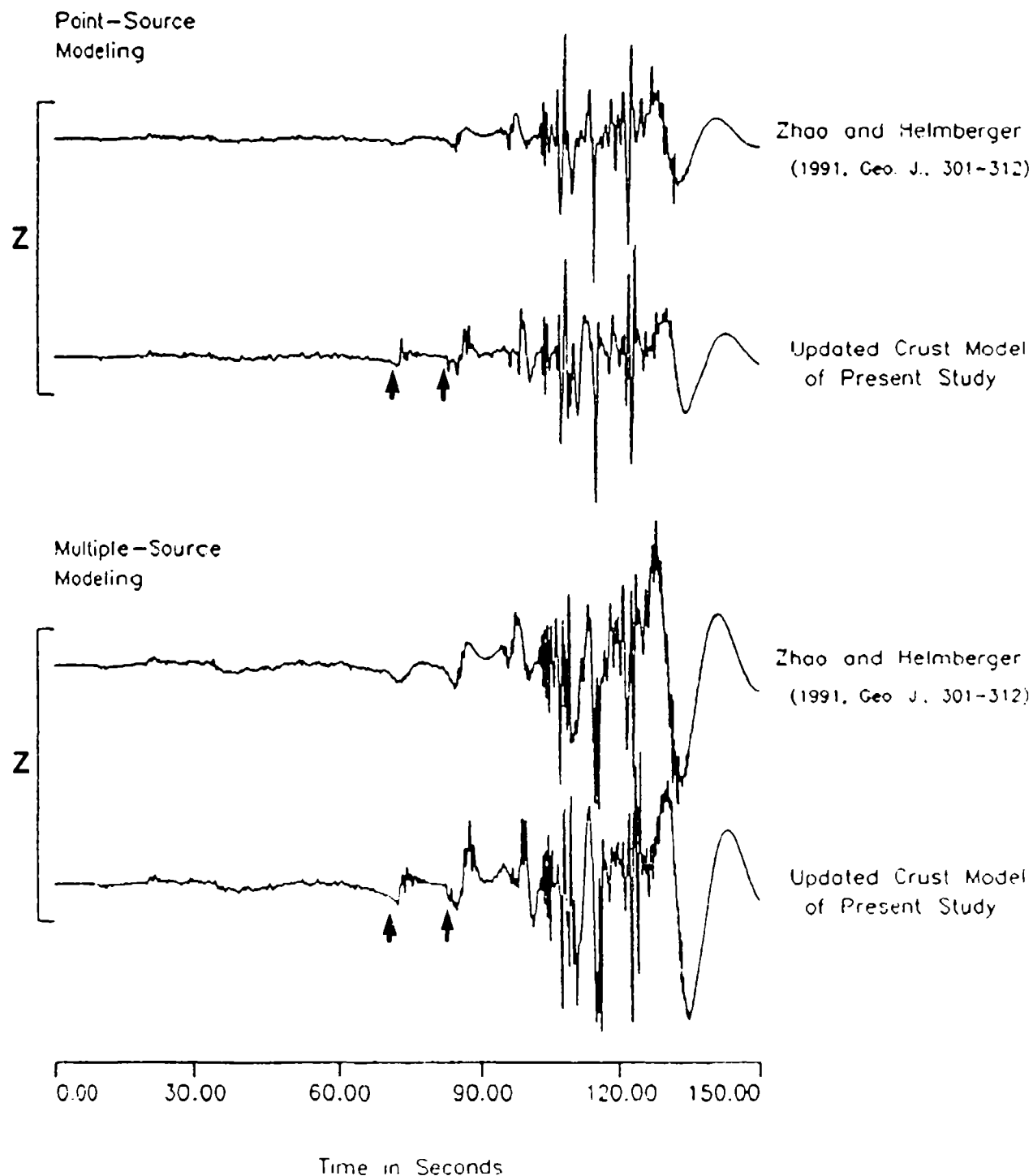


Figure 31. Comparison between two sets of displacement seismograms synthesized using point and multiple sources. (a) Point-source displacements - the upper seismogram is computed using the model response of Zhao and Helmberger (1991) and the bottom seismogram is computed using the model response of the present crustal model, and (b) multiple-source displacements for the two crustal models.

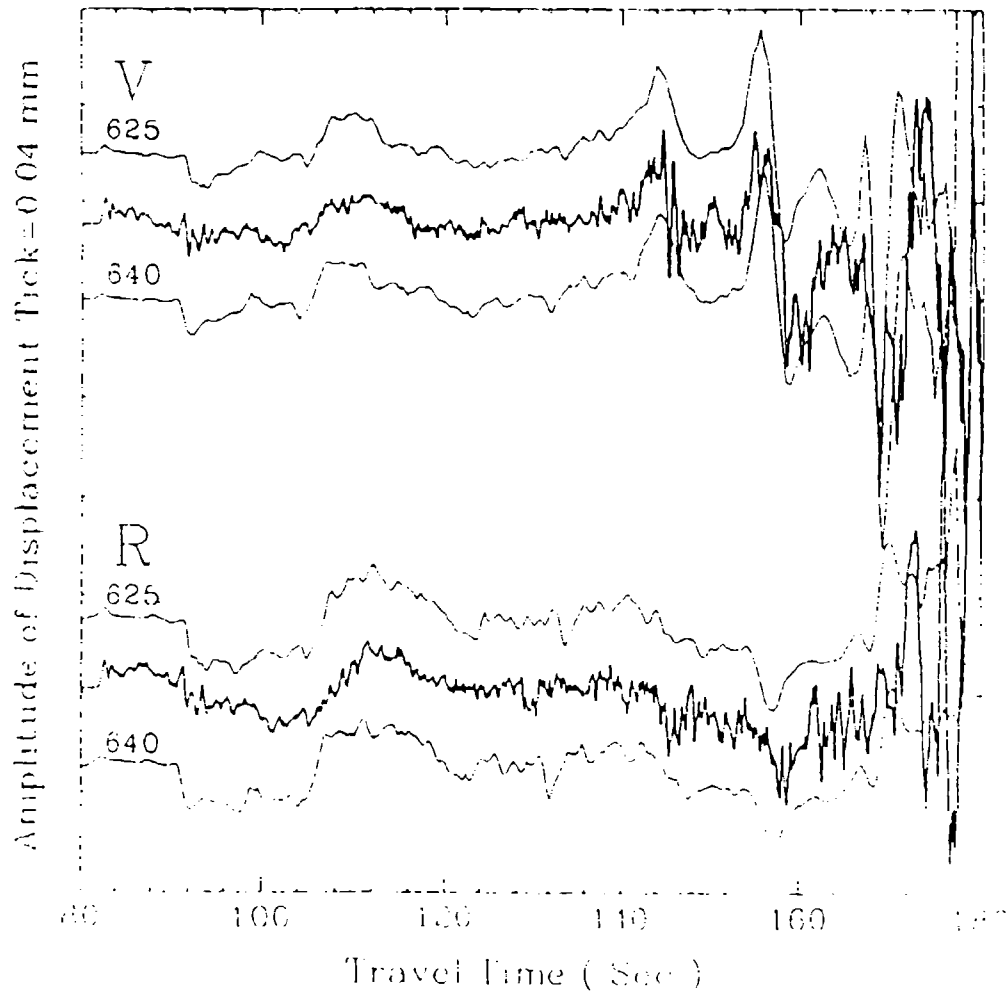


Figure 32. Comparison between data and synthetic displacements with a nyquist of 4 hz. The seismograms for 625 km was computed using a different velocity crustal model (Figure taken from Zhao and Helmberger, 1991)

In Figure 33, we compare the vertical and radial component showing just the P_{nl} portion of the seismograms computed using the parameters of multiple sources. The high-frequency signals are adequately predicted with respect to those observed on the recorded data. The seismograms computed using the response up to 4 Hz were essentially identical to these seismograms.

Ray Analysis of P_{nl} Seismograms. In this section, we discuss our investigation of the constituent phases of the recorded P_{nl} seismogram at Harvard station. The basic idea is to investigate the interaction of individual ray groups in creating the total seismogram. We computed generalized ray seismograms using the source process of the Saguenay earthquake for several groups of generalized rays. In Figure 34, we display vertical-component seismograms of these ray groups. The top six seismograms are normalized to their maximum amplitude. All the PmP and SmS rays were allowed to reflect from each interface beneath the crust-mantle boundary including the reflection from the Moho discontinuity. The total response of these PmP and SmS rays is plotted in the first seismogram. The geometric arrivals are indicated by PmP and SmS respectively. The S_n arrival is small and is preceded by a refracted phase SP . This refracted phase had developed due to a critical incidence of an S wave on an interface permitting the converted P phase to travel along the interface. This is a strong phase as distinctly observed on the record (see Figure 33) and was incorrectly identified by Zhao and Helmberger (1991) as the S_n wave. The seismogram in the second row is for the $sPmP$, a ray which has departed from the source as a S wave and then converted to P mode at the free surface. The amplitude of this ray is small. The next seismogram is for $sSmS$. Both the geometric and head waves are strong for this ray group and contribute significantly to the total seismogram. The next two seismograms are for the $SmSSmS$ and $sSmSSmS$ ray groups. Both the ray groups have significant contributions. The sixth seismogram is for a ray group identified as $SmS'SmS$. The rays included in this group leave the source downward and reflect from each interface. The reflections are turned back into the lower crust again at the Moho discontinuity before they are reflected back to the receiver. The contributions from these rays do offer a significant contribution to the evolution of the S_n wave group. The seismogram "Total" is the result of direct sum of the upper six seismograms. Having obtained a good agreement between

Comparison between Data and Multiple-Source Synthetics

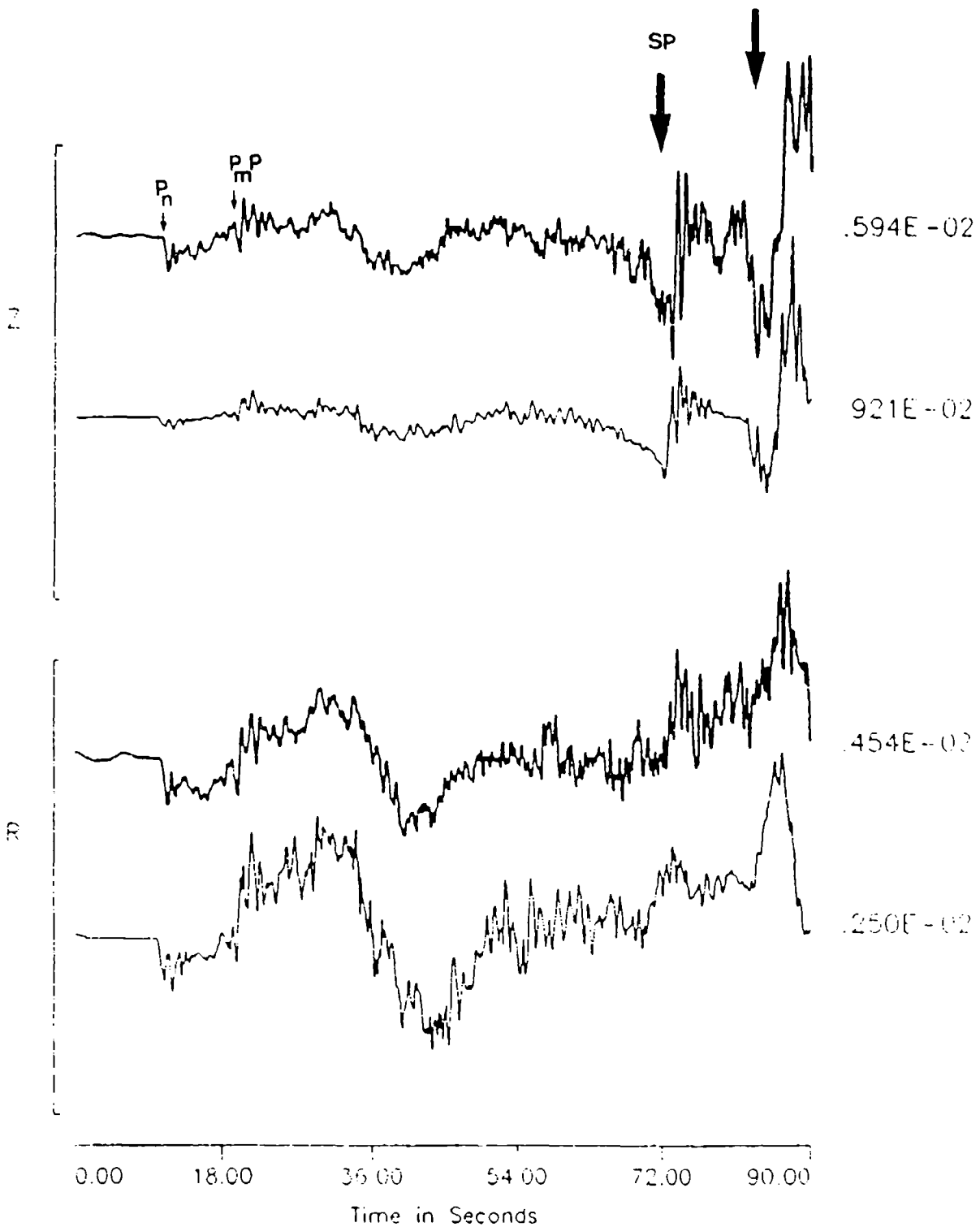


Figure 33. Comparison between data and synthetic displacements computed with model response up to a nyquist of 10 Hz. Note the development of high frequencies and agreement between phases marked by the arrows.

Generalized Ray Interpretation of Pnl Waves at Regional
Distance - $R=640.0$ Km (Saguenay Epicenter to HARVARD)

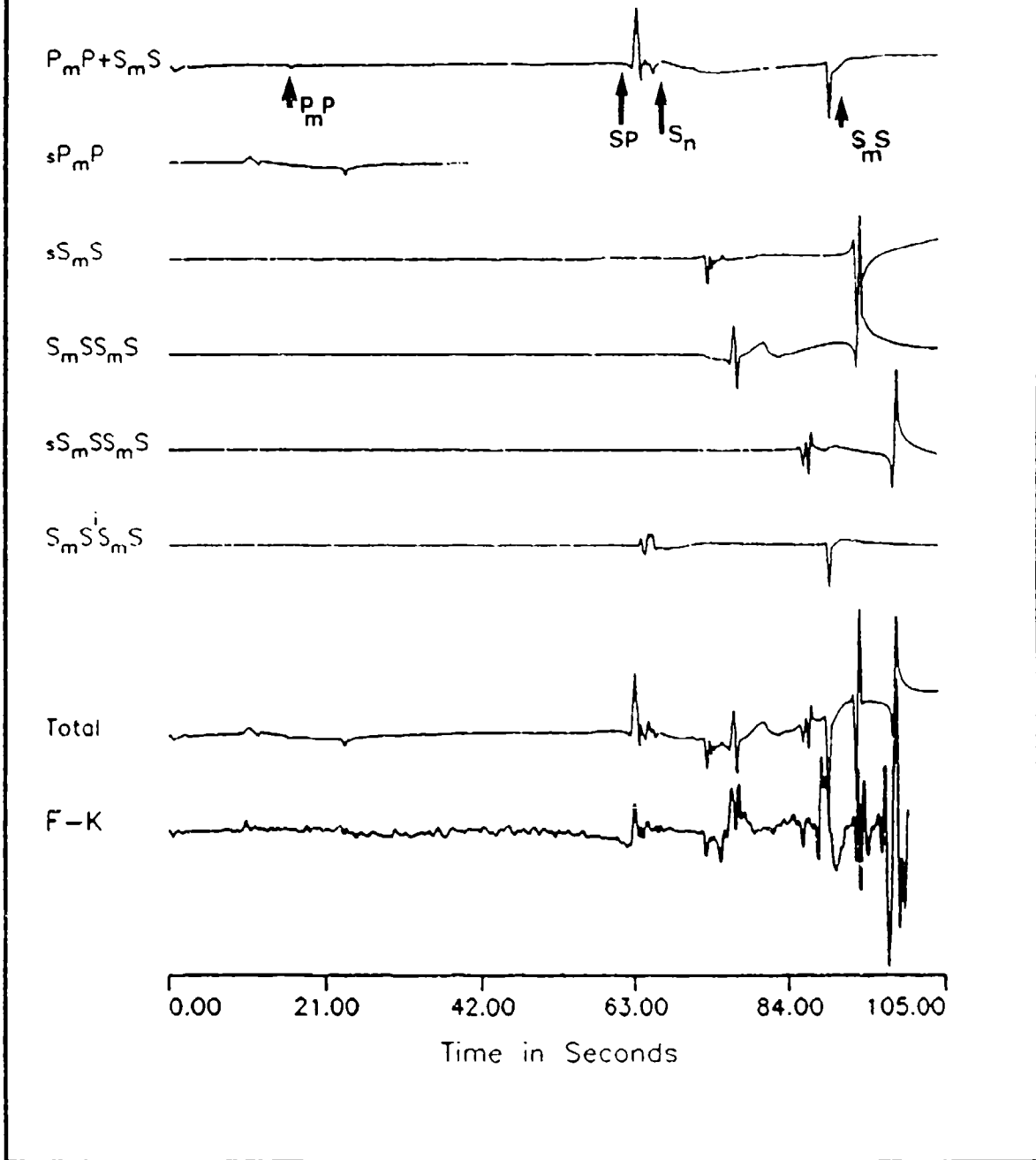


Figure 34. Understanding of the waveform recorded at Harvard station using the ray decomposition technique. The top six seismograms are for the individual ray groups. The seismogram labeled "Total" is the total response of all the responses of upper six seismograms and the comparison with the F-K seismogram shown below suggests a good agreement between the two seismograms.

the data and the synthetics, we only plotted the multiple-source frequency wavenumber seismogram computed using the frequency-wavenumber method beneath the total response for a direct comparison. This comparison produced good agreement among the dominant features within the so called " S_n waves".

Thus, we have extended our previous study (Saikia and Burdick, 1990) on the deciphering of the ray composition of P_g waves from explosion sources to earthquake sources. As in the above study, we found that the waveforms within the S_n group can be studied in time domain in terms of a basic few rays, namely the S_mS , $sSmS$, S_mSSmS , $sSmSSmS$ and $S_mS'SmS$ rays. Since these phases leave the source as S waves, they are not excited by the explosion source. Therefore, the only phases that may arrive within the S_n widow from a pure isotropic source are the P waves that are converted to S waves.

Modeling of GARM Seismograms from May 4, 1989 USSR Earthquake: In this study we have used a set of three-component seismograms recorded at Garm station from an earthquake of May 4, 1989 (latitude: $39.436^\circ N$ and longitude: $75.35^\circ E$, $h=35$ km, ISC). The station is located at a distance of 200 km from the source. Figure 35 shows the recorded displacements processed from the broadband velocity seismograms. A high-pass filter was applied to remove the long-period effects. The crustal structure encountered by the wavefield along its propagation path is complex which is reflected in the waveform. To begin to understand the waveforms, it was necessary to develop a crustal structure.

Our strategy for developing the crustal model was to begin with the tangential component seismogram because of the simplicity of the observed displacement. This component contains only three distinct individual arrivals as marked by the arrows. We used generalized ray theory to synthesize this component for various crustal models and several source depths. The best prediction was obtained for a source depth of 25 km for the preliminary crustal model shown in Figure 36. We used the following focal mechanism, dip= 75° , slip= -135° and a strike= 32° . The structure contains two major discontinuities representing the Conrad and the Moho. We succeeded in modeling the tangential displacement using only three arrivals, the direct SH and two reflections from the

Broadband Displacement recorded at GARM Station
from 1989-05-04 Earthquake in Soviet Union; AZ=292

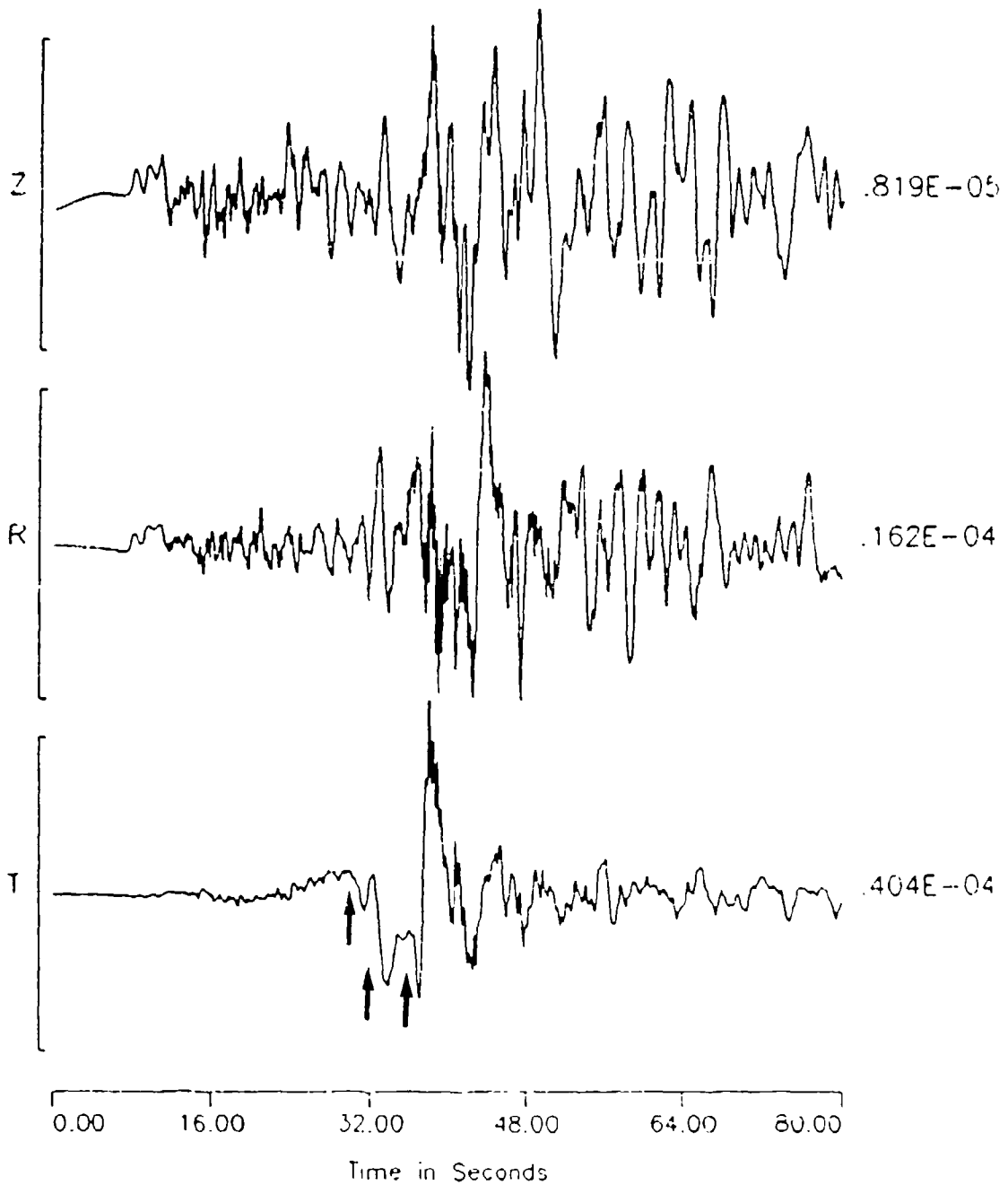


Figure 35. Broadband three-component displacement seismograms as recorded by Garm station from the USSR earthquake of May 4, 1989. The original seismograms were integrated.

USSR Regional Velocity Model

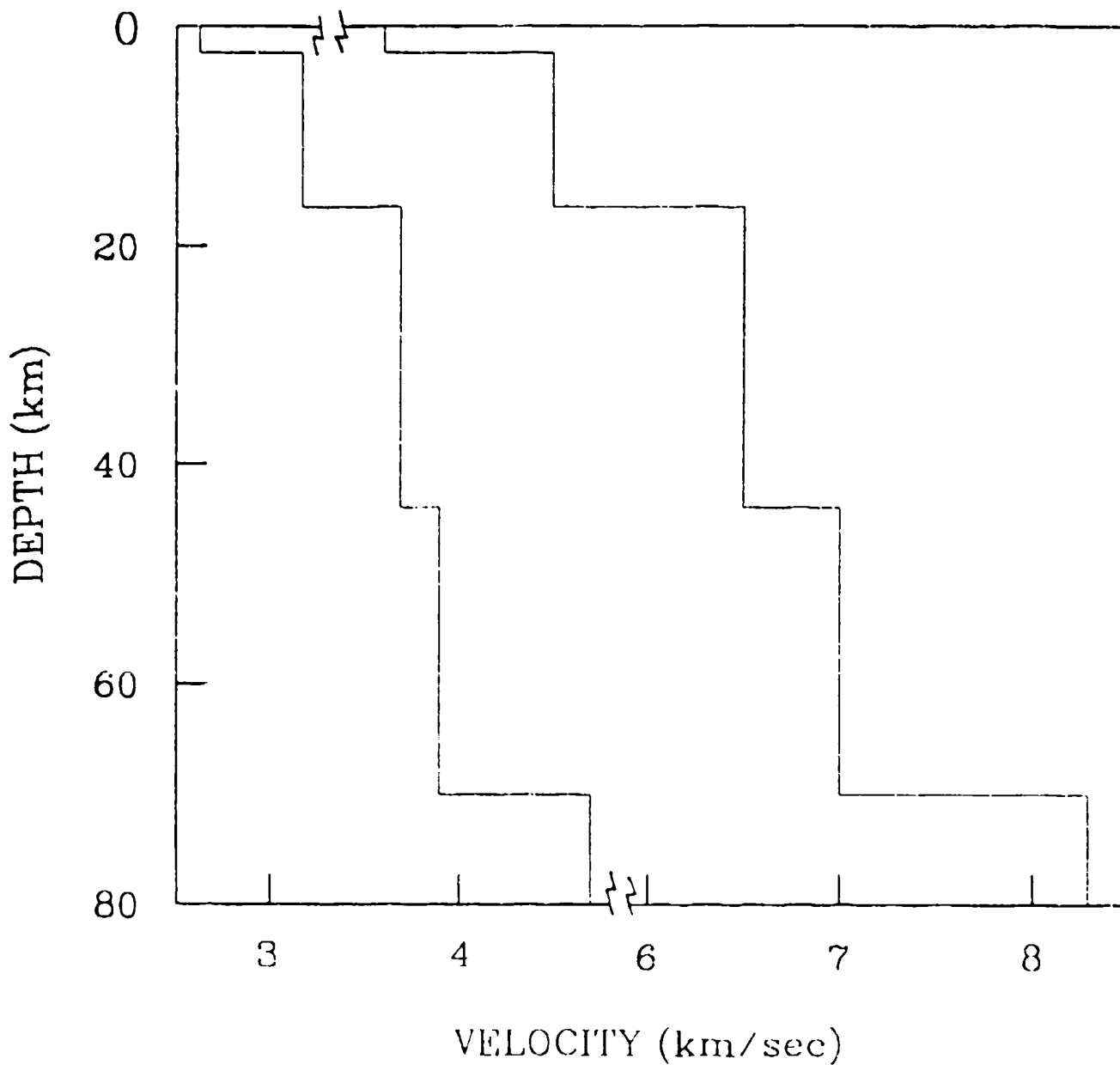


Figure 36. Eastern North American regional velocity profiles. The models shown by the solid lines are developed in this study. The model shown by the dotted lines were published by Zhao and Helmberger (1991).

discontinuities. The frequency-wavenumber seismograms were computed with these parameters and were compared with the recorded data. Figure 37 shows the comparison between the data and the synthetic seismograms for the vertical and tangential components. We are successful in producing a good agreement between the data and the synthetic for the tangential motion. We mark the individual arrivals in the synthetic and show their correspondence with the data by the thin arrows. The vertical component show agreement in the arrivals of P_n , P_mP , ScS and SmS phases. The signal bracketed within the window of the vertical-component synthetic seismogram has a similar character in the frequency content to the signal bracketed within the data window. Figure 38 shows a generalized ray seismogram using the three rays. The vertical synthetic seismogram has a strong SmS which is smeared out in the data due to the interaction with the physically more complicated crust in the region. The vertical component of the recorded seismogram is also dominated by long-period P_{nl} signals shown by the solid window. These waves are also observed in the synthetic seismogram but arriving at Garm with a fast velocity. We also investigated the effect of a possible linear velocity gradient near the free surface to determine if such a velocity distribution would account for the mismatch between the data and the synthetics within the bracketed window shown in Figure 37. We discretized the top ten kilometers of the crust into ten layers of equal thickness and allowed a P-wave velocity increase from 4.5 km/sec to 5.5 km/sec from the surface. The S-wave velocity within each layer had a ratio of 1.73 to the P-wave velocity. This seemed to be a particularly reasonable explanation for the small complex phases between the major arrivals. However, the synthetic seismograms computed using this surface gradient did not improve the fit to a significant degree.

Comparison of Regional P_{nl} Waves from the US and USSR Crustal Models: In this section, we continue to investigate the regional waveforms that are likely to be predicted by the crustal models developed for North America and Soviet Union. Since the record at Harvard station was so successfully modelled and since it was at a range of 640 km, we examined the response of the USSR crust model at this range. In fact, seismograms at such distances are just becoming available from the Soviet Union. Figure 39 shows the comparison between the synthetic seismograms

Preliminary Modeling of Broadband Displacement
 Recorded at GARM station, R=200 Km

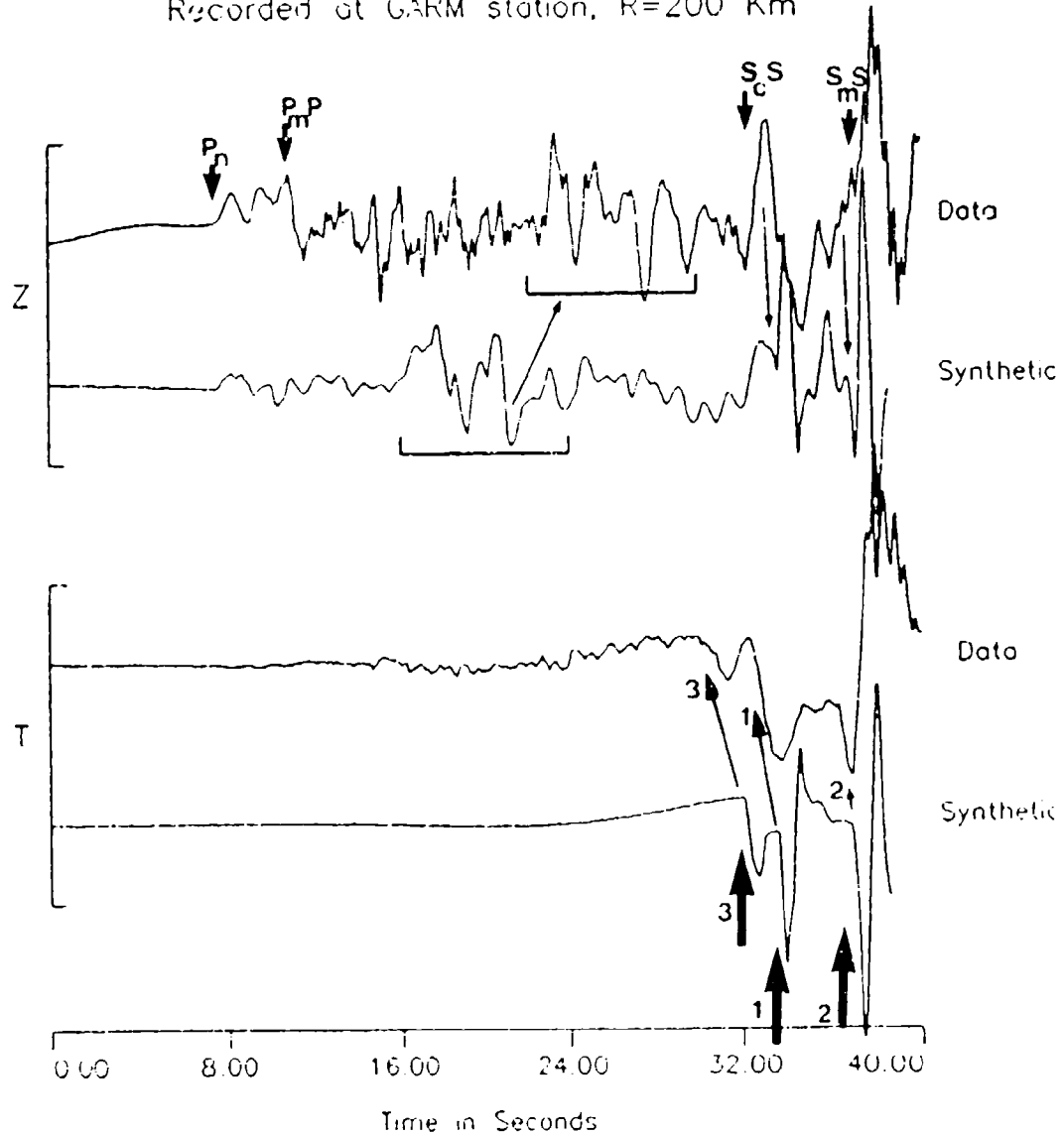


Figure 37. Comparison is shown between the data and the synthetic seismogram for the vertical and tangential components. The signal marked by arrow 1 is a phase reflected from the Conrad and by arrow 2 is from the Moho discontinuity. The phase marked by arrow 3 on the tangential component is the direct arrival. The signal within window shows a possible correlation between the data and synthetics

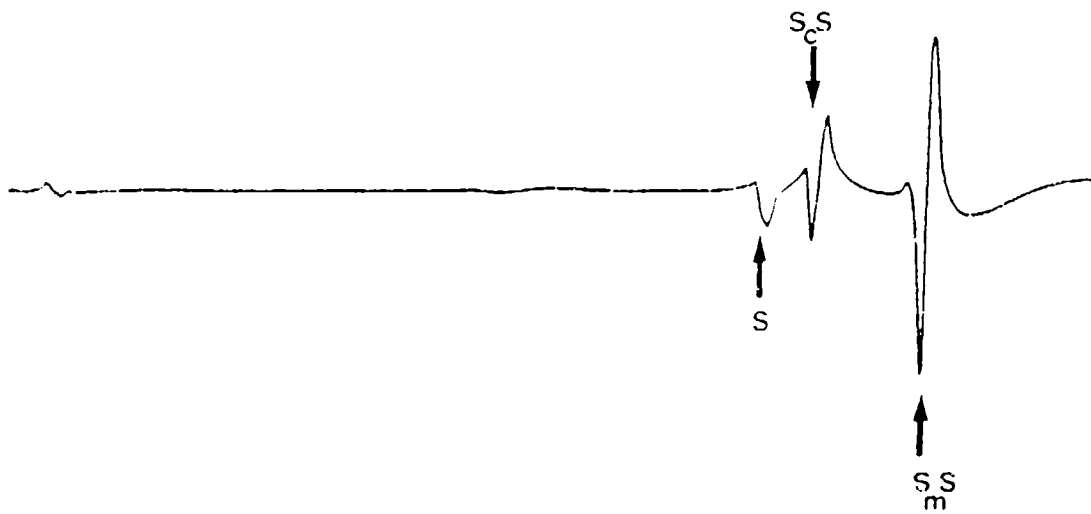


Figure 38. A vertical component seismogram computed using direct P and S, PcP and ScS, and PmP and SmS phases. These arrivals can distinctly be observed on the recorded seismograms.

Comparison of Displacement Seismograms at 640 Km
for the U.S. and USSR Crustal Models

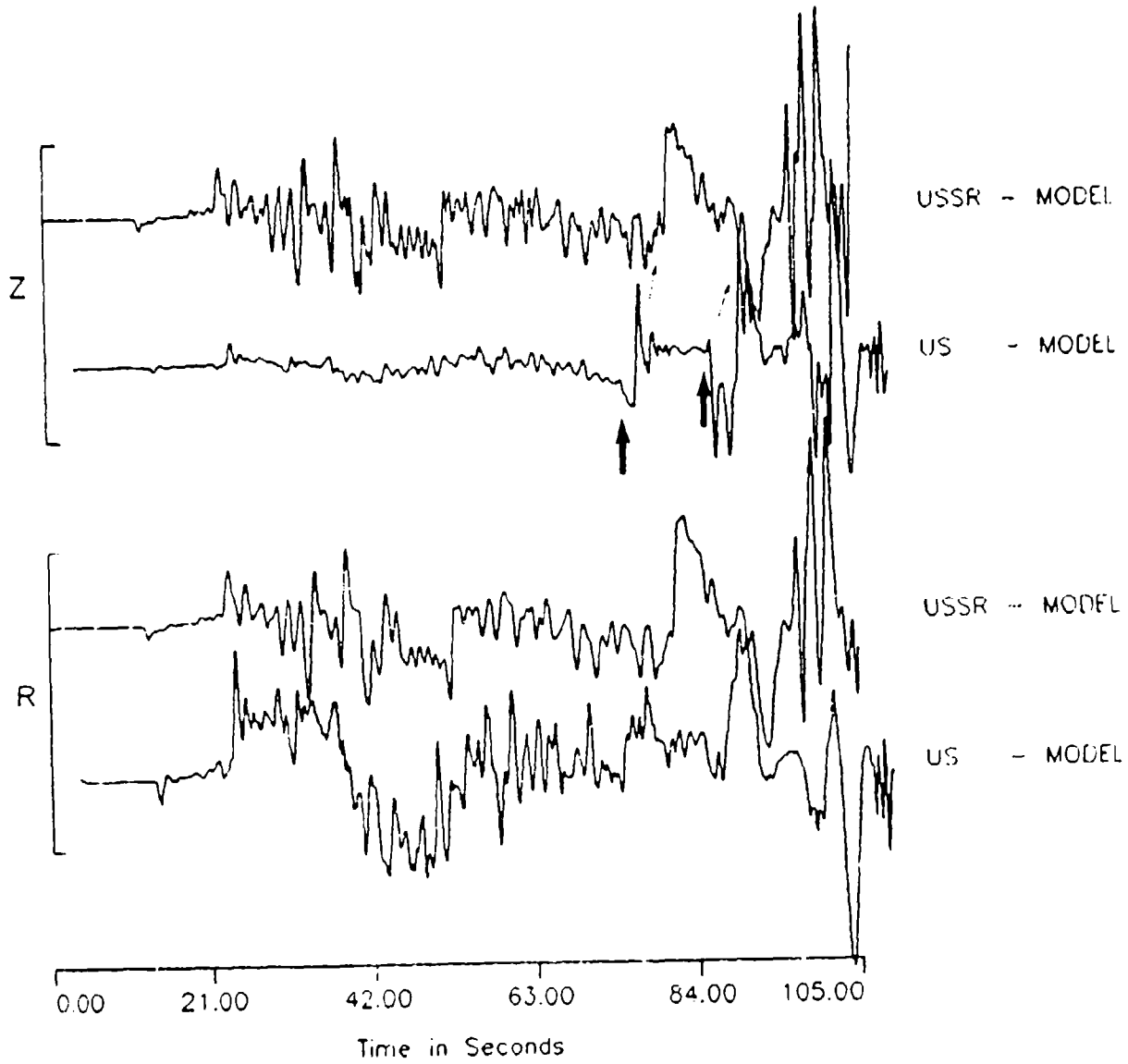


Figure 39. Comparison between the synthetic seismograms computed at 640 km for the USSR crustal model and the US crustal model. Both vertical and radial components are shown.

computed for the USSR and US crustal models for both the vertical and horizontal components assuming the same focal mechanism at the same azimuth. The seismograms are plotted at the respective depths of the earthquakes and the two depths are similar. We also used the same source function. The USSR crustal model predicts a stronger PmP relative to the P_n . The S_n/SP and sS_n arrivals predicted in the seismograms by the US crustal model (marked by the arrows) seem to exhibit a correspondence to the long-period signals predicted in the response of the USSR crustal model. The difference in the amplitude ratios is caused by the differences in the near-surface velocities of the two crustal models. For the North American crustal model, the crustal velocities have a gradient near the surface. The rays arrive at the receiver more steeply compared to the rays for the USSR crustal model, thus partitioning the energy in a significantly different ratio to the vertical and radial component.

We further investigated the composition of the P_{nl} waves predicted by the USSR crustal model at 640 km in terms of generalized rays. We found that the S-wave reflections from the Moho and Conrad discontinuities are strong as shown in the top two seismograms of Figure 40. The Conrad reflection, ScS, arrives immediately following the Moho reflection SmS. The phase shown by an arrow on the SmS seismogram is arriving at the arrival time of S_n phase, but its waveshape is more complicated than is expected from a classical S_n phase. Among the other phases that contribute most significantly to the total P_{nl} seismogram within the S window are the sSmS, SmSSmS and ScSScS phases. The bottom two seismograms plotted in Figure 40 allow us to compare the agreement between the generalized ray (Total) and frequency wavenumber (F-K) seismograms. The agreement is poor following the PmP arrival. A strong long-period signal does propagate to the receiver in the frequency wavenumber seismogram. This must be a total effect of many generalized rays. This effect was also observed on the recorded seismogram at Garm station even at a distance of 200 km from the source.

Conclusions: Based on these investigations, it seems feasible to develop time-domain discriminants at different nuclear test sites which rely on the stable features that are observed in the recorded waveforms. The most stable phases are observed in the explosion generated P_{nl} waveforms for

Generalized Ray Interpretation of Pnl Waves at Regional
 Distance - $R=640.0$ Km - SOVIET UNION CRUSTAL MODEL

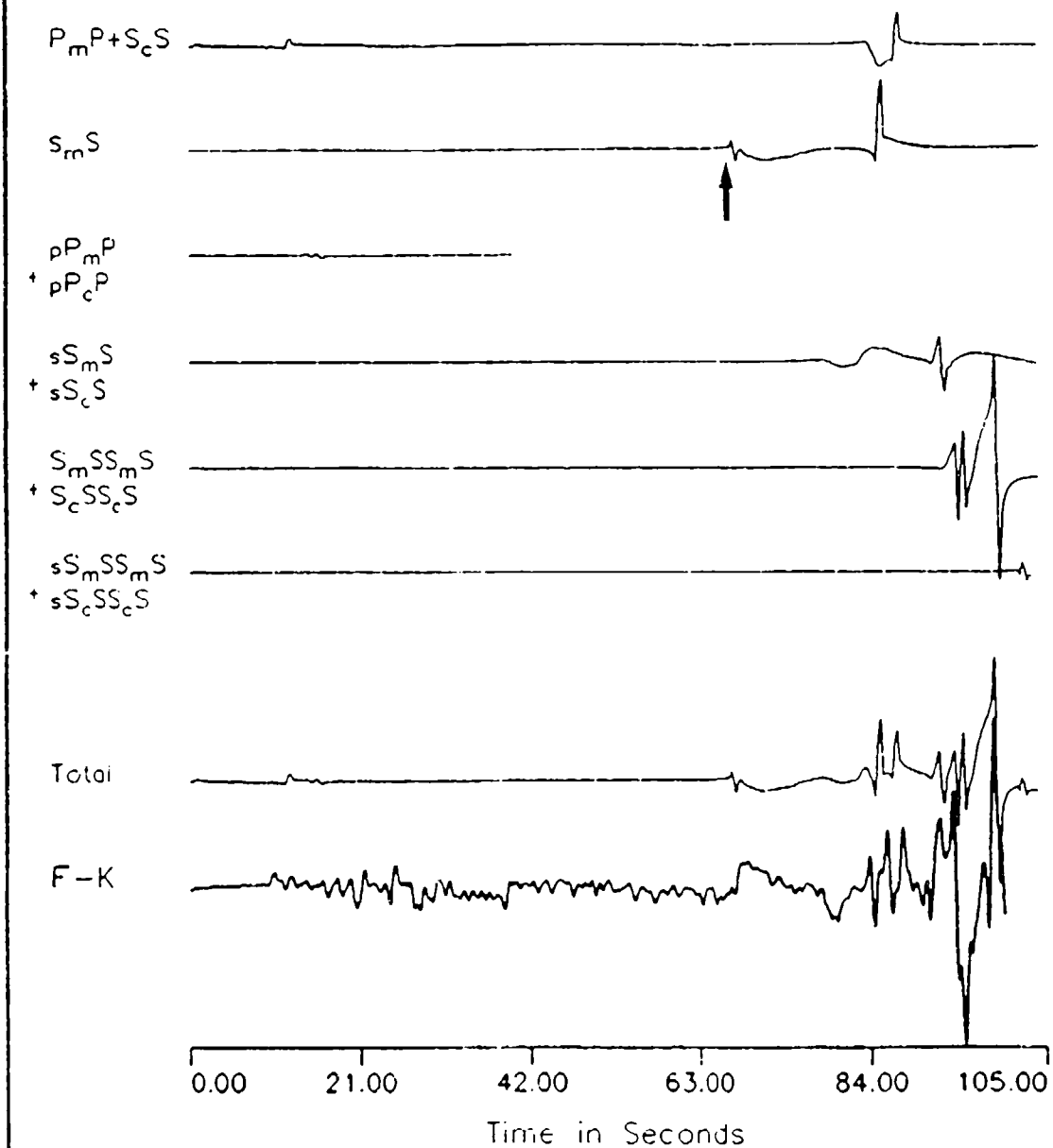


Figure 10. Understanding of the waveform computed at 640 Km from the USSR crustal model using the ray decomposition technique. The top six seismograms are for the individual ray groups.

periods as short as 2 s (Burdick *et al.*, 1988; Saikia and Burdick, 1990). In this study, we have extended our analysis approach to regional broadband seismograms from earthquake sources. The short-period P_{nl} waves have a functional dependence on the crustal waveguide. They can be deterministically modeled using average flat-layered crustal structures and using some selected generalized rays. By modeling the broadband displacement at Harvard station, we found that the structure across the crust-mantle transition zone and within the mantle can profoundly affect the frequency content of the phases like S_n and sS_n . The source multiplicity of an earthquake can also create added complexity in the frequency content of these phases. We found that the P_{nl} seismograms near the S-wave arrival can adequately be modeled using the ray responses of the following phases: SmS, sSmS, SmSSmS, sSmSSmS and SmS'SmS.

For the Soviet Union, the most important requirement for understanding recorded seismograms is the crustal model. The structure within the Soviet Union is heterogeneous and the development of reliable crustal models is on-going (Gurrola and Minster, 1991). In this study, we have developed a crustal structure by modeling the recorded seismograms at Garm station from an earthquake at a distance of 200 km ($Az=292^\circ$) which consisted of Conrad and Moho discontinuities. In addition, a slight gradient is allowed for the upper-mantle structure. The ray analysis indicated that the most important generalized rays for the composition of the P_{nl} waves are the following phases: SmS, ScS, sSmS, sScS, SmSSmS and sSmSSmS.

REFERENCES

- Barker, J.S., "Analysis of regional bodywave phases from earthquakes and explosions in eastern Asia", PL/DARPA Seismic Research Symposium, 64-70, PL-TR-91-2208, ADA241325, 1991.
- Bennett, T. J., B. W. Barker, K. L. McLaughlin, and J. R. Murphy, "Regional discrimination of quarry blasts, earthquakes and underground nuclear explosions", ADA223148, Final Report, 1989.
- Blandford, R. R., "Seismic discrimination problems at regional distances", in Identification of Seismic Sources, E. S. Husebye and S. Mykkelveit eds., D. Reidel Publishing Co., Dordrecht, The Netherlands, 695-740, 1981.
- Brune, J. N., "Tectonic stress and spectra of seismic shear waves from earthquakes", J. Geophys. Res., 75, 4997-5009, 1970.
- Burdick, L. J. and D. V. Helmberger, "The upper mantle P velocity structure of the western United States", J. Geophys. Res., 83, 1699-1712, 1978.
- Burdick, L. J., C. K. Saikia, E.J. Garnero, D. V. Helmberger, and L.S. Zhao, "Regional and upper mantle wave propagation in the Soviet Union", PL/DARPA Seismic Research Symposium, 100-107, PL-TR-91-2208, ADA241325, 1991.
- Burdick, L. J., C. K. Saikia and D. V. Helmberger, "Deterministic modeling of regional waveforms from the Nevada test site", ADA216641, Final Report, 1989.
- Burdick, L. J., C. K. Saikia, and N. F. Smith, "Pn from the Nevada test site", AFGL Tech. Rep., TR-89-0034, Rep 3, Air Force Geophysical Lab., Bedford, Mass, ADA208276, 1988.
- Burdick, L. J., T. C. Wallace and T. Lay, "Modeling the near field and teleseismic observations from the Amchitka test site", J. Geophys. Res., 89, 4373-4388, 1984.
- Dowla, F. U., S. R. Taylor and R. W. Anderson, "Seismic detection with artificial neural networks: Preliminary results with regional spectral data", Bull. Seism. Soc. Am., (to be submitted), 1990.
- Given, H. K., D. V. Helmberger, and L. S. Zhao, "A new acquisition of historical seismograms from the USSR emphasizing digital storage", EOS, Transactions, 72, 190, 1991.

- Given, J. W. and D. V. Helmberger, "Upper mantle structure of northwestern Eurasia", J. Geophys. Res., 85, 7183-7194, 1980.
- Gurrola, H. and J. B. Minster, "Single-station estimates of crust and upper mantle velocity structure at broadband IRIS/IDA stations in the USSR", PL/DARPA Seismic Research Symposium, 225-236, PL-TR-91-2208, ADA241325, 1991.
- Helmberger, D. V., "Long period body-wave propagation from 4° to 13°", Bull. Seis. Soc. Am., 62, 325-341, 1972.
- Helmberger, D. V., "Numerical seismograms of long-period body waves from seventeen to forty degrees", Bull. Seism. Soc. Am., 63, 633-646, 1973a.
- Helmberger, D. V., "On the structure of the low velocity zone", Geophys. J. R. Astr. Soc., 34, 251-263, 1973b.
- Helmberger D.V., D. Dreger, L.S. Zhao, S. Kedar, B. Woods, and D.G. Harkrider, "Source retrieval from regional seismograms", PL/DARPA Seismic Research Symposium, 249-260, PL-TR-91-2208, ADA241325, 1991.
- Hwang, H-J., and B. J. Mitchell, "Shear velocities, Q_w , and the frequency dependent of the Q_p in stable and tectonically active regions from surface wave observation", Geophys. J. R. Astr. Soc., 90, 575-613, 1987.
- Jones, L. E. and D. V. Helmberger, "Possible nature of the 520 Discontinuity", EOS, Transactions, 72, 200, 1991.
- King, D. W. and G. Calcagnile, "P wave velocities in the upper mantle beneath Fennoscandia and western Russia", Geophys. J. R. Astron. Soc., 46, 407-432, 1976.
- Lay, T., L. J. Burdick and D. V. Helmberger, "Estimating the yields of the Amchitka tests by waveform intercorrelation", Geophys. J. R. A. S., 78, 181-208, 1984.
- LeFevre, L. V. and D. V. Helmberger, "Upper mantle P velocity structure of the Canadian shield", J. Geophys. Res., 91, 17749-17765, 1989.

- Mallick, S., and L.N. Frazer, "Rapid computation of multioffset vertical seismic profile synthetic seismograms for layered media", Geophysics, 53, 479-491, 1988.
- Murphy, J. R., "Network averaged teleseismic P wave spectra for underground explosions part II. Source characteristics of Pahute Mesa explosions", Bull. Seism. Soc. Am., (submitted), 1988.
- Murphy, J. R. and T. J. Bennett, "A discrimination analysis of short period regional seismic data recorded at Tonto Forest Observatory", Bull. Seism. Soc. Am., 72, 1351-1366, 1982.
- Saikia, C. K. and L. J. Burdick, "Fine structure of Pnl waves from explosions", J. Geophys. Res., V 96, 14,383-14,401, 1990.
- Savage, J. C., "Radiation from a realistic model of faulting", Bull. Seism. Soc. Am., 56, 577-593, 1966.
- Somerville, P. G., J. P. McLaren, L. V. LeFevre, R. W. Burger and D. V. Helmberger, "Comparison of source scaling relations of eastern and western North American earthquakes", Bull. Seism. Soc. Am., 77, 322-346, 1987.
- Taylor, S. R., N. W. Sherman and M. D. Denny, "Spectral discrimination between NTS explosions and western United States earthquakes at regional distances", Bull. Seism. Soc. Am., 78, 1563-1579, 1988.
- Zhao, L. S., and D. V. Helmberger, "Broadband modeling along a regional shield path, Harvard recording of the Saguenay earthquake", Geophys. J. Int., 105, 301-312, 1991.

Prof. Thomas Ahrens
Seismological Lab, 252-21
Division of Geological & Planetary Sciences
California Institute of Technology
Pasadena, CA 91125

Prof. Keiiti Aki
Center for Earth Sciences
University of Southern California
University Park
Los Angeles, CA 90089-0741

Prof. Shelton Alexander
Geosciences Department
403 Deike Building
The Pennsylvania State University
University Park, PA 16802

Dr. Ralph Alewine, III
DARPA/NMRO
3701 North Fairfax Drive
Arlington, VA 22203-1714

Prof. Charles B. Archambeau
CIRES
University of Colorado
Boulder, CO 80309

Dr. Thomas C. Bache, Jr.
Science Applications Int'l Corp.
10260 Campus Point Drive
San Diego, CA 92121 (2 copies)

Prof. Muawia Barazangi
Institute for the Study of the Continent
Cornell University
Ithaca, NY 14853

Dr. Jeff Barker
Department of Geological Sciences
State University of New York
at Binghamton
Vestal, NY 13901

Dr. Douglas R. Baumgardt
ENSCO, Inc
5400 Port Royal Road
Springfield, VA 22151-2388

Dr. Susan Beck
Department of Geosciences
Building #77
University of Arizona
Tucson, AZ 85721

Dr. T.J. Bennett
S-CUBED
A Division of Maxwell Laboratories
11800 Sunrise Valley Drive, Suite 1212
Reston, VA 22091

Dr. Robert Blandford
AFTAC/TT, Center for Seismic Studies
1300 North 17th Street
Suite 1450
Arlington, VA 22209-2308

Dr. G.A. Bollinger
Department of Geological Sciences
Virginia Polytechnical Institute
21044 Derring Hall
Blacksburg, VA 24061

Dr. Stephen Bratt
Center for Seismic Studies
1300 North 17th Street
Suite 1450
Arlington, VA 22209-2308

Dr. Lawrence Burdick
Woodward-Clyde Consultants
566 El Dorado Street
Pasadena, CA 91109-3245

Dr. Robert Burrige
Schlumberger-Doll Research Center
Old Quarry Road
Ridgefield, CT 06877

Dr. Jerry Carter
Center for Seismic Studies
1300 North 17th Street
Suite 1450
Arlington, VA 22209-2308

Dr. Eric Chael
Division 9241
Sandia Laboratory
Albuquerque, NM 87185

Prof. Vernon F. Cormier
Department of Geology & Geophysics
U-45, Room 207
University of Connecticut
Storrs, CT 06268

Prof. Steven Day
Department of Geological Sciences
San Diego State University
San Diego, CA 92182

Marvin Denny
U.S. Department of Energy
Office of Arms Control
Washington, DC 20585

Dr. Zoltan Der
ENSCO, Inc.
5400 Port Royal Road
Springfield, VA 22151-2388

Prof. Adam Dziewonski
Hoffman Laboratory, Harvard University
Dept. of Earth Atmos. & Planetary Sciences
20 Oxford Street
Cambridge, MA 02138

Prof. John Ebel
Department of Geology & Geophysics
Boston College
Chestnut Hill, MA 02167

Eric Fielding
SNEE Hall
INSTOC
Cornell University
Ithaca, NY 14853

Dr. Mark D. Fisk
Mission Research Corporation
735 State Street
P.O. Drawer 719
Santa Barbara, CA 93102

Prof Stanley Flatte
Applied Sciences Building
University of California, Santa Cruz
Santa Cruz, CA 95064

Dr. John Foley
NER-Geo Sciences
1100 Crown Colony Drive
Quincy, MA 02169

Prof. Donald Forsyth
Department of Geological Sciences
Brown University
Providence, RI 02912

Dr. Art Frankel
U.S. Geological Survey
922 National Center
Reston, VA 22092

Dr. Cliff Frolich
Institute of Geophysics
8701 North Mopac
Austin, TX 78759

Dr. Holly Given
IGPP, A-025
Scripps Institute of Oceanography
University of California, San Diego
La Jolla, CA 92093

Dr. Jeffrey W. Given
SAIC
10260 Campus Point Drive
San Diego, CA 92121

Dr. Dale Glover
Defense Intelligence Agency
ATTN: ODT-1B
Washington, DC 20301

Dr. Indra Gupta
Teledyne Geotech
314 Montgomery Street
Alexandria, VA 22314

Dan N. Hagedorn
Pacific Northwest Laboratories
Battelle Boulevard
Richland, WA 99352

Dr. James Hannon
Lawrence Livermore National Laboratory
P.O. Box 808
L-205
Livermore, CA 94550

Dr. Roger Hansen
HQ AFTAC/TTR
Patrick AFB, FL 32925-6001

Prof. David G. Harkrider
Seismological Laboratory
Division of Geological & Planetary Sciences
California Institute of Technology
Pasadena, CA 91125

Prof. Danny Harvey
CIRES
University of Colorado
Boulder, CO 80309

Prof. Donald A. Helmberger
Seismological Laboratory
Division of Geological & Planetary Sciences
California Institute of Technology
Pasadena, CA 91125

Prof. Eugene Herrin
Institute for the Study of Earth and Man
Geophysical Laboratory
Southern Methodist University
Dallas, TX 75275

Prof. Robert B. Herrmann
Department of Earth & Atmospheric Sciences
St. Louis University
St. Louis, MO 63156

Prof. Lane R. Johnson
Seismographic Station
University of California
Berkeley, CA 94720

Prof. Thomas H. Jordan
Department of Earth, Atmospheric &
Planetary Sciences
Massachusetts Institute of Technology
Cambridge, MA 02139

Prof. Alan Kafka
Department of Geology & Geophysics
Boston College
Chestnut Hill, MA 02167

Robert C. Kemerait
ENSCO, Inc.
445 Pineda Court
Melbourne, FL 32940

Dr. Max Koontz
U.S. Dept. of Energy/DP 5
Forrestal Building
1000 Independence Avenue
Washington, DC 20585

Dr. Richard LaCoss
MIT Lincoln Laboratory, M-200B
P.O. Box 73
Lexington, MA 02173-0073

Dr. Fred K. Lamb
University of Illinois at Urbana-Champaign
Department of Physics
1110 West Green Street
Urbana, IL 61801

Prof. Charles A. Langston
Geosciences Department
403 Deike Building
The Pennsylvania State University
University Park, PA 16802

Jim Lawson, Chief Geophysicist
Oklahoma Geological Survey
Oklahoma Geophysical Observatory
P.O. Box 8
Leonard, OK 74043-0008

Prof. Thome Lay
Institute of Tectonics
Earth Science Board
University of California, Santa Cruz
Santa Cruz, CA 95064

Dr. William Leith
U.S. Geological Survey
Mail Stop 928
Reston, VA 22092

Mr. James F. Lewkowicz
Phillips Laboratory/GPEH
Hanscom AFB, MA 01731-5000 (2 copies)

Mr. Alfred Lieberman
ACDA/VI-OA State Department Building
Room 5726
320-21st Street, NW
Washington, DC 20451

Prof. L. Timothy Long
School of Geophysical Sciences
Georgia Institute of Technology
Atlanta, GA 30332

Dr. Randolph Martin, III
New England Research, Inc.
76 Olcott Drive
White River Junction, VT 05001

Dr. Robert Masse
Denver Federal Building
Box 25046, Mail Stop 967
Denver, CO 80225

Dr. Gary McCarror
Department of Physics
Southern Methodist University
Dallas, TX 75275

Prof. Thomas V. McEvelly
Seismographic Station
University of California
Berkeley, CA 94720

Dr. Art McGarr
U.S. Geological Survey
Mail Stop 977
U.S. Geological Survey
Menlo Park, CA 94025

Dr. Keith L. McLaughlin
S-CUBED
A Division of Maxwell Laboratory
P.O. Box 1620
La Jolla, CA 92038-1620

Stephen Miller & Dr. Alexander Florence
SRI International
333 Ravenswood Avenue
Box AF 116
Menlo Park, CA 94025-3493

Prof. Bernard Minster
IGPP, A-025
Scripps Institute of Oceanography
University of California, San Diego
La Jolla, CA 92093

Prof. Brian J. Mitchell
Department of Earth & Atmospheric Sciences
St. Louis University
St. Louis, MO 63156

Mr. Jack Murphy
S-CUBED
A Division of Maxwell Laboratory
11800 Sunrise Valley Drive, Suite 1212
Reston, VA 22091 (2 Copies)

Dr. Keith K. Nakanishi
Lawrence Livermore National Laboratory
L-025
P.O. Box 808
Livermore, CA 94550

Dr. Carl Newton
Los Alamos National Laboratory
P.O. Box 1663
Mail Stop C335, Group ESS-3
Los Alamos, NM 87545

Dr. Bao Nguyen
HQ AFTAC/TTR
Patrick AFB, FL 32925-6001

Prof. John A. Orcutt
IGPP, A-025
Scripps Institute of Oceanography
University of California, San Diego
La Jolla, CA 92093

Prof. Jeffrey Park
Kline Geology Laboratory
P.O. Box 6666
New Haven, CT 06511-8130

Dr. Howard Patton
Lawrence Livermore National Laboratory
L-025
P.O. Box 808
Livermore, CA 94550

Dr. Frank Pilote
HQ AFTAC/TT
Patrick AFB, FL 32925-6001

Dr. Jay J. Pulli
Radix Systems, Inc.
2 Taft Court, Suite 203
Rockville, MD 20850

Dr. Robert Reinke
ATTN: FCTVTD
Field Command
Defense Nuclear Agency
Kirland AFB, NM 87115

Prof. Paul G. Richards
Lamont-Doherty Geological Observatory
of Columbia University
Palisades, NY 10964

Mr. Wilmer Rivers
Teledyne Geotech
314 Montgomery Street
Alexandria, VA 22314

Dr. George Rothe
HQ AFTAC/TTR
Patrick AFB, FL 32925-6001

Dr. Alan S. Ryall, Jr.
DARPA/NMRO
3701 North Fairfax Drive
Arlington, VA 22209-1714

Dr. Richard Sailor
TASC, Inc.
55 Walker Brook Drive
Reading, MA 01867

Dr. Charles G. Sammis
Center for Earth Sciences
University of Southern California
University Park
Los Angeles, CA 90089-0741

Prof. Christopher H. Scholz
Lamont-Doherty Geological Observatory
of Columbia University
Palisades, CA 10964

Dr. Susan Schwartz
Institute of Tectonics
1156 High Street
Santa Cruz, CA 95064

Secretary of the Air Force
(SAFRD)
Washington, DC 20330

Office of the Secretary of Defense
DDR&E
Washington, DC 20330

Thomas J. Sereno, Jr.
Science Application Intl Corp.
10260 Campus Point Drive
San Diego, CA 92121

Dr. Michael Shore
Defense Nuclear Agency/SPSS
6801 Telegraph Road
Alexandria, VA 22310

Dr. Matthew Sibol
Virginia Tech
Seismological Observatory
3044 Derring Hall
Blacksburg, VA 24061-0420

Prof. David G. Simpson
ERIS, Inc.
1616 North Fort Myer Drive
Suite 1440
Arlington, VA 22209

Donald L. Springer
Lawrence Livermore National Laboratory
L-025
P.O. Box 808
Livermore, CA 94550

Dr. Jeffrey Stevens
S-CUBED
A Division of Maxwell Laboratory
P.O. Box 1620
La Jolla, CA 92038-1620

Lt. Col. Jim Stobie
ATTN: AFOSR/NL
Bolling AFB
Washington, DC 20332-6448

Prof. Brian Stump
Institute for the Study of Earth & Man
Geophysical Laboratory
Southern Methodist University
Dallas, TX 75275

Prof. Jeremiah Sullivan
University of Illinois at Urbana-Champaign
Department of Physics
1110 West Green Street
Urbana, IL 61801

Prof. L. Sykes
Lamont-Doherty Geological Observatory
of Columbia University
Palisades, NY 10964

Dr. David Taylor
ENSCO, Inc
445 Pineda Court
Melbourne, FL 32940

Dr. Steven R. Taylor
Los Alamos National Laboratory
P.O. Box 1663
Mail Stop C335
Los Alamos, NM 87545

Prof. Clifford Thurber
University of Wisconsin-Madison
Department of Geology & Geophysics
1215 West Dayton Street
Madison, WI 53706

Prof. M. Nafi Toksoz
Earth Resource Lab
Massachusetts Institute of Technology
42 Carleton Street
Cambridge, MA 02142

Dr. Larry Turnbull
CIA-OSWR/NEED
Washington, DC 20505

DARPA/RMO/SECURITY OFFICE
3701 North Fairfax Drive
Arlington, VA 22203-1714

Dr. Gregory van der Vink
IRIS, Inc.
1616 North Fort Myer Drive
Suite 1440
Arlington, VA 22209

HQ DNA
ATTN: Technical Library
Washington, DC 20305

Dr. Karl Veith
EG&G
5211 Auth Road
Suite 240
Suitland, MD 20746

Defense Intelligence Agency
Directorate for Scientific & Technical Intelligence
ATTN: DTIB
Washington, DC 20340-6158

Prof. Terry C. Wallace
Department of Geosciences
Building #77
University of Arizona
Tucson, AZ 85721

Defense Technical Information Center
Cameron Station
Alexandria, VA 22314 (2 Copies)

Dr. Thomas Weaver
Los Alamos National Laboratory
P.O. Box 1663
Mail Stop C335
Los Alamos, NM 87545

TACTEC
Battelle Memorial Institute
505 King Avenue
Columbus, OH 43201 (Final Report)

Dr. William Wortman
Mission Research Corporation
8560 Cinderbed Road
Suite 700
Newington, VA 22122

Phillips Laboratory
ATTN: XPG
Hanscom AFB, MA 01731-5000

Prof. Francis T. Wu
Department of Geological Sciences
State University of New York
at Binghamton
Vestal, NY 13901

Phillips Laboratory
ATTN: GPE
Hanscom AFB, MA 01731-5000

AFIAC/CA
(STINFO)
Patrick AFB, FL 32925-6000

Phillips Laboratory
ATTN: TSML
Hanscom AFB, MA 01731-5000

DARPA/PPI
3701 North Fairfax Drive
Arlington, VA 22203-1714

Phillips Laboratory
ATTN: SUL
Kirtland, NM 87117 (2 copies)

DARPA/RMO/RETRIEVAL
3701 North Fairfax Drive
Arlington, VA 22203-1714

Dr. Michel Bouchon
I.R.I.G.M.-B.P. 68
38402 St. Martin D'Heres
Cedex, FRANCE

Dr. Michel Campillo
Observatoire de Grenoble
I.R.I.G.M. B.P. 53
38041 Grenoble, FRANCE

Dr. Jorg Schlittenhardt
Federal Institute for Geosciences & Nat'l Res.
Postfach 510153
D-3000 Hannover 51, GERMANY

Dr. Kin Yip Chun
Geophysics Division
Physics Department
University of Toronto
Ontario, CANADA

Dr. Johannes Schweitzer
Institute of Geophysics
Ruhr University/Bochum
P.O. Box 1102148
4360 Bochum 1, GERMANY

Prof. Hans-Peter Harjes
Institute for Geophysic
Ruhr University/Bochum
P.O. Box 102148
4630 Bochum 1, GERMANY

Prof. Eystein Husebye
NTNF/NORSAR
P.O. Box 51
N-2007 Kjeller, NORWAY

David Jepsen
Acting Head, Nuclear Monitoring Section
Bureau of Mineral Resources
Geology and Geophysics
G.P.O. Box 378, Canberra, AUSTRALIA

Ms. Eva Johannisson
Senior Research Officer
National Defense Research Inst.
P.O. Box 27322
S-102 54 Stockholm, SWEDEN

Dr. Peter Marshall
Procurement Executive
Ministry of Defense
Blacknest, Brimpton
Reading RG7-FRS, UNITED KINGDOM

Dr. Bernard Massinon, Dr. Pierre Mechler
Societe Radiomana
27 rue Claude Bernard
75005 Paris, FRANCE (2 Copies)

Dr. Svein Mykkeltveit
NTNF/NORSAR
P.O. Box 51
N-2007 Kjeller, NORWAY (3 Copies)

Prof. Keith Priestley
University of Cambridge
Buildard Labs, Dept. of Earth Sciences
Madingley Rise, Madingley Road
Cambridge CB3 0EZ, ENGLAND